

HERMETIC PACKAGES AND FEEDTHROUGHS FOR NEURAL PROSTHESES

Final Report

(Contract NIH-NINDS-N01-NS-4-2319)

(Contractor: The Regents of the University of Michigan)

For the Period:

September 1, 1994- February 28, 1998

Submitted to the

Neural Prosthesis Program

National Institute of Neurological Disorders and Stroke

National Institutes of Health

By the

Center For Integrated Sensors and Circuits

Department of Electrical Engineering and Computer Science

University of Michigan

Ann Arbor, Michigan 48109-2122

14th report
final.

Program Personnel:

UNIVERSITY OF MICHIGAN

Professor Khalil Najafi: Principal Investigator

Graduate Student Research Assistants:

Mr. Anthony Coghlan: Microstimulator Assembly, Transmitter Design

Mr. Mehmet Dokmeci: Packaging and Accelerated Testing

Mr. Sebastien Hauvespre: Package Fabrication and Testing

Mr. Mark Nardin: Design and Fabrication of Multichannel Microstimulators

Mr. Jeffrey Von Arx: Electrode/Package Fabrication/Testing, On-Chip Coils

Ms. Jane Ueda: Microstimulator Assembly

VANDERBILT UNIVERSITY

Professor David L. Zeale: Principal Investigator -

March 1998

**THIS QPR IS BEING SENT TO
YOU BEFORE IT HAS BEEN
REVIEWED BY THE STAFF OF THE
NEURAL PROSTHESIS PROGRAM.**

SUMMARY

This final report summarizes work performed over the past three and a half years to develop hermetic packages and feedthroughs for a variety of implantable neural prostheses and stimulators, as well as work on the development of implantable single- and multi-channel implantable microstimulators for use in functional neural stimulation. The primary objectives of the past contract were: 1) the development and characterization of hermetic packages for miniature, silicon-based, implantable three-dimensional structures designed to interface with the nervous system for periods of many decades; 2) the development of techniques for providing multiple sealed feedthroughs for the hermetic package; 3) the development of custom-designed packages and systems used in chronic stimulation or recording in the central or peripheral nervous systems in collaboration and cooperation with groups actively involved in developing such systems and establishing the overall biocompatibility of these packages; and 4) the development of single-channel and multichannel microstimulators that will serve as a vehicle to demonstrate the suitability of the packages and feedthroughs.

During the past three contract periods, our research and development program has made considerable progress in a number of areas related to the above goals. A hermetic packaging technique based on electrostatic bonding of a custom-made glass capsule and a supporting silicon substrate has been developed. This technique allows the transfer of multiple interconnect leads between electronic circuitry and hybrid components located in the sealed interior of the capsule and stimulating electrodes located outside of the capsule. The glass capsule can be fabricated using a variety of materials and can be made to have arbitrary dimensions as small as a few cubic millimeters. Long-term tests of glass packages in high temperature saline and deionized water baths has shown them to be hermetic for a period of at least 40 years.

A multiple sealed feedthrough technology has been developed that allows the transfer of electrical signals through polysilicon conductor lines located on a silicon support substrate. Several hundred feedthroughs can be fabricated in a length of less than 1.5mm. The feedthroughs have also been tested under accelerated test conditions and have shown to be functional in these conditions. The packaging and feedthrough techniques utilize materials that are biocompatible and can be integrated with a variety of micromachined silicon structures.

The packaged and feedthroughs have been implanted in several animal models in collaboration with colleagues at Vanderbilt University, University of Michigan, Hines VA Hospital, and several other groups. These implants have been performed for periods ranging from a few weeks up to one year. The results from all of these in-vivo tests are consistent and show no sign of significant damage to the biological tissue. The packages have also been tested after explantation for sign of moisture penetration and they seem to be intact, unless mechanically damaged during surgery. The project provided several tens of packages to investigators around the country for biocompatibility tests and will continue to do so in the future.

A mixed analog-digital circuit block based on CMOS and bipolar technologies has been developed. This circuit receives a modulated RF carrier from the transmitter and generates regulated power supplies, control data, clock, and regulated stimulation currents that are delivered to the tissue through the on-chip stimulating electrodes. Voltage and current regulators are implemented using bipolar devices, while control logic is implemented using low-power CMOS circuits. These devices are fabricated using a unique Bipolar-CMOS technology that has been developed in our laboratory during our previous contracts.

During this past contract several implantable microstimulators were developed. An inductively-powered single-channel microstimulator capable of delivering charge-balanced pulses through IrOx electrodes formed on a silicon substrate has been developed and shown to be

fully functional. We also developed a multi-channel version of this microstimulator. This device provides eight electrodes for stimulation, has programmable amplitude and duration, and utilizes much more reliable circuit blocks for power generation, clock recovery, data recovery, and current delivery. The circuit blocks are designed to operate with very small amount of power, and are much more tolerant to process parameter, and data modulation variations. In addition, the second generation device has incorporated an on-chip active transmitter, thus providing a bi-directional telemetry link. The on-chip transmitter, allows the microstimulator to communicate with the outside world in order to perform several functions, including hand shaking for reliable data transfer and package integrity tests to inform the user when the package is compromised. In the future, this device design can be used to transmit sensed data from the implant to the outside world, which is a crucial function for many next generation implantable systems needed for neural prostheses.

Since many future implantable systems, such as those used for peripheral nerve stimulation, require smaller profiles (i.e., smaller heights), it desirable to eliminate the use of hybrid components such as coils and capacitors which are required for telemetry applications. During the past contract our group also developed on-chip coils monolithically integrated with electronics circuits to reduce the height of wireless implantable systems to below 1mm, including the package. We have demonstrated that these on-chip coils are capable of receiving at least several milliwatts of power at a distance of several centimeters from an external transmitter and can easily power an integrated circuit chip and deliver current to the tissue. An 8-channel integrated circuit chip with on-chip coils has been designed, and fabricated, to deliver constant current pulses of up to 2mA in amplitude to peripheral nerves through any 8 user-selected channels. This system has recently been tested and shown to be fully functional. In the future packaged and assembled versions of this system will be built and delivered to outside investigators for further testing.

The combination of the above technologies has allowed us for the first time to implement implantable systems. Obviously the road ahead is both exciting and challenging, and based on our past progress we believe that fully functional, robust, and practical multichannel implantable microstimulators for a variety of applications can be fabricated. We believe that we have achieved most of the objectives stated in the original proposal. This report will summarize results obtained during the past contract covering the period September 1, 1994 to February 28, 1998.

TABLE OF CONTENTS

Summary	2
1. Introduction.....	5
2. Hermetic Packages and Feedthroughs.....	10
2.1. Package and Feedthrough Fabrication Technology	10
2.1.1. Glass-Silicon Bonding	10
2.1.2. Fabrication of Glass Capsules.....	11
2.1.3. Multiple Feedthrough Technology.....	14
2.2 In-Vitro Testing.....	18
2.2.1 Mechanical Strength Measurements	18
2.2.2 Humidity Monitoring	20
2.2.3 Accelerated Testing Model	22
2.2.4 Accelerated Soak Tests in Phosphate Buffered Saline	24
2.2.5 Interpretation of the Long Term Soak Testing Results in Saline	26
2.2.6 Accelerated Testing of Silicone Coated Glass Packages In Saline	26
2.2.7 Room Temperature Soak Tests in Saline.....	30
2.2.8 Accelerated Soak Tests in Deionized Water.....	30
2.2.9 Dissolution Studies of Silicon and Polysilicon in Saline and Deionized Water.....	34
2.2.10 Analysis of the Failure Modes	35
2.3 In-Vivo Testing	37
2.3.1 Biocompatibility Studies Performed in The University of Michigan Facilities	37
2.3.2 Biocompatibility Studies At the Hines VA Hospital	38
2.3.3 Animal Studies Conducted Through Consortium With Vanderbilt University	40
3. Implantable Wireless Microstimulation Systems.....	53
3.1 Single Channel Microstimulators.....	53
3.2 Multichannel Microstimulator With A Bi-Directional Telemetry Link	55
3.2.1 Overall System Architecture	56
3.2.2 Bi-directional Telemetry Link	59
3.3 FINESS System Overview.....	61
3.3.1 On-Chip Coils For Inductive Powering	64
3.3.2 Modeling the Telemetry Link	66
3.3.3 Results from On-Chip Coil Models	67
3.3.4 Fabrication and Testing of On-chip Coils.....	71
3.3.5 Fabrication of the On-Chip Coils.....	75
3.3.6 Measured Power Reception Of The On-Chip Coils.....	77
3.3.7 Circuit Design	80
3.3.8 Telemetry Communications Protocol	86
3.3.9 FINESS Chip Test Results.....	90
3.3.10 Electrical Test Results From The FINESS Chip.....	91
4. Conclusions.....	95
5. Papers and Theses Produced By The Current Contract.....	97
References	99

1. Introduction

The overall goal of this program was to develop a miniature hermetic package and integrated sealed feedthroughs for miniature, silicon-based, implantable three dimensional structures designed to interface with the nervous system. The packaging technology developed can seal a variety of electronic components such as capacitors and coils, and integrated circuits which can interface with external sensors (in particular electrodes) used in neural prostheses. Although the applications are different, it is possible to identify a number of common requirements in all of these applications. This packaging and feedthrough technology is capable of:

- 1- protecting non-planar electronic components such as capacitors and coils, which typically have large dimensions of about a few millimeters;
- 2- protecting integrated circuit chips that are either integrated monolithically or attached in a hybrid fashion with the substrate that supports the sensors used in the implant;
- 3- interfacing with structures that contain either thin-film electrodes or conventional microelectrodes that are attached to the structure;
- 4- providing a biocompatible interface to the tissue and contain materials that do not create adverse histological reactions in the tissue;

and

- 5- protecting the implanted electronics and systems from the biological environment for periods of many decades.

The general requirements for the hermetic package for neural prostheses as originally stated in our contract are summarized in Table 1. We have identified two general categories of packages that need to be developed for implantable neural prostheses. The first deals with those systems, or parts of a system, that contain relatively large components like capacitors, coils, and hybrid integrated circuit chips, such as needed in implantable microstimulators. The second deals with those systems, or parts of a system, that contain only integrated circuit chips that are either monolithically fabricated on the substrate or are attached in a hybrid fashion to the system, such as those needed in low-profile peripheral nerve stimulation of neural recording systems.

Figure 1.1 shows our general approach to the implementation of the package required in the first category. The package is a glass capsule that is electrostatically sealed to a support silicon substrate using electrostatic bonding. Inside the glass capsule all of the necessary components for the system are housed. The electronic circuitry needed for any analog or digital circuit functions is either fabricated on a separate circuit chip that is hybrid mounted on the silicon substrate and electrically connected to the silicon substrate, or integrated monolithically in the support silicon substrate itself. The attachment of the hybrid IC chip to the silicon substrate can be performed using a number of different technologies such as simple wire bonding between pads located on each substrate, or using more sophisticated techniques such as flip-chip solder reflow or tab bonding. The larger capacitor or microcoil components are mounted on either the substrate or the IC chip using appropriate epoxies or solders. This completes the assembly of the electronic components of the system and it should be possible to test the system electronically at this point before the package is completed. After testing, the system is packaged by placing the glass capsule over the entire system and bonding it to a polysilicon bond region, using the electrostatic sealing process. As we will discuss later, the cavity inside the glass package is now hermetically sealed against the outside environment. Feedthroughs to the outside world are provided using the grid-feedthrough technique that will be discussed later.

These feedthroughs transfer the electrical signals between the electronics inside the package and various elements outside of the package. If the package has to interface with conventional microelectrodes, these microelectrodes can be attached to bonding pads located outside of the package; the bond junctions will have to be protected from the external environment using various polymeric encapsulants such as silicone rubber. If the package interfaces with on-chip electrodes, it can do so by integrating the electrode on the silicon support substrate. Interconnection is simply achieved by using on-chip polysilicon conductors that make the feedthroughs themselves. If the package has to interface with remotely located recording or stimulating electrodes that are attached to the package using a silicon ribbon cable, it can do so by integrating the cable and the electrodes again with the silicon support substrate that houses the package and the electronic components within it.

Table 1: General Requirements for Miniature Hermetic Packages and Feedthroughs for Neural Prostheses Applications.

Package Lifetime:

≥ 40 Years in Biological Environments @ 37°C

Packaging Temperature:

≤360°C

Package Volume:

10-100 cubic millimeters

Package Material:

Biocompatible

Transparent to Light

Transparent to RF Signals

Package Technology:

Batch Manufactureable

Package Testability:

Capable of Remote Monitoring

In-Situ Sensors (Humidity & Others)

Feedthroughs:

At Least 12 with ≤125μm Pitch

Compatible with Integrated or Hybrid Microelectrodes

Sealed Against Leakage

Testing Protocols:

In-Vitro Under Accelerated Conditions

In-Vivo in Chronic Recording/Stimulation Applications

Figure 1.2 shows our approach to implementing the package for the second category of applications. In these applications, there are no large components such as capacitors and coils. The only component that needs to be hermetically protected is the electronic circuitry. This circuitry is either monolithically fabricated in the silicon substrate that supports the electrodes (similar to the active multichannel probes being developed by the Michigan group), or is attached to the silicon substrate in a hybrid fashion that supports the electrodes (like the passive probes being developed by the Michigan group). In both of these cases the package is a glass capsule that is electrostatically sealed to the silicon substrate electrostatically. Notice that in this case, the glass package need not be a high profile capsule, but rather it need only have a cavity that is deep enough to allow for the silicon chip to reside within it. Note that even though the silicon IC chip is originally 500 μm thick, it can be thinned down to about 100 μm , or can be recessed in a cavity created in the silicon substrate itself. In either case, the recess in the glass is less than 100 μm deep (as opposed to several millimeters for the glass capsule). Such a glass package can be easily fabricated in a batch process from a larger glass wafer. The recess in the glass can be created using photolithographic techniques and etching using hydrofluoric acid. This simplifies glass package fabrication, and can be potentially performed at the wafer level even before the micromachined silicon substrate is released from the host wafer.

We believe the above two approaches address the needs for most implantable neural prostheses. Note that both of these techniques utilize a silicon substrate as the supporting platform, and are not directly applicable to structures that use other substrate materials such as ceramics or metals. Although this may seem a limitation at first, we believe that the use of silicon is, in fact, an advantage because it provides several benefits. First, it is biocompatible [1,2] and has been used extensively in biological applications. Second, there is a great deal of effort in the IC industry in the development of multi-chip modules (MCMs), and many of these efforts use silicon supports because of the ability to form high density interconnections on silicon using standard IC fabrication techniques. Third, many present and future implantable probes are based on silicon micromachining technology; the use of this packaging technology is inherently compatible with most of these probes, which simplifies the overall structure and reduces its size.

In the following sections, we will summarize the results of research aimed at the development and testing of these packages, as well as efforts that were undertaken to develop miniature implantable microstimulators for neuromuscular stimulation. The microstimulators represent one of the primary applications of the packages and feedthroughs developed under this contract. As will be presented, several generation of packages have been developed for different versions of these microstimulators. The report will first present the results of the hermetic packages and feedthroughs, and it will then present the development of the various versions of microstimulators.

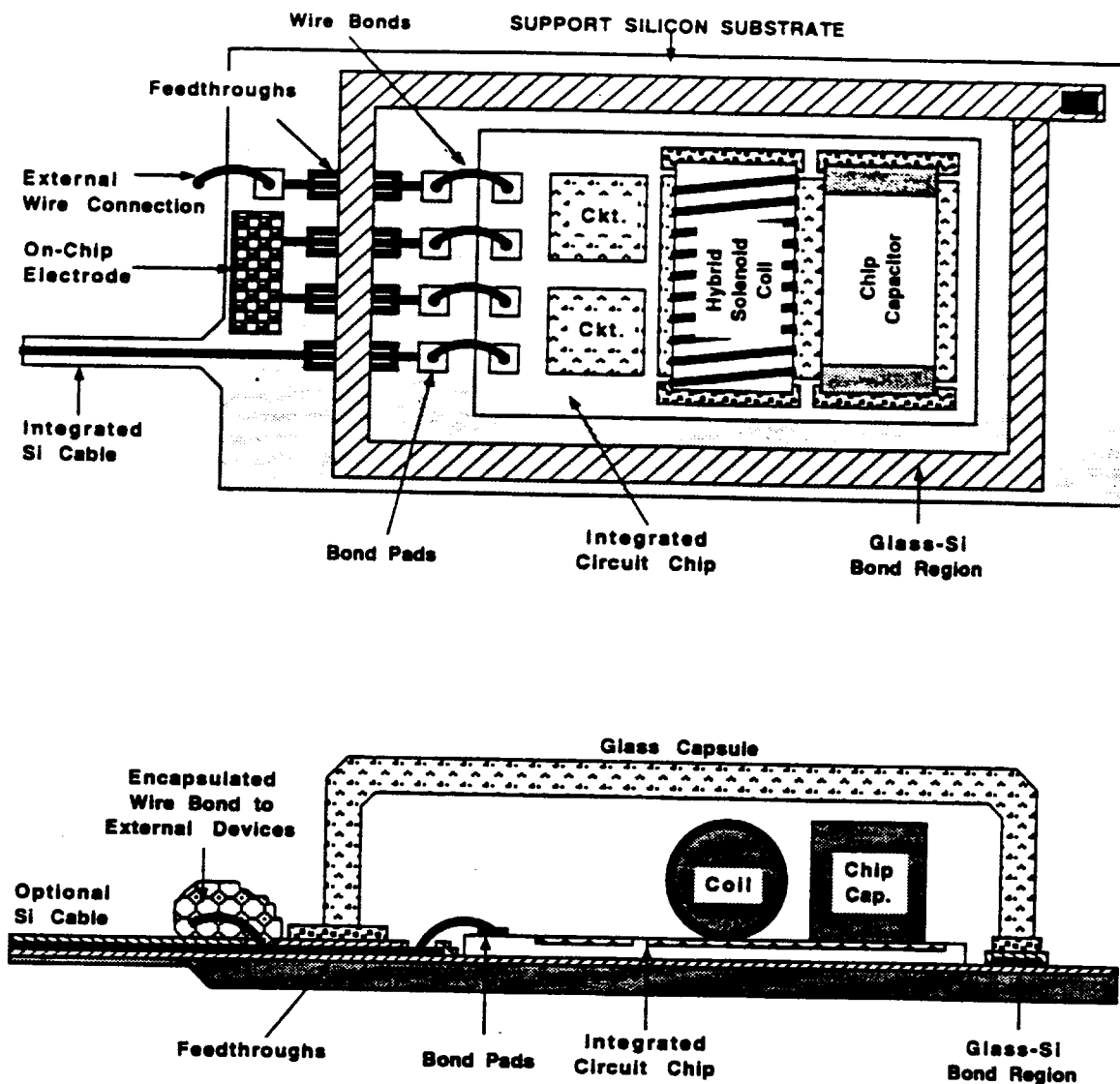


Figure 1.1: A generic approach for packaging implantable neural prostheses that contain a variety of components such as chip capacitors, microcoils, and integrated circuit chips. This packaging approach allows for connecting to a variety of electrodes.

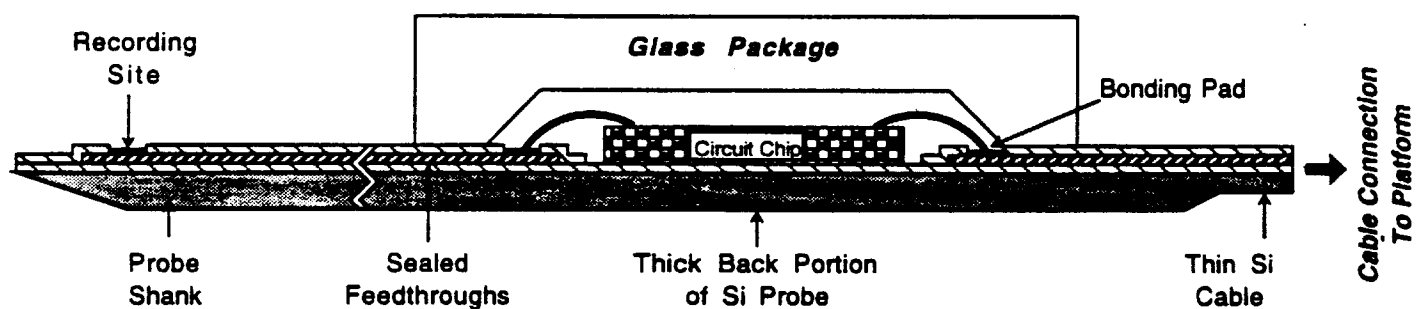


Figure 1.2: Proposed packaging approach for implantable neural prostheses that contain electronic circuitry, either monolithically fabricated in the probe substrate or hybrid attached to the silicon substrate containing microelectrodes.

2. Hermetic Packages and Feedthroughs

The following section summarizes the basic packaging technology based on glass-Si bonding, the implementation of sealed feedthroughs, the results of accelerated tests on the package for the determination of the mean time to failure of the package, and finally the results of in-vivo tests for determining the biocompatibility of the packages and feedthroughs.

2.1 Package and Feedthrough Fabrication Technology

2.1.1 Glass-Silicon Bonding

Electrostatic bonding of glass and silicon wafers has long been used for the fabrication of a variety of silicon-based sensors. This bonding occurs when two polished wafers of silicon and glass are brought into intimate contact and a high voltage is applied across this sandwich to create a permanent chemical bond. Electrostatic bonding of silicon and glass is illustrated in Figure 2.1. The glass-silicon sandwich is heated to $\approx 300\text{-}400^\circ\text{C}$, which tends to soften the glass and lower its electrical resistivity, and a DC voltage of 800-1500V is applied across the glass-silicon combination. This voltage generates very high electrostatic attractive forces which pull the silicon and the glass into intimate contact thus promoting and creating a chemical bond. Once the bond is complete, the structure is cooled to room temperature. The bond is achieved between Si and O_2 atoms and is created by the high temperature and the extreme attractive force generated by the electrostatic voltage. The Si-O bond is stronger than the Si-Si bonds in the substrate, and it is stronger than the glass. In order to minimize intrinsic stresses generated within the structure and at the silicon-glass interface, the thermal expansion coefficients of the glass and silicon have to be as nearly matched as possible. Therefore, Pyrex glass code #7740 is often used for silicon-glass bonding applications since this glass not only has an expansion coefficient very close to that of silicon, but it has a low softening point that helps lower the bonding temperature. In order to ensure a high quality bond, the surfaces of both the silicon and the glass have to be polished and free of any scratches and defects.

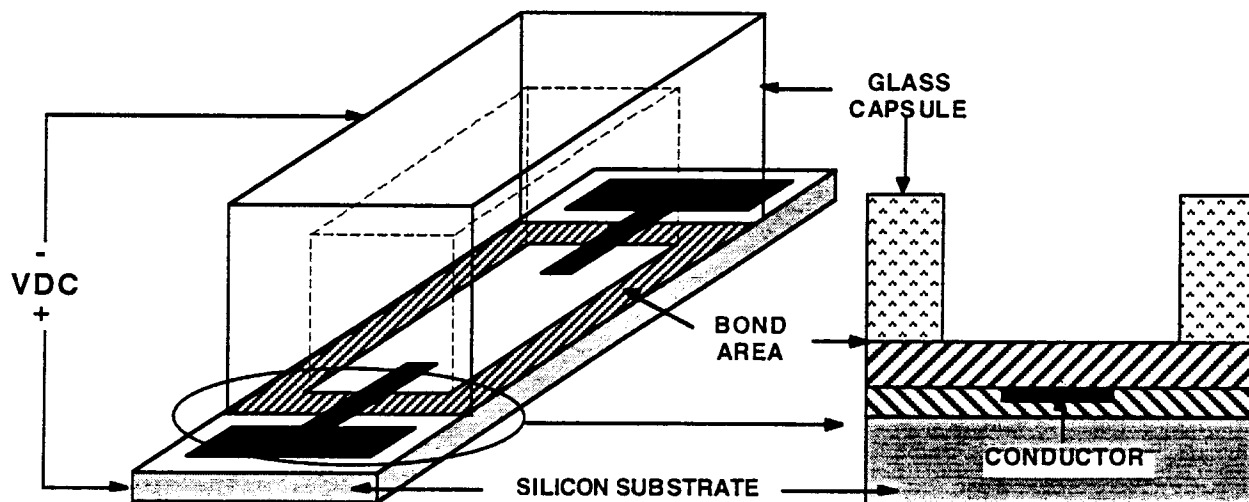


Figure 2.1: Electrostatic bonding of a silicon substrate and a glass capsule. The glass-silicon structure is first heated to temperatures of $\approx 320\text{-}400^\circ\text{C}$, and a DC voltage of 800-1500V is applied across the structure to create a permanent chemical bond between silicon and glass wafers. The bond between Si and O is stronger than the glass and the Si-Si bond.

2.1.2. Fabrication of Glass Capsules

In order to utilize this technique to create a hermetic package for the microstimulator, a glass capsule using code #7740 glass and satisfying the dimensional requirements for the microstimulator with a high-quality bonding surface is needed. Our glass capsules are now machined from a thick wafer of #7740 glass rather than made by molding. The glass wafer is milled by an ultrasonic machining tool as illustrated in Figure 2.2 to create cavities of different shapes and sizes as required by a given application. After milling, the wafer surface is polished to ensure planarity and smoothness. Polishing a wafer is a standard procedure which can be done much more accurately than polishing the small individual molded pieces. Finally the polished wafer is diced apart to form the individual glass capsules. This method of forming the glass capsules has a number of advantages. It is inexpensive (\$3.00 per capsule), has a smooth surface because polishing is done on the wafer level, and it provides excellent planarity for the bonding surface because the bonding surface starts out as a planar wafer. The top surface of the capsules can be metallized before dicing by standard wafer level metallization techniques to evenly distribute the electric field during bonding. In addition, using a machined wafer allows for batch assembly by wafer level electrostatic bonding.

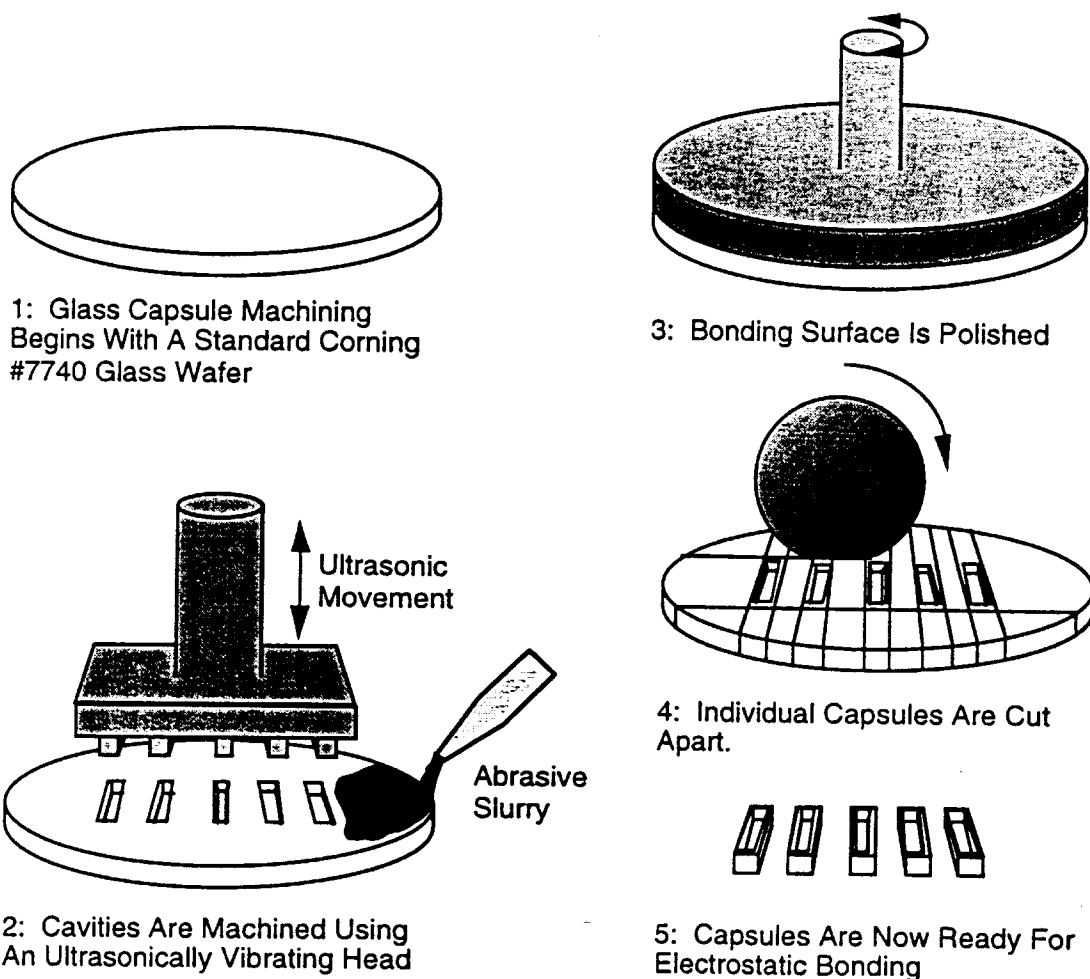


Figure 2.2: Batch fabrication of glass capsules from a Corning code #7740 glass wafer.

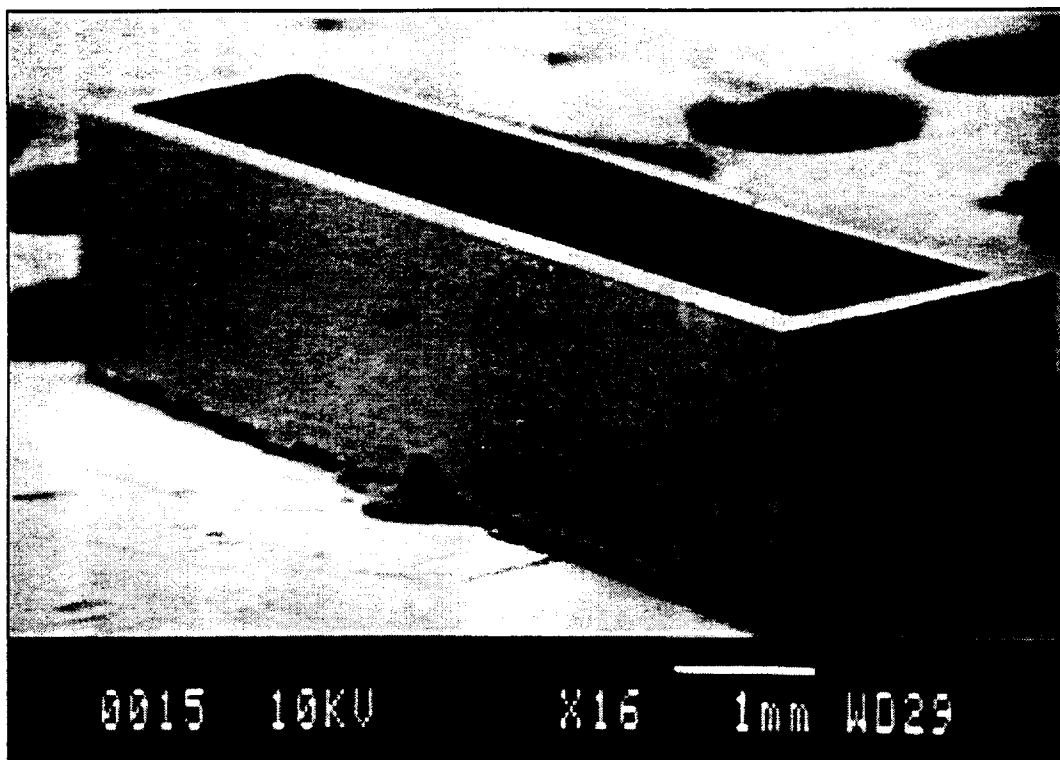


Figure 2.3: SEM micrograph of a glass capsule fabricated by ultrasonic machining. The capsule walls are about 0.3mm thick, and the inside dimensions are ~2mmx2mmx9.2mm. It is made of #7740 glass which has a thermal expansion coefficient close to that of silicon.

It should also be mentioned that in our earlier research we had used molded glass packages which were fabricated individually, and which provided a rounded top surface. Later in the report we will refer to these molded packages when we present accelerated testing data. However, all of our tests since we have developed the ultrasonic machining method have been conducted using the new glass capsules.

Figure 2.4 shows an SEM of a glass capsule electrostatically bonded to a silicon substrate using the methods discussed above.

Ultrasonic machining of glass is usually required when the cavities created in it have to be rather deep to be able to accommodate large components like hybrid capacitors and coils. As an extension of this effort we have also developed silicon-glass packages that only consist of integrated components. To encapsulate such systems we have developed an approach to make glass capsules for low profile applications. The fabrication sequence is shown in figure 2.5. The original thickness of the glass wafers is about 750 μ m. First, we deposit and pattern Chromium/Gold layers to act as a mask against the etchant. Next the glass is recessed for a depth of about 40 μ m in HF/HNO₃ solution. Later, the glass wafer is thinned from the other side to a final thickness of approximately 300 μ m. The final steps of this process include dicing the glass wafer into small glass capsules and then bonding to the silicon substrate. Figure 2.6 shows a SEM micrograph of the finished package. Due to the reduction in the thickness of the glass, the bonding voltage is reduced to about 1000 volts.

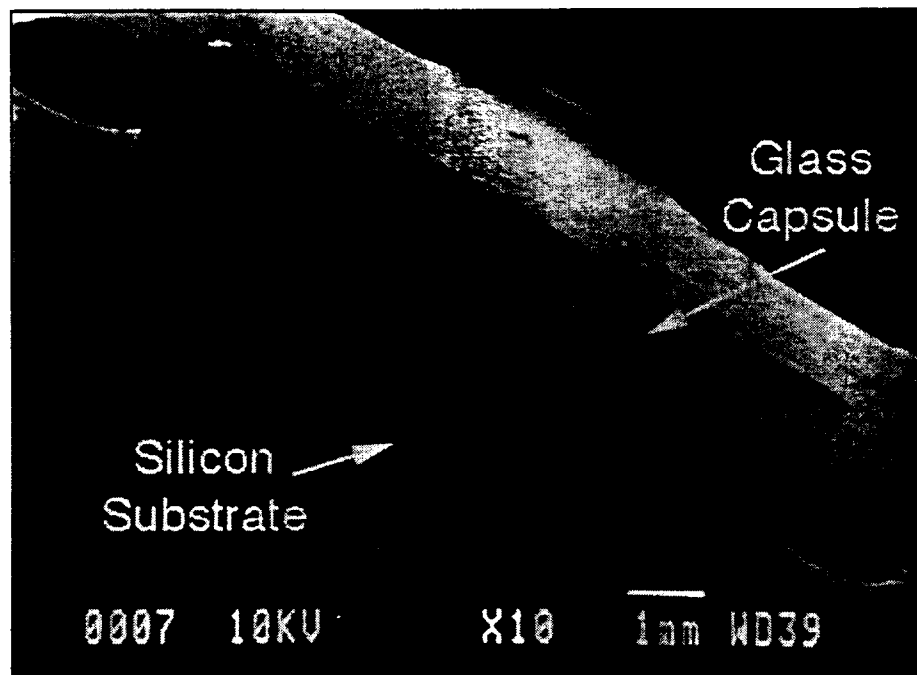


Figure 2.4: SEM Photograph of a glass capsule bonded to a silicon substrate.

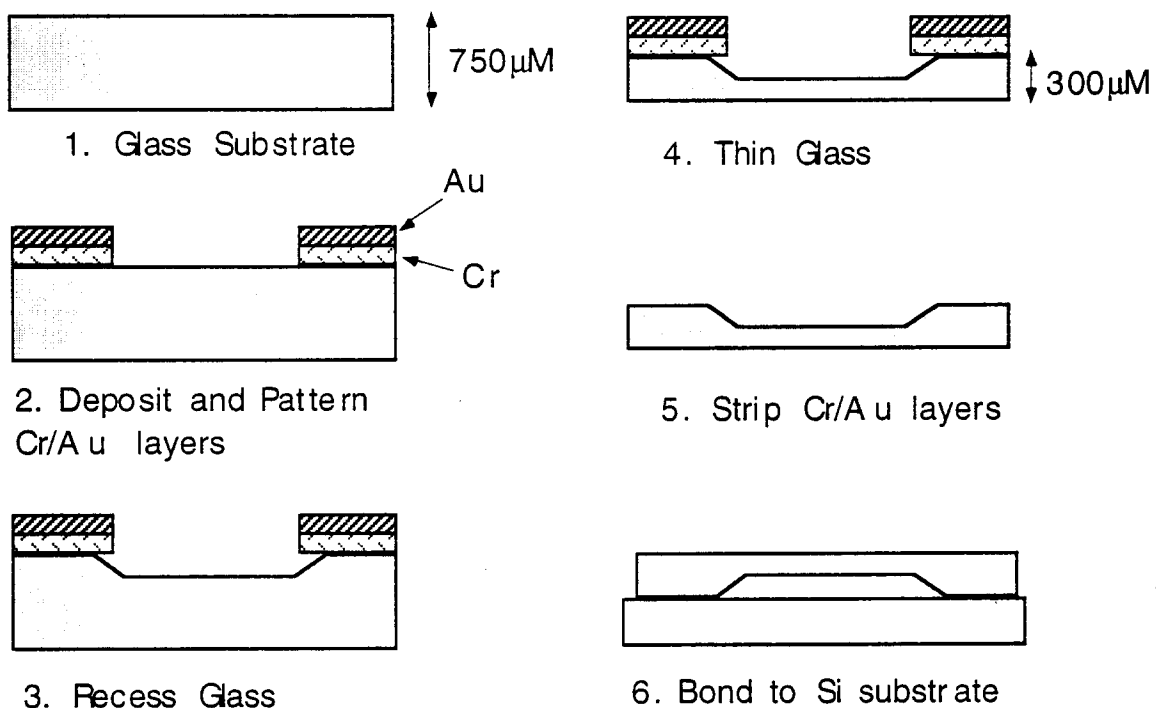


Figure 2.5: The fabrication sequence for the low profile package.

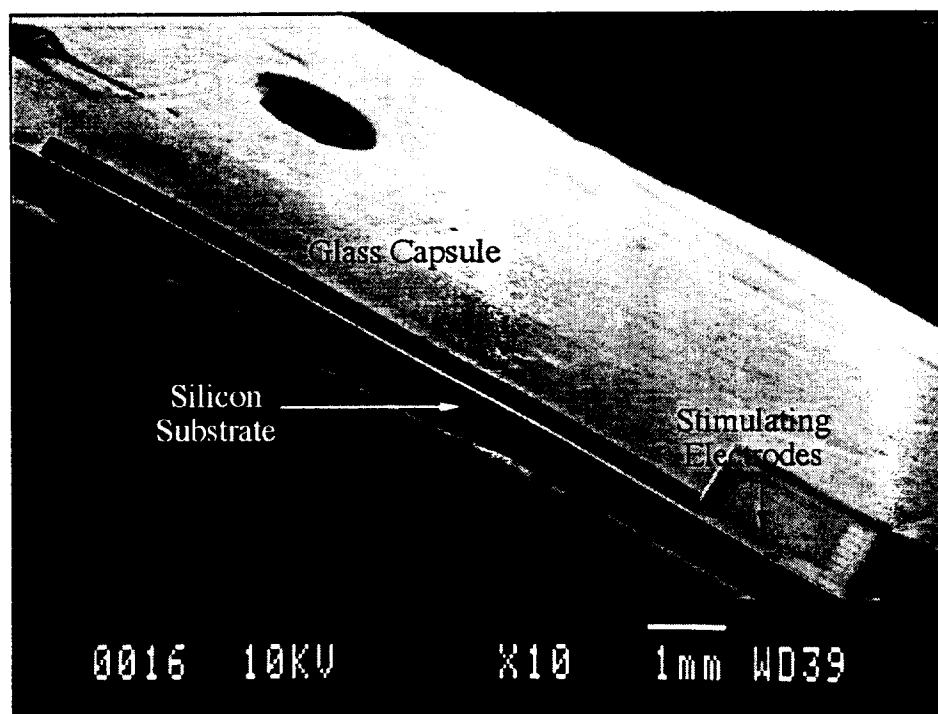


Figure 2.6: The SEM micrograph of the low profile package.

2.1.3 Multiple Feedthrough Technology

Feedthrough lines for connecting the circuitry to the electrodes and for various monitoring purposes are provided using polysilicon conductors insulated by dielectric layers, as shown in Figure 2.7. Polysilicon feedthrough lines connecting the electrodes to the circuitry inside the package have to be insulated from body fluids on top in order to prevent shorting by body electrolytes. This is done by depositing dielectric layers of low-pressure chemical vapor deposited (LPCVD) oxide/nitride/oxide on top of the feedthroughs. In order to reduce the bonding temperature to below 320°C, which is a temperature tolerated by the hybrid chip capacitor and receiver coil, we have developed a new technique which involves bonding the glass capsule to a top layer of LPCVD deposited fine-grain polysilicon, as shown in Figure 2.5. In this structure, the electrostatic voltage is applied across the glass capsule and the polysilicon layer avoiding the large voltage drop across the other thick dielectric films that insulate the polysilicon feedthrough conductors. Bonding to this fine-grain polysilicon overlayer effectively reduces the bonding temperature to ~300°C. The polysilicon overlayer used for bonding must have a smooth surface if a good hermetic bond is to be achieved. The roughness and grain structure of LPCVD polysilicon is strongly influenced by dopants, deposition temperature, and post-deposition heat cycles. Polysilicon deposited below 575°C is nearly amorphous and has a smooth surface with no detectable structure. Polysilicon deposited above 625°C is polycrystalline and has columnar structure. In order to achieve a smooth surface for electrostatic bonding of the glass capsule, polysilicon deposited at 570°C is now routinely used. Because of the very small grain sizes, we refer to this polysilicon as fine-grain polysilicon, as opposed to coarse-grain polysilicon deposited at 625°C. The surface roughness of fine-grain polysilicon has a rms value of less than 8Å, which is quite close to that of a polished single crystal silicon wafer. The coarse-grain polysilicon, however, has a surface roughness much larger than this and can be as large as several thousand angstroms and strongly depends on particular deposition conditions.

and surface features. We have been able to use the fine-grain polysilicon film in the microstimulator package reproducibly and reliably as will be discussed below.

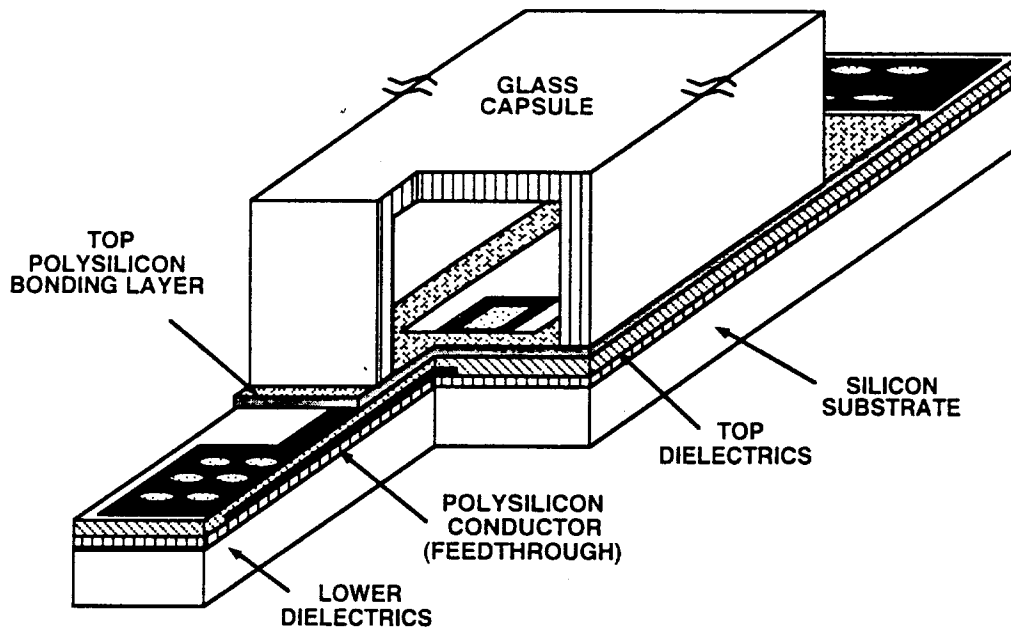


Figure 2.7: The structure of the microstimulator packaging technology that utilizes a top fine-grain polysilicon film to lower bonding temperature and sealed polysilicon feedthroughs for lead transfer to the outside environment.

The packaging technology must also be able to provide feedthrough lines for connecting the circuitry inside the package to the electrodes outside. This lead transfer should be performed without disturbing the surface planarity over the feedthrough lines. Any nonplanarity (more than 100Å) over the feedthrough lines would cause a local unbonded region between the glass and silicon which in turn allows a path for moisture to penetrate inside the package. We have developed a new technology for the transfer of multiple leads for the microstimulator package which utilizes phosphosilicate glass (PSG; phosphorus-doped silicon dioxide) films to planarize the bonding regions and fill any gaps between closely-spaced feedthrough conductor lines. The PSG film is annealed and reflowed through a high-temperature annealing step to completely planarize the top bonding surface.

Figure 2.8 shows the fabrication sequence for these feedthrough lines. Fabrication begins with a standard silicon substrate, over which $\sim 1\mu\text{m}$ of thermal oxide is grown for isolation, and is followed by the deposition of $1\mu\text{m}$ of LPCVD polysilicon to form the feedthrough lines (the first poly). The polysilicon is subsequently doped by diffusing phosphorus using a liquid source at 950°C for 30 minutes. This yields a low sheet resistance needed for feedthrough lines ($R_s \approx 10 \Omega/\text{square}$). The polysilicon is then patterned using an RIE dry etch to produce the vertical sidewalls needed for planarization. A combination of low temperature oxide (LTO) (deposited at 420°C) of about 2000 Å and phosphosilicate glass (PSG) (phosphorus concentration = 8 wt.%) of about $1.8 \mu\text{m}$ is deposited on top of the polysilicon conductors. The LTO is required to improve PSG adhesion to the first polysilicon. The PSG is then reflowed at 1100°C in steam for 2 hours to planarize the top surface, and is patterned and etched everywhere except over the bond regions. Since PSG absorbs moisture very fast, it is necessary to insulate it with a 3000Å/1500Å/3000Å LPCVD oxide/nitride/oxide sandwich to avoid its exposure to the outside

environment, as shown in Fig. 2.8(d). Note that before the deposition of this polysilicon film, the top dielectric layers and the bottom dioxide layer are removed around the edges of the substrate to expose the silicon substrate. Subsequently, a $1\mu\text{m}$ fine-grain polysilicon layer is deposited on top (the second poly). This polysilicon layer is then lightly doped at 950°C for 30 minutes. Note that this polysilicon layer wraps around the oxide/nitride/oxide layer and prevents their contact with moisture and therefore blocks water penetration through these layers inside the package. The second poly will be used as the bonding overlayer and is patterned to define the bonding surface for the glass capsule. Finally, contacts are opened to the first polysilicon film, and an iridium metallization layer is deposited and patterned to achieve electrical contacts (this mask also defines the stimulating sites of the electrodes). An extra mask is used for contact to the second fine-grain polysilicon, and to form interdigitated comb structures that serve as dew point sensors.

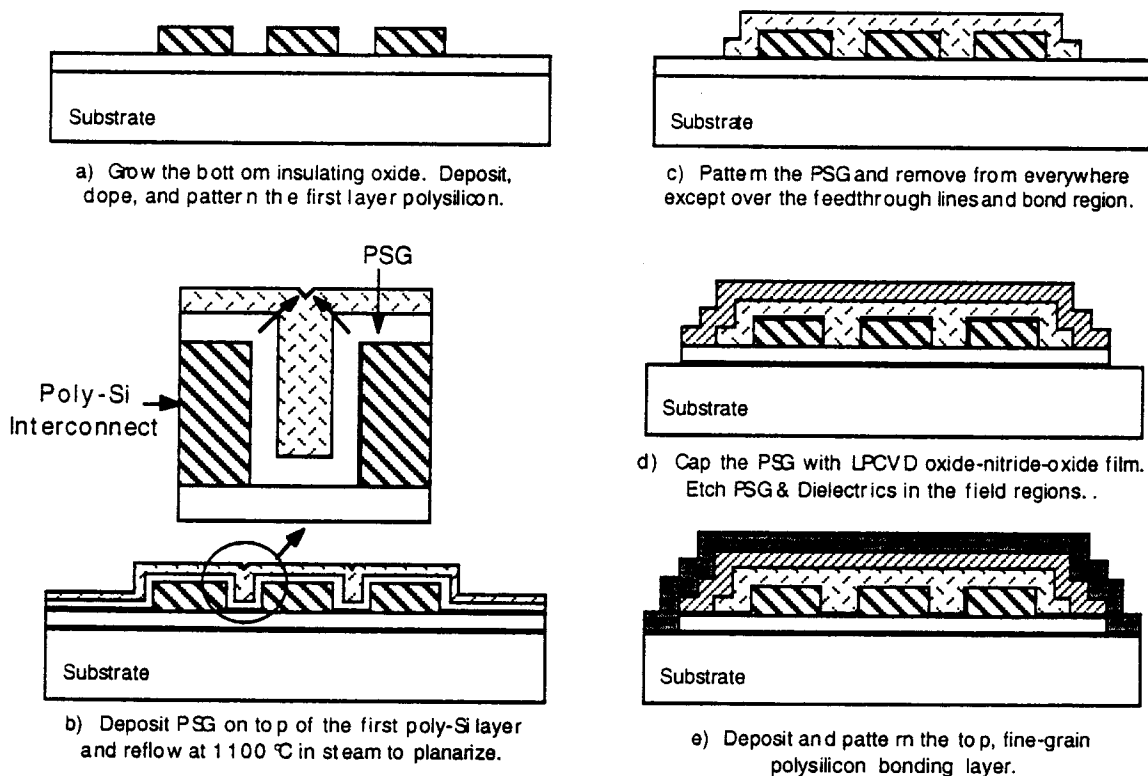


Figure 2.8: Cross section of the fabrication process for on-chip feedthroughs.

Figure 2.9 shows a SEM photograph of the cross-section of the grid feedthrough lines ($1.7\mu\text{m}$ lines with $2.3\mu\text{m}$ spacing), showing the top PSG layer. As can be seen perfect planarity has been achieved using this grid structure. This grid feedthrough technique provides a great amount of flexibility in the number of isolated feedthroughs that can be realized through the package. For example, if series resistance is not an issue, and if one assumes a pitch of about $5\mu\text{m}$ between the polysilicon lines, it is possible to form 300 feedthroughs in a distance of 1.5mm (this is the dimension of the inside width of the microstimulator package). In addition, this process is much more forgiving of slight variations in the separation between the polysilicon lines due to process changes.

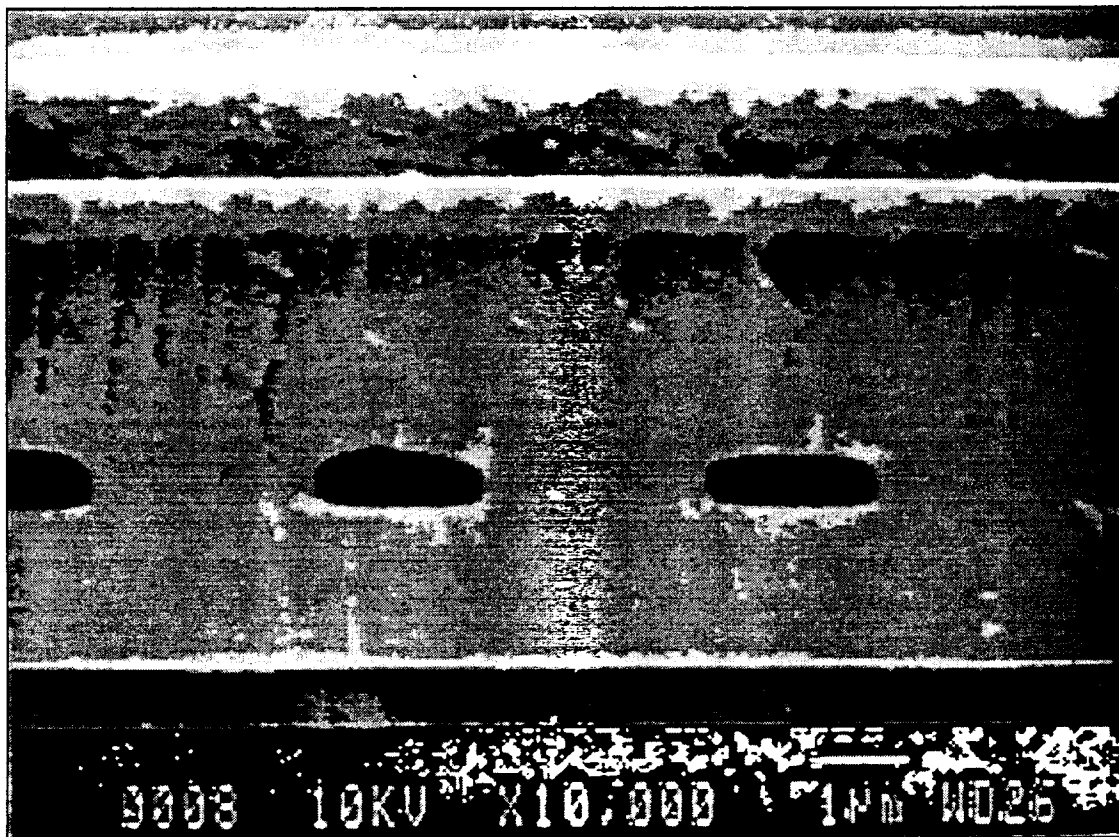


Figure 2.9: SEM photograph of the cross-section of the grid feedthrough lines ($1.7\text{ }\mu\text{m}$ lines with $2.3\text{ }\mu\text{m}$ spacing), showing the top PSG layer. As can be seen perfect planarity has been achieved using this grid structure.

2.2 In-Vitro Testing

In order to determine the suitability of the package for biomedical applications, a series of tests have been performed on the package. These tests are summarized in this section.

2.2.1 Mechanical Strength Measurements

Previously, we mentioned that the strength of the silicon-glass bond exceeded the fracture strength of the glass capsule and the silicon substrate. This was confirmed by breaking the bond and observing that fracture occurred in the glass and not where the bond was formed. We have consistently observed that the fracture always occurred in the lowest resistance point of the package which is the glass capsule. In order to obtain a quantitative measure of the strength of the bond, we performed a series of experiments. Several devices were prepared using the original microstimulator silicon substrate and a glass capsule. In order to attach a large load to the glass and silicon pieces, we then glued a piece of wood block to silicon and glass side of the device as a support and a handle using a strong epoxy, as shown in Figure 2.10. In these pull tests, one device is held fixed whereas weights are gradually added to the other end until the package came apart. The results of the experiments are summarized in the Figure 2.11. These values are obtained by dividing the total load applied to the bonded area between glass and silicon. The maximum tolerable was found to be 14.5 pounds which corresponds to about 13 MPa. The average was 6.6 pounds with the standard deviation being 1.95 pounds. These results fall within the range of the data obtained from similar structures in the literature which ranged from 2 to 25 MPa. Figures 2.12 and 2.13 show the overall and the close-up view from one of these samples. As seen in the Figure 2.12 the package breaks at the lowest resistance point in glass which is expected of a bond which is stronger than both silicon and glass. We should also add that the bond is uniform around the perimeter of the package.

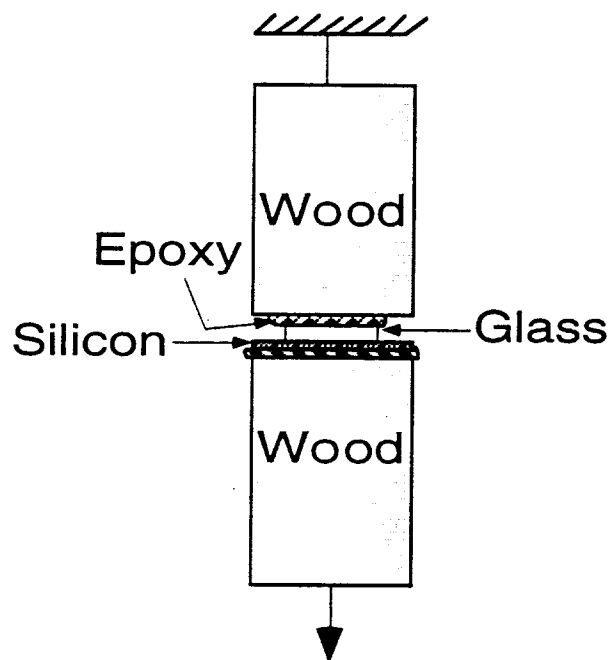


Figure 2.10. The set up for the tensile pull tests.

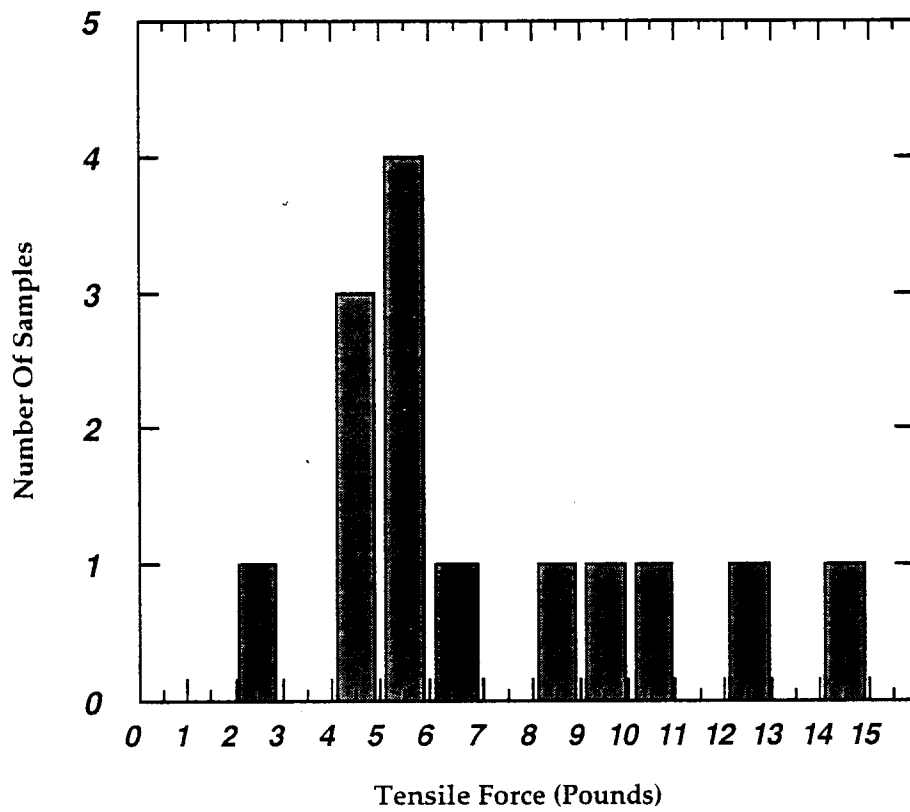


Figure 2.11: The summary of pull test results from polysilicon to bulk Pyrex glass.

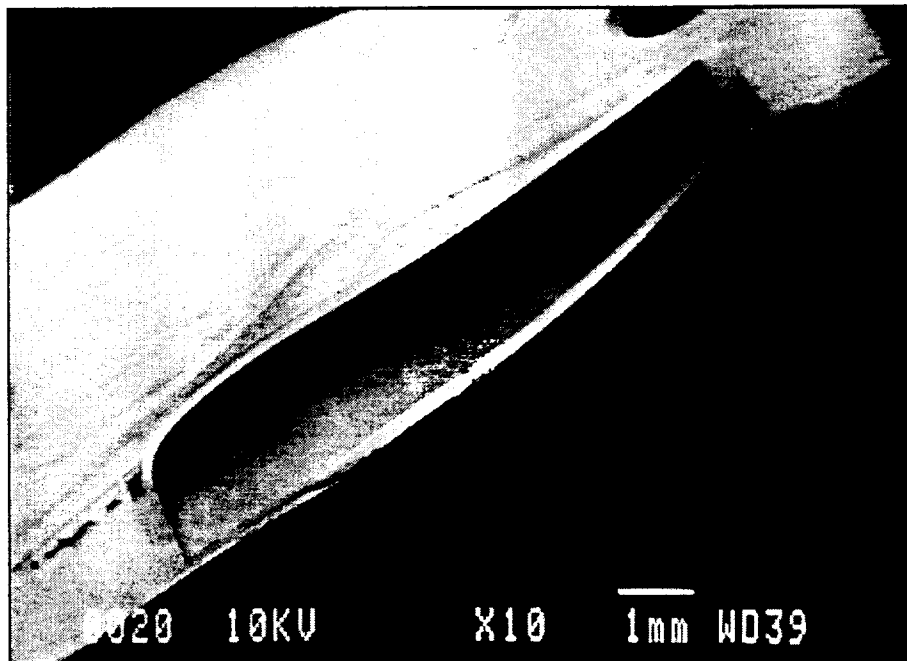


Figure 2.12: SEM photograph of the Silicon to glass package after the bond has come apart.

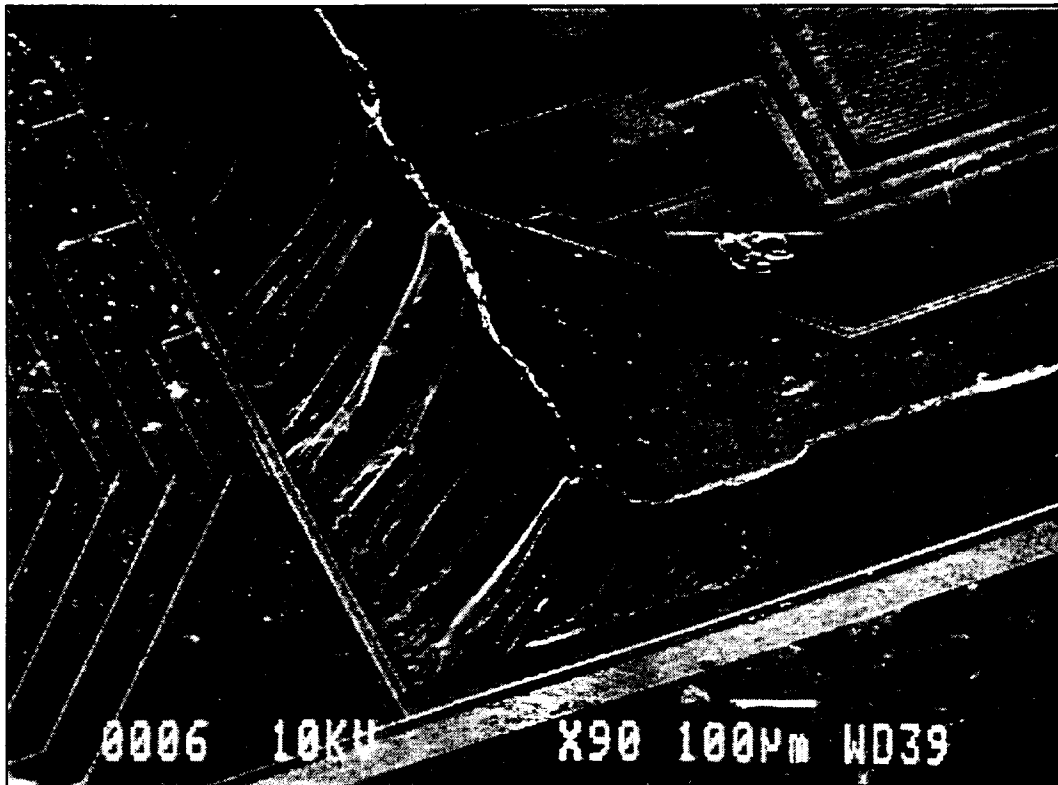


Figure 2.13: SEM photographs of an electrostatic bond area between the glass capsule and the underlying fine-grain polysilicon film from the bottom left corner of Figure 2.12.

In Figure 2.12, the glass surrounds the perimeter of the bonding region. The fracture occurs randomly in the glass capsule. The bottom left hand corner of the same figure is exploded in Figure 2.13. In this figure we see that there is glass residue remaining on the bonding surface of the polysilicon surface. The bond as expected is uniform and hermetically seals the entire bonding region. All of the samples that we have pulled had the same typical pattern remaining on the substrate indicating that the silicon to glass bonds are hermetic, uniform and very strong.

2.2.2 Humidity Monitoring

The package must operate within the body for a period of 40 years. This requires the package to withstand the harsh body environment without allowing moisture to penetrate inside. Moisture is a major cause of failure in non-hermetic packaging, and, together with temperature, is responsible for over 50% of device failures. The common causes of failure due to moisture are: 1) charge separation and surface inversion in MOS devices; 2) corrosion of wire bonds, wire bond pads and metallization runs; and 3) gold and/or silver migration between conducting paths. In the microstimulator application moisture penetration inside the package can be one of the most important sources of failure since the package must continuously operate inside the body in salt water environments. Therefore, there is a need to carefully evaluate the package resistance to moisture penetration and monitor the humidity level inside the package under accelerated test conditions.

In order to test the microstimulator package for hermeticity, the environment inside the package should be monitored to measure the moisture level and changes in humidity over time. Although a number of different humidity sensors can be fabricated to be used inside the package, we have decided to use a simple dew point sensor. This sensor has allowed us to acquire accelerated test data easily without the need for any humidity sensors.

The basic structure of the dew point sensor is shown in Figure 2.14. It consists of a pair of closely spaced interdigitated comb structures. The impedance between the two comb fingers depends on the dimensions of the fingers, the dielectric constant of the medium, and the quality of the surface over which the fingers reside. If the surface is dry and if there exists no appreciable conduction between the fingers, the impedance measured between the two fingers is primarily capacitive. Note that there are also parasitic RC components between each finger and the substrate which are fixed and do not really depend on the surface properties of the dielectric that separates the fingers from the substrate. Note that when the surface of the device is dry (with air having a relative dielectric constant of $\epsilon_r = 1$), the initial capacitance is rather small and produces a high impedance between the comb fingers. Once moisture is condensed on the surface and water contacts both fingers of the comb (with a relative dielectric constant of about $\epsilon_r = 80$), then the impedance between the comb fingers drops drastically. Note that the drop in impedance could be due to two factors: the capacitance between the metal fingers and the liquid becomes very large (by about two orders of magnitude), and the resistance also drops due to the higher conductivity of water. Therefore, when dew point is reached (that is when the moisture level inside the package becomes large enough), surface irregularities due to the comb fingers form fixed condensation nuclei which spread over the whole sensor, thus changing the impedance between comb fingers. The change in capacitance can be read with an impedance meter. Note that this is a very simple structure and a technique to monitor whether moisture has penetrated inside the package; it has a fast response time, is compatible with IC fabrication techniques, is stable, and has a very high operating temperature which is crucial for our application since the package bonding is performed at 300°C. However, the sensor does not allow direct measurement of exact humidity inside the package before dew point. This shortcoming can be circumvented if one can cool the package down to force condensation and measure dew point at lower levels of humidity than possible when tested at room temperature.

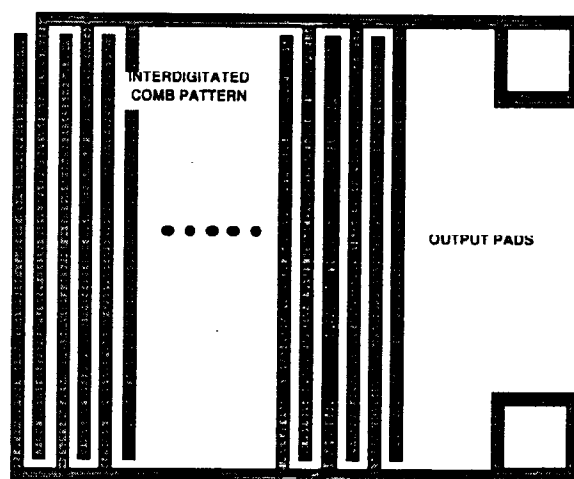


Figure 2.14: Top view of a simple interdigitated dew-point sensor.

The dew point sensor is easily fabricated using the iridium metal used in the fabrication of the stimulating electrodes and can be directly incorporated onto the same substrate that contains the feedthrough lines. The first polysilicon film is used as the feedthrough conductor and is connected to the iridium comb structure using wire bonding. Figure 2.15 shows a photograph of a fabricated substrate with dew-point sensors. When a drop of DI water is placed on top of the sensor, the magnitude drops significantly, while the phase increases. This effect is even more pronounced for salt water, which has a higher conductivity than DI water. Note also that the phase becomes very much resistive at higher frequencies when there is a liquid on top of the sensor because at these frequencies the phase is primarily determined by the resistive nature of the liquid.

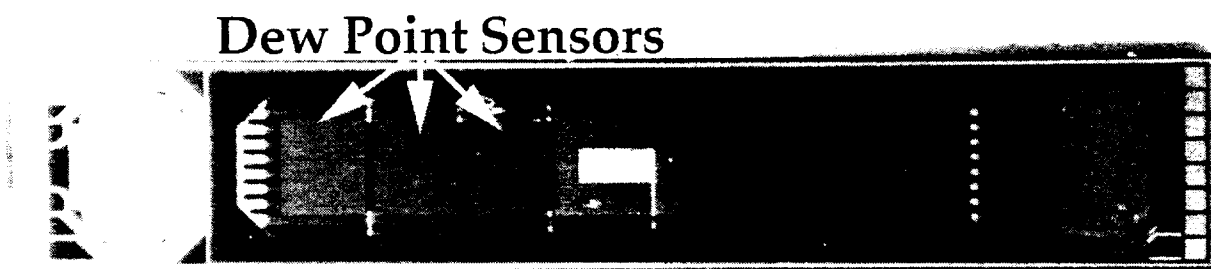


Figure 2.15: Photograph of a fabricated substrate with a number of interdigitated comb structures used as dew-point sensors.

Using this structure, we have performed a number of accelerated tests in phosphate buffered saline and deionized water environments in order to determine the lifetime of the package. This will be presented in the next section.

2.2.3 Accelerated Testing Model

Since the package should operate inside the body for a period of 40 years, accelerated testing schemes must be used in order to determine the expected lifetime of the package. Different mechanisms can be responsible for the penetration of moisture inside the package. Penetration of moisture inside the package occurs through diffusion and permeation, both of which can be accelerated by increasing temperature and humidity. The microstimulator will ultimately be implanted inside the body and will be surrounded by body fluids. Therefore, we have elected not to use humidity as a variable and have chosen to use temperature as the primary accelerating factor in our accelerated tests. We believe that this is a reasonable assumption for the first series of tests because we do not anticipate any major chemical corrosion processes to affect the hermeticity of the package. So far, we have used temperature as our main acceleration mechanism, but in the future we will focus on other factors such as pressure and changes in the concentration of the saline solution.

Moisture diffusion through the package is an Arrhenius process, i.e. a process whose rate constant (R) has the following temperature dependence:

$$R = A \exp(-Q/kT) \quad (1)$$

Where A is a constant, Q is the activation energy, k is the Boltzmann's constant, and T is temperature in degree Kelvin. The mean time to failure which corresponds to accumulation of a critical mass of moisture at a given temperature, T , can be written as:

$$\text{Mean Time to Failure (MTTF)} = B \exp(Q/kT) \quad (2)$$

where, B =constant. The value of Q must be determined for each package. By using the MTTFs at 85°C and 95°C, we can easily calculate the activation energy (Q) and from this activation energy we can proceed to obtain an acceleration factor (AF) for these tests. The accelerating factor (AF) is defined as the ratio of MTTF under normal conditions to MTTF under stressed conditions. AF is given by:

$$AF = \frac{\text{MTTF under normal conditions}}{\text{MTTF under stressed conditions}} = e^{\left[\frac{Q}{k} \left(\frac{1}{T_n} - \frac{1}{T_s}\right)\right]} \quad (3)$$

We can then calculate the MTTF at body temperature.

In order to measure the mean time to failure of the package, we used a saline bath at different temperatures. In this test silicon substrates with dew-point sensors on them and the glass capsules were first carefully cleaned in TCE, Acetone and IPA to remove any particulate and grease. This is necessary, because even a small particle on the surface will cause nonuniform bond and eventual package failure. Then the glass capsules were electrostatically bonded to the substrates at 320°C by applying 2000V across the two structures. The bonded substrates were immersed in a saline bath at two elevated temperatures, namely at 85 and 95°C. The dew point sensors were tested every few days for any moisture condensation on their surface. This was done by pulling the substrates out of the saline bath, rinsing them in DI water, probing the pads connected to the dew-point sensors inside the package, and measuring the dew-point sensor impedance with an impedance meter. Any condensation of moisture on the surface of the dew-point sensor was detected as a decrease in the impedance and the package was considered failed at that point. The failures were also confirmed by the visual observation of condensation inside the package under microscope.

This method of testing the package is very sensitive; this is because by pulling out and rinsing the package one actually cools the package down to room temperature (25°C). Any condensation at room temperature corresponds to a certain amount of relative humidity at elevated temperature which is below the condensation point at that temperature. This can be shown by an example: consider a substrate that has been soaking at 90°C in saline, the substrate is pulled out and rinsed in DI water at room temperature. Any condensation of moisture at 25 °C corresponds to a relative humidity of 5% at 90°C. Therefore, by using this method we are actually detecting a 5% RH at 90°C. The nice feature about this technique is that it does allow one to measure very small relative humidity without the need for a humidity sensor. Of course, the disadvantage is that the substrate has to be cooled down to dew point at that particular RH value which is impractical for in-vivo testing in animals. Even though at all tests the dew point sensors have depicted failure at the correct time, they are limited due to the fact that they indicate condensation and no condensation. In the future we will fabricate humidity sensors inside the package which will monitor the humidity in the package on a more continuous basis.

In general we have conducted soak tests at two different temperatures (85 and 95°C) to find the mean time to failure and the package activation energy. These tests are performed both in De-ionized water and phosphate buffered saline. We will first mention the tests performed in the saline solution at the elevated temperatures. The following sub-section will detail the tests in de-ionized water. Then we will mention the tests in saline using protective coatings. Then, the study of devices soaked in saline at the room temperature (control group) will follow. A summary of the soak tests and a general comparison of the devices are detailed next. A dissolution study of the silicon films concludes this section.

2.2.4 Accelerated Soak Tests in Phosphate Buffered Saline

In these set of tests, we have prepared 28 packages by bonding the ultrasonically machined glass capsules to full thickness silicon substrates. 17 of these packages have been soaked at 85°C and 11 of them have been soaked at 95°C both in phosphate buffered saline. The yield was 73%. That is 3 packages in the 85°C and 5 packages in the 95°C tests failed prematurely. Most of these failures were due to misalignment of the glass to the silicon substrate. The samples at each temperature have been tested both electrically with the aid of dew point sensors inside the packages and also visually with the help of a microscope. These tests are performed every three to four days by taking the package out of its jar, cooling the sample down to room temperature and then making the measurement. The saline solution in each jar is changed daily in order to keep the concentration of the saline at a constant level. If the saline solution is not changed, at this high temperature the solution evaporates and changes the concentration of saline and hence not only leaves a residue on the glass capsules causing difficulty in visual inspection, but also enhances dissolution of the polysilicon bonding layer.

Tables 2 and 3 below summarize the pertinent data from these tests. From these high temperature tests we have found out that the polysilicon bonding layer gets dissolved at a fairly high rate. As such, the soak tests at 95°C have come to a conclusion earlier than the 85°C tests. It should be noted that the dissolution of the polysilicon is exacerbated at the high accelerated testing temperatures and is not believed to be a major cause for concern at the operating body temperature. The longest lasting package in the 95°C tests have survived a total of 70 days. The average lifetime was calculated to be 38 days. Moreover, the longest lasting package in the 85°C soak tests have lasted a total of 321 days. The meantime to failure of the samples was calculated to be 115.6 days. The calculations for the meantime to failures do not include the samples that have failed within 24 hours from the start of the tests namely because these failures are related to the formation of a poor bond between the polysilicon and the glass which is caused by particulates and defects generated during processing that reside on the bonding surface and also from the alignment errors. In the failure analysis section we will present more information about these samples. Figures 2.16 and 2.17 show lifetime data plots that illustrates the general trend.

Table 2: Key data for 85°C soak tests in saline.

Number of packages in this study	17
Soaking solution	Saline
Failed within 24 hours (not included in MTTF)	3
Packages lost due to mishandling	0
Longest lasting packages so far in this study	321 days
Packages still under tests with no measurable room temperature condensation inside	0
Average lifetime to date (MTTF)	115.6 days

Table 3: Key data for 95°C soak tests in saline.

Number of packages in this study	11
Soaking solution	Saline
Failed within 24 hours (not included in MTTF)	5
Packages lost due to mishandling	0
Longest lasting packages so far in this study	70 days
Packages still under tests with no measurable room temperature condensation inside	0
Average lifetime to date (MTTF)	38 days

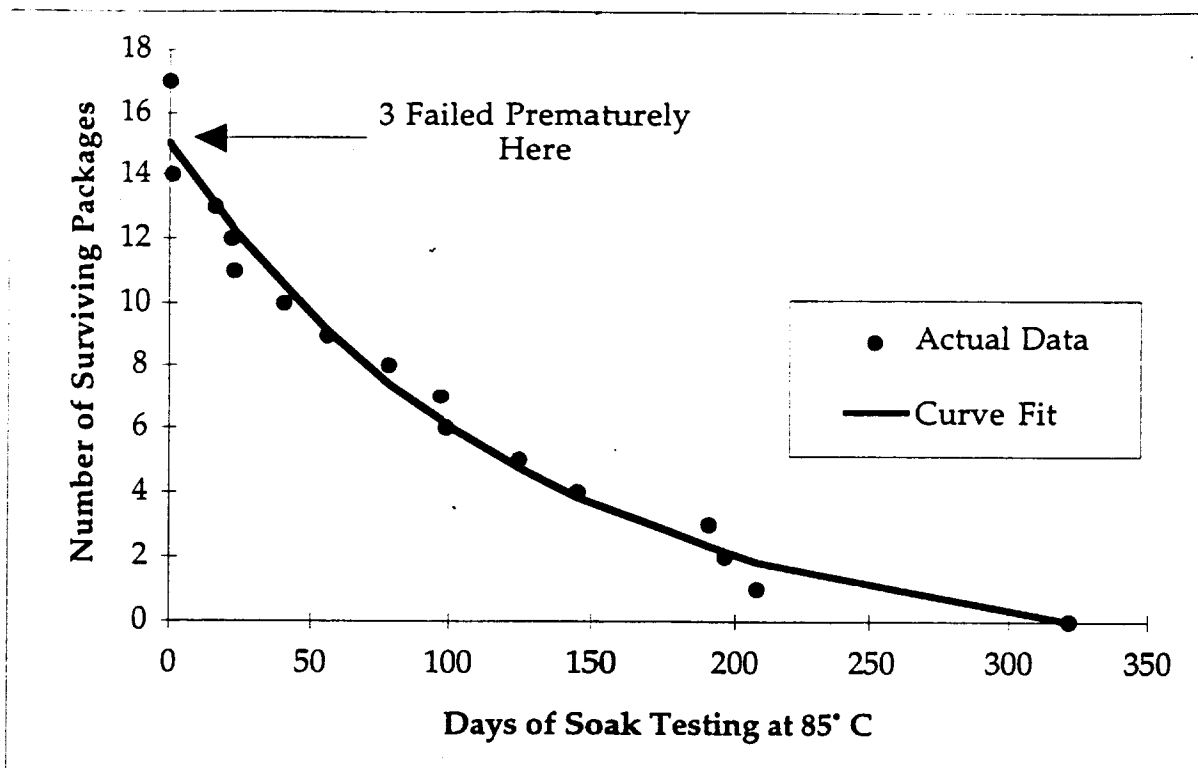


Figure 2.16: Summary of the lifetimes of the 17 packages which have been soak tested at 85°C in saline solution.

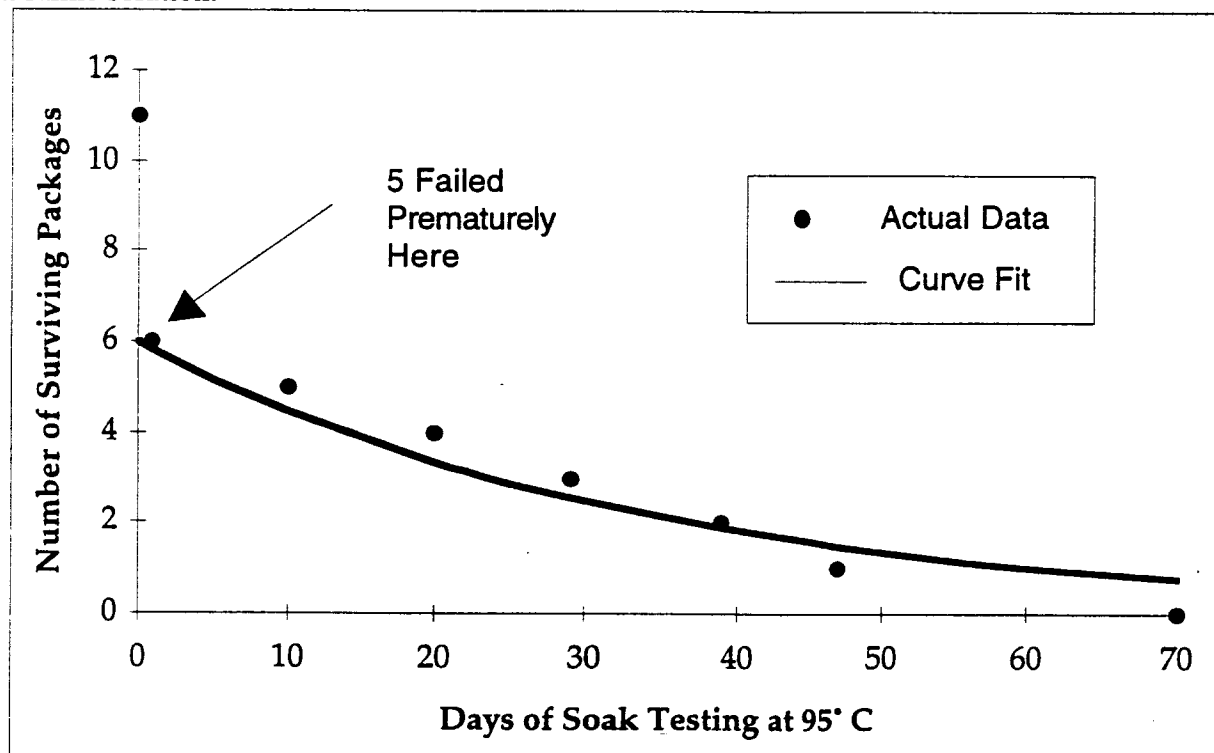


Figure 2.17: Summary of the lifetimes of the 11 packages which have been soak tested at 95 C in saline solution.

2.2.5 Interpretation of the Long Term Soak Testing Results in Saline

By using the current MTTFs at 85°C and 95°C, we then calculated the activation energy (Q) and from this activation energy we proceeded to obtain an acceleration factor (AF) for these tests, and then calculated the MTTF at body temperature. Performing this calculation yields:

$$MTTF|_{85^{\circ}C} = 115.6 \text{ Days} \quad MTTF|_{95^{\circ}C} = 38 \text{ Days}$$

$$Q = 1.26 \text{ eV}, AF(95^{\circ}C) = 1693, AF(85^{\circ}C) = 558$$

$$MTTF|_{37^{\circ}C} = 177 \text{ Years}$$

The activation energy of 1.2 eV is about what we expect for these packages. For comparison, corrosion is known to be one of the major failure mechanisms for plastic-encapsulated silicon chips, and the activation energy for corrosion of these standard plastic packages is well characterized and known to be about 0.7 to 0.9 eV. Hence our calculated average lifetime of 177 years at the body temperature is a feasible lifetime.

All of the samples that have failed in these tests have been thoroughly analyzed under a microscope and a SEM. In these set of tests we have found the dissolution of the top polysilicon layer as the main cause of failure. That is, at this high temperature the polysilicon gets etched in saline both at 85°C and 95°C. We also expected the substrate which itself is made out of silicon to be attacked and be a cause for moisture penetration. However, since in these tests the backside of the silicon substrate is coated with the LPCVD dielectrics such as oxide and nitride which do not get etched in the saline solution, and hinder the backside etching. A typical corrosion related path is shown in Figure 2.18. This sample has failed after 33 days at 85° C. As seen in the figure the saline as it dries on the bonding region leaves a dark colored residue which is easily noticeable under a microscope. It is clear that the sole source of failure for the tests in saline is the dissolution of the top polysilicon layer. In order to slow down the dissolution of polysilicon in the high-temperature saline bath, we used a biocompatible silicone coating from Nusil technology. We have found that this coating enhances the lifetime of the samples and hence started a set of new tests using this coating which will be detailed in the next section.

2.2.6 Accelerated Testing of Silicone Coated Glass Packages In Saline

Figure 2.19 shows a SEM view of a silicone-coated ultrasonically machined glass-capsule/silicon package. A total of 16 coated packages were prepared and tested: 8 packages were soaked in buffered saline at 85°C and 8 packages were soaked at 95°C. With the application of this coating the lifetime of the samples has improved significantly, compared to the tests done with the uncoated packages. The packages have been soaking for 190 days now, and 6 of them are still under test and show no sign of leakage. The packages in these accelerated tests have been monitored every few days for room temperature condensation both electrically by means of an integrated dew point sensor and also visually by the aid of a microscope.

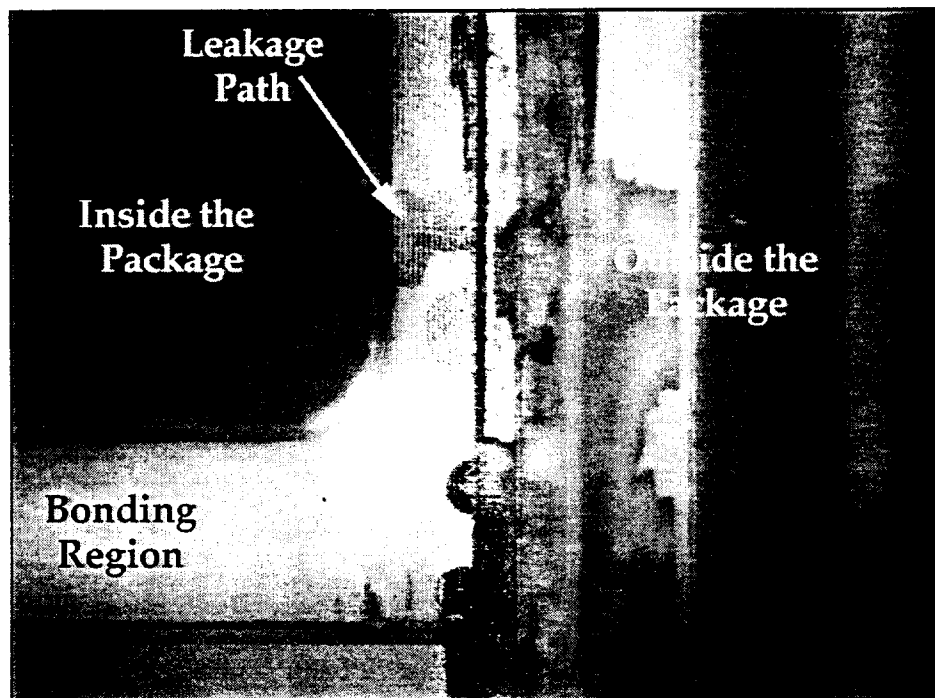


Figure 2.18: The leakage path of a sample that has leaked after 33 days in saline at 85°C.

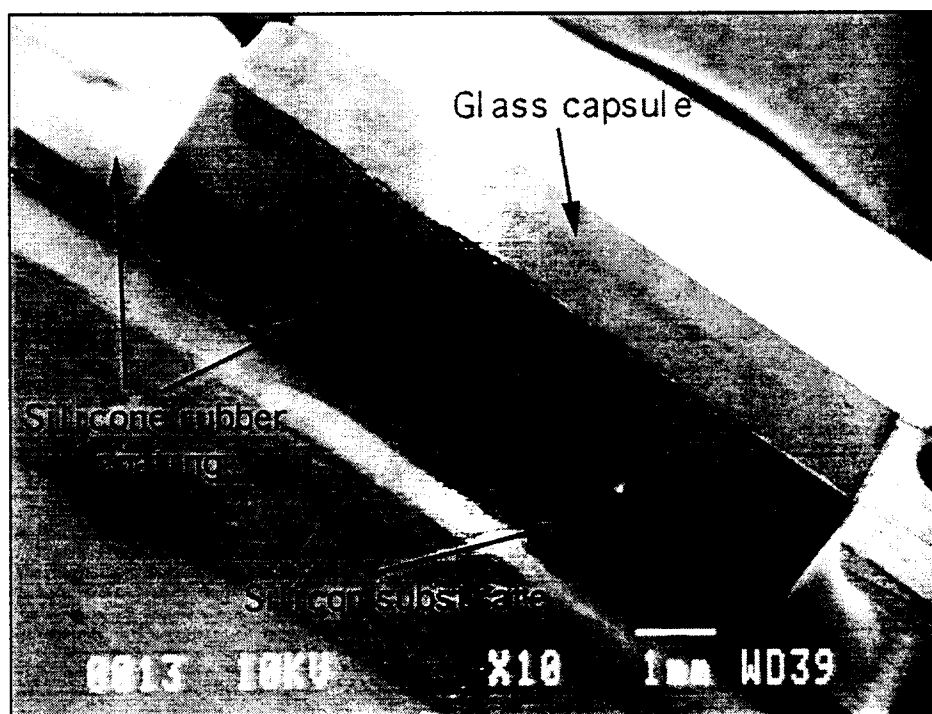


Figure 2.19: SEM of a silicone-coated glass-silicon package.

Table 4 summarizes the main results concerning the packages soaked at 85°C. Out of the original 8 packages soaked at 85°C, 1 failed after one day: this premature failure was due to a fault on the bonding surface, and this sample is not included in our calculations, for such a failure can be easily screened before implantation. From the remaining 7 packages, the first one failed after 138 days and the second one failed after 186 days. Both failures were due to a leakage path developing on the bonding surface, as shown before. Assuming that the 5 remaining packages would fail at the time of writing of this report, this would provide a Mean Time To Failure (MTTF) of 182 days, though this number is not really significant considering that 5 of the devices are still dry. However, we observe some dissolution around the edges of the devices, and some of the testing pads outside the packages (which allow us to probe the dew point sensors inside the package through the feedthroughs) have been eroded away, thus preventing us from electrically testing the dew point sensors. We were still able to monitor the humidity of the package, scanning for any moisture path by visually inspecting the bonding surface through the glass capsule and by inspecting the sides and backside of the silicon substrate. We are currently working to find ways to overcome this pad dissolution problem.

Table 4: Key data for soak tests in saline at 85° C.

Number of packages in this study	8
Soaking solution	Saline
Failed within 24 hours (not included in MTTF)	1
Longest lasting packages in this study	190 days
Packages still under tests with no measurable room temperature condensation inside	5
Average lifetime to date (MTTF)	182 days

Table 5 summarizes the main results concerning the packages soaked at 95°C. Out of the 8 packages that were soaked at 95°C, one failed after the first day because of a scratch on the polysilicon bonding surface; this sample is not included in our calculations. The first package failed after 70 days, and there is still one device which is dry after being soaked for 190 days. Assuming that this last device would fail today, this would give us an average lifetime (MTTF) of 123 days, which is a significant improvement compared to the lifetime observed for the uncoated devices at the same temperature, for which we had a MTTF of 38 and the longest lasting sample had survived a total of 70 days at 95°C (from a sample set of 11 uncoated packages). However, as can be seen in Figure 2.20, which shows a plot of the lifetime of the packages tested at 95°C, we can see that some of the devices failed because of etching through the side or the backside of the devices, which are not protected by the silicone rubber coating. This issue is discussed further in the next section concerning the different failure modes observed during those tests.

As mentioned above, because most of the packages soaked at 85°C are still dry, the MTTF calculated for those devices is not significant and cannot be used to derive the parameters (activation energy Q and constant factor A) used in our accelerated tests model equation. However, if we want an estimation of the lifetime which could be expected at body temperature, we can use the activation energy Q and the acceleration factor AF (from 95°C to body temperature) derived in the accelerated tests of the uncoated devices in saline. A MTTF of 123

days would then correspond to a lifetime of 570 years. We will be able to give a more accurate estimation after the current tests are completed.

Table 5: Key data for soak tests in saline at 95° C.

Number of packages in this study	8
Soaking solution	Saline
Failed within 24 hours (not included in MTTF)	1
Longest lasting packages in this study	190 days
Packages still under tests with no measurable room temperature condensation inside	1
Average lifetime to date (MTTF)	123 days

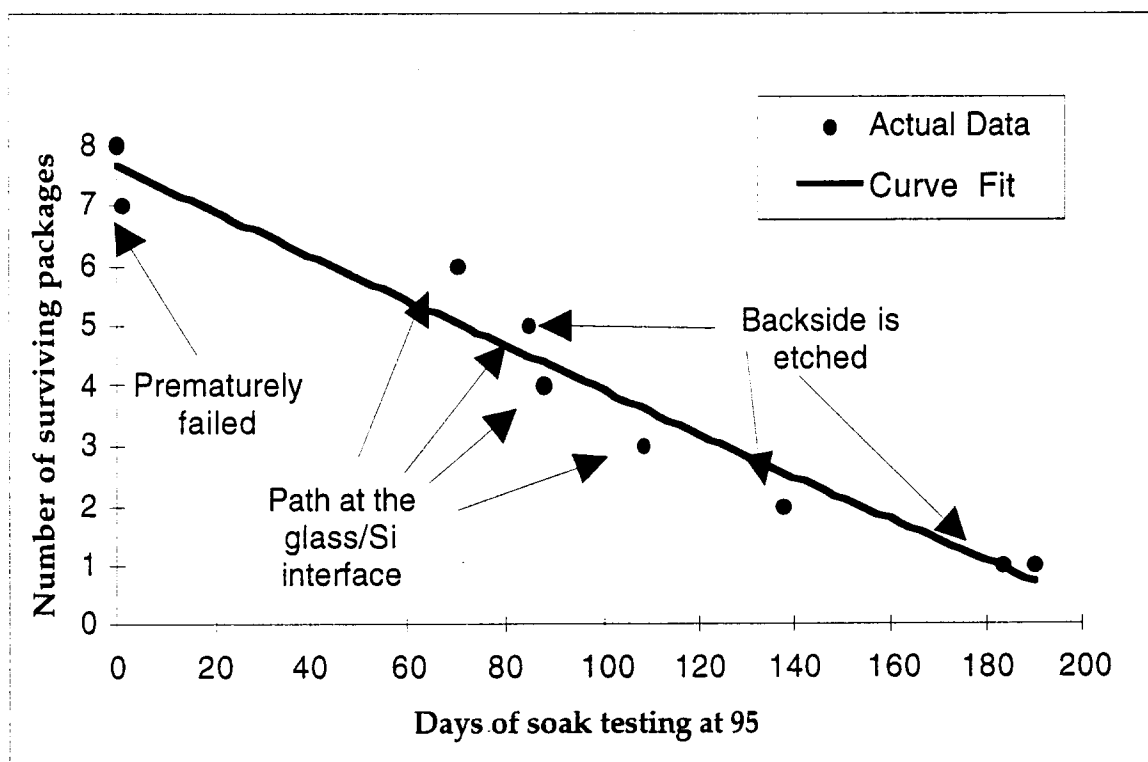


Figure 2.20: Summary of the lifetime of the 8 packages soaked in saline at 95°C.

In summary, we can conclude that the coating used in these tests was efficient in slowing down the dissolution of the polysilicon at the silicon substrate/glass bonding interface. We should also add that while applying the polymer some air molecules get trapped between the polysilicon and glass interface and when the samples have been soaked at a high temperature like 95°C, the air expands and forms bubbles. As the sample is cooled down to room temperature during measurements, these bubbles disappear and this cycling process introduces a stress to the coating. With time, this heat cycling damages the coating and finally allows the saline to penetrate to the polysilicon glass interface which starts the dissolution process. The failed sample is analyzed and as expected has a leakage path that extends across the bonding surface which strongly suggests that the sample has failed due to the dissolution of the polysilicon layer. We feel that by perfecting our technique in applying the silicone rubber to the interface and also by investigating other coatings we can reduce this dissolution process.

2.2.7 Room Temperature Soak Tests in Saline

Aside from our accelerated soak tests, we have also conducted a set of soak tests as a control group at room temperature. Admittedly, the room temperature tests will take a long time to produce meaningful data, but the results obtained this way will act as a good control study to verify the overall integrity of our package. We bonded 6 custom-molded glass capsules to thinned Silicon substrates and soaked them at room temperature in phosphate buffered saline solution. Table 6 summarizes the pertinent data from these soak tests. One of these packages failed within one day, most likely due to surface defects or poor bonding due to misalignment. Another one failed after 160 days of soaking. The remaining 4 samples are dry and still under test. These samples, similar to our other samples, are tested visually with the aid of a microscope and electrically with the help of dew point sensors integrated into the package substrate. The longest lasting sample in these tests has reached a total of 1196 days and is still under test. We have calculated a worst case mean time to failure of 982 days for these samples. We should also mention that at room temperature we are below the activation energy required to cause dissolution of polysilicon and hence as of yet have not observed any dissolution related failures.

Table 6: Data for room temperature soak tests in saline.

Number of packages in this study	6
Soaking solution	Saline
Failed within 24 hours (not included in MTTF)	1
Packages lost due to mishandling	1
Longest lasting packages in this study	1196 days
Packages still under tests with no measurable room temperature condensation inside	4
<i>Average lifetime to date (MTTF)</i>	<i>981.6 days</i>

2.2.8 Accelerated Soak Tests in Deionized Water

Early in the project, we started a number of soak tests in deionized water using custom-molded glass capsules for the package. These glass capsules were also anodically bonded to the thinned silicon substrates, as shown in Figure 2.21. The yield (calculated as the samples that last for more than 1 day) from these samples was 85%. In these soak tests, we started 10 samples

each at 85°C and 95°C. Tables 7 and 8 list some pertinent data from these soak tests. Figure 2.22 summarizes the final results from the 95°C soak tests and Figure 2.23 summarizes the results so far from the 85°C tests. These figures also list the causes of failure for individual packages when it is known, and they show a curve fit to our lifetime data to illustrate the general trend. The curve fit, however, only approximates the actual package lifetimes since some of our packages failed due to breaking during testing rather than due to leakage.

Presently, we have 2 packages soaking at 85°C. These longest going packages have lasted a total of 1284 and 1260 days are still dry and under test. For these packages we define failure as the room temperature condensation of moisture inside the package. The testing sequence for these packages start by cooling the sample to room temperature from its soak bath at the elevated temperature. The samples are next rinsed with deionized water and then dried with a nitrogen gun. We then measure the impedance of the dew point sensors and inspect the sample carefully for leakage under the microscope. The significant change in impedance (about 2 orders of magnitude) and observation of visible condensation inside the package would both be classified as the failure of the package under test. Of the original 10 samples in the 95°C tests, the longest lasting package survived for a total of 484 days. The calculated mean time to failure of these packages are 135.7 days excluding the handling errors. The mean time to failure for the 85°C soak tests (from the failed samples so far) has been calculated as 1001 days excluding the handling errors.

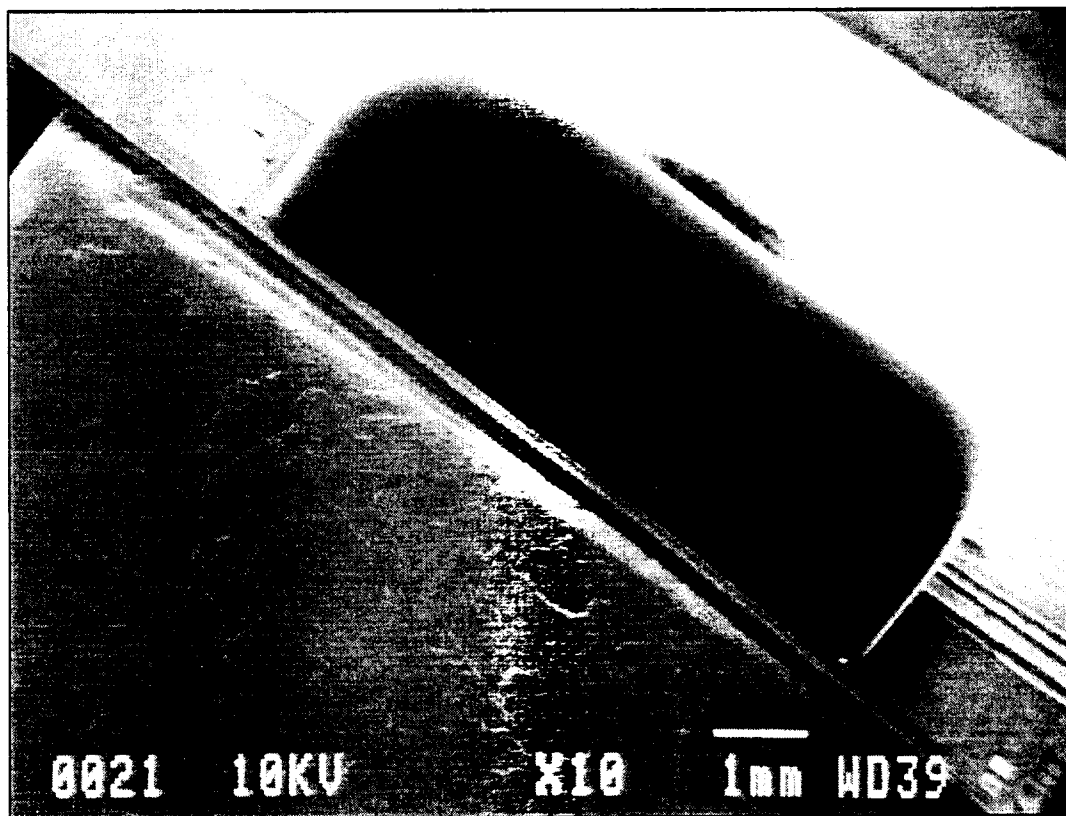


Figure 2.21: SEM view of a custom-molded Glass-Silicon package.

Table 7: Key data for 95°C soak tests in DI water.

Number of packages in this study	10
Soaking solution	DI water
Failed within 24 hours (not included in MTTF)	1
Packages lost due to mishandling	2
Longest lasting packages in this study	484 days
Packages still under tests with no measurable room temperature condensation inside	0
Average lifetime to date (MTTF) including losses attributed to mishandling	118.7 days
Average lifetime to date (MTTF) not including losses attributed to mishandling	135.7 days

Table 8: Key data for 85°C soak tests in DI water.

Number of packages in this study	10
Soaking solution	DI water
Failed within 24 hours (not included in MTTF)	2
Packages lost due to mishandling	3
Longest lasting packages so far in this study	1284 days
Packages still under tests with no measurable room temperature condensation inside	4
Average lifetime to date (MTTF) including losses attributed to mishandling	636.1 days
Average lifetime to date (MTTF) not including losses attributed to mishandling	1001.2 days

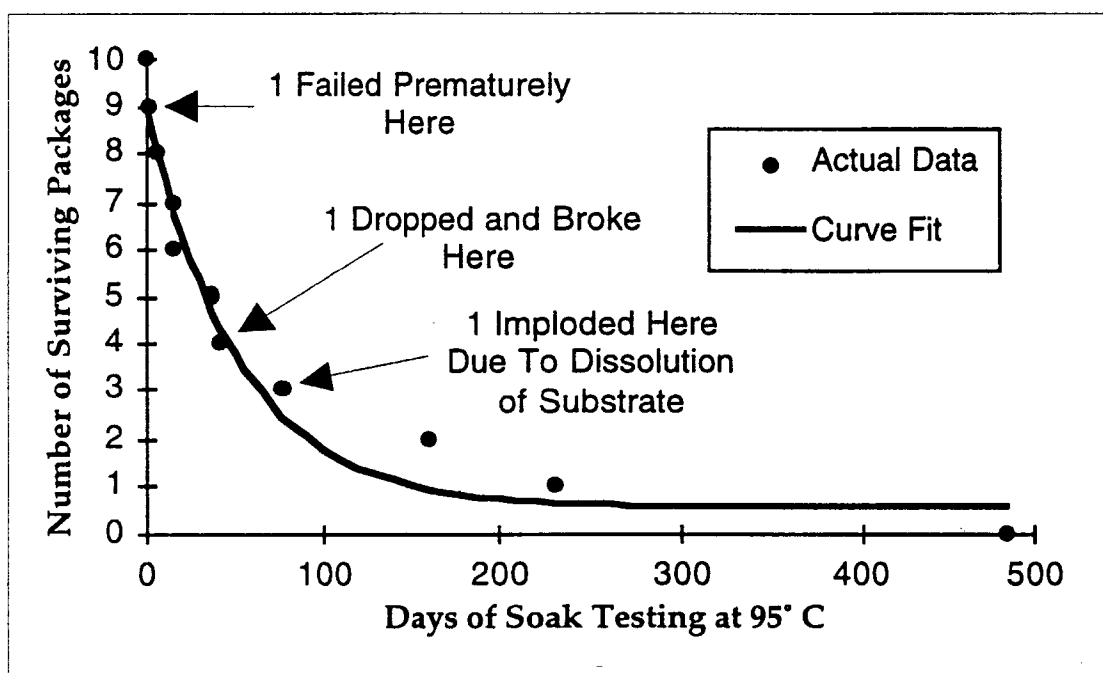


Figure 2.22: Summary of the lifetimes of the 10 packages which have been soak tested at 95°C in DI water.

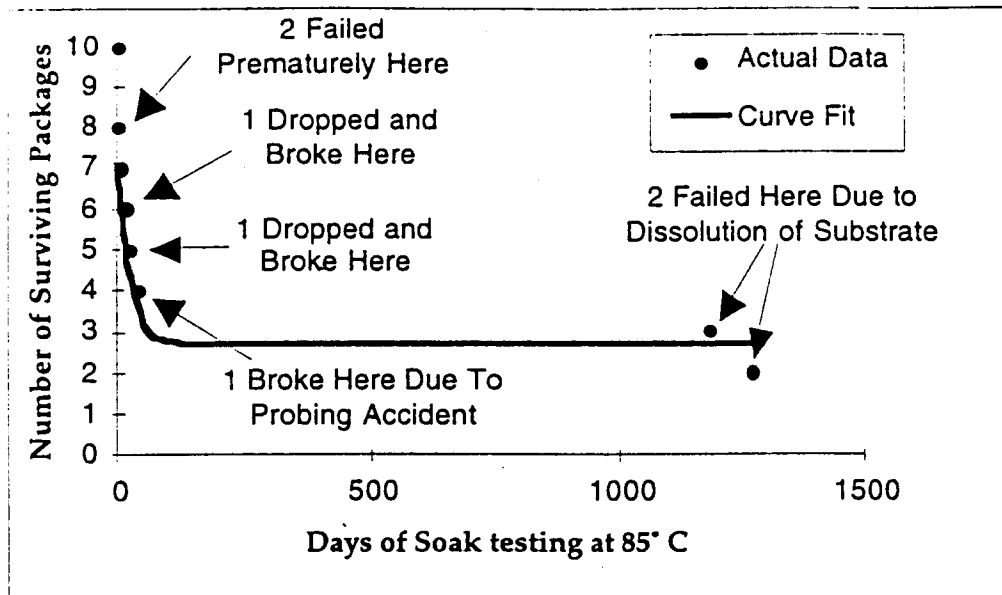


Figure 2.23: Summary of the lifetimes of the 10 packages which have been soak tested at 85° C in DI water.

By using these MTTFs at 85°C and 95°C, we can calculate the activation energy (Q) and from this activation energy we can proceed to obtain an acceleration factor (AF) for these tests, and then calculate the MTTF at the body temperature. Moreover, failed samples in the 95°C tests failed prematurely due to the enhanced dissolution rate for silicon at this temperature. Since the dissolution reaction is an exponential function of temperature, the samples at the 85°C tests have been effected less than the ones at 95°C. The model we use only accounts for acceleration of moisture diffusion, but not dissolution. For our calculations we assume that all the samples in the 85°C tests have also failed the same time as the longest going sample in the 95°C tests and proceed with the calculations as follows:

$$MTTF|_{85^{\circ}C} = 257.6 \text{ Days} \quad MTTF|_{95^{\circ}C} = 118.7 \text{ Days}$$

$$Q = 0.88 \text{ eV}, AF(95^{\circ}C) = 179.5, AF(85^{\circ}C) = 82.7$$

$$MTTF|_{37^{\circ}C} = 58.4 \text{ Years}$$

We should also note that we have included every single sample in the 85°C and 95°C soak tests in this calculation except the 15% which failed during the first day (we assume that these early failures can be screened for). Moreover, some of these capsules have failed due to mishandling during testing rather than due to actual leakage into the package. If we disregard the samples that we have attributed failure due to mishandling we obtain a longer mean time to failure:

$$MTTF|_{85^{\circ}C} = 396 \text{ Days} \quad MTTF|_{95^{\circ}C} = 136 \text{ Days}$$

$$Q = 1.217 \text{ eV}, AF(95^{\circ}C) = 1304, AF(85^{\circ}C) = 447$$

$$MTTF|_{37^{\circ}C} = 485 \text{ Years}$$

For the tests at 95°C tests, one of the main failure modes is the dissolution of the substrate also. Since the dissolution is a temperature activated process, all these samples failed sooner than the ones in the 85°C tests. We should mention that by going to a more robust and cheaper glass capsule design (ultrasonically machined ones) we have completely eliminated the handling errors. Moreover, similar to the tests in 85°C, in these tests some of the packages have failed due to handling errors. The dissolution of silicon is very enhanced at this temperature and the substrate for the longest going sample (after 484 days) actually dissolved away during soak testing leaving only residual films (oxide and nitride) and the glass capsule. In spite of these issues, the early tests in DI water still correlate well with the tests performed in saline and indicate that indeed a lifetime of many decades can be achieved with these packages.

2.2.9 Dissolution Studies of Silicon and Polysilicon in Saline and Deionized Water

As has been discussed above, we have observed silicon dissolution repeatedly in our high temperature soak tests in saline and in deionized water. We have found that silicon dissolution occurs much more slowly in DI water than in saline at high temperatures. It is important to note that we have not observed significant dissolution of silicon in saline at room temperature. Tests have been performed to measure the approximate dissolution rate of silicon and polysilicon in saline. The average dissolution rates for these samples are: 1.8µm/day at 95°C and 0.7µm/day at 85°C. The polysilicon layers get etched away with the rate of 1.6µm/day at 95°C and 0.6µm/day at 85°C. We should add that the polysilicon layers had a starting thickness of 1µm, whereas the silicon etch rates are estimated from a substrate thickness. After observing this dissolution of silicon, we performed some tests to begin characterizing it. We examined the temperature dependency of the dissolution by soaking some substrates at two different temperatures (85°C and 95°C) and examining them after 1 week for substrate thinning and surface pitting. We examined the dependency on soaking solution by soaking some in saline and some in DI water for 1 week and again examining for thinning and pitting. A summary of our observations for bare silicon substrates under all of our different soaking conditions is given in Table 9. The results of these tests indicate that the dissolution rate is a strong function of temperature, a strong function of the soaking solution, and it is not unique to our structure, nor does it appear to be faster in our structure than in bare silicon.

Table 9: Summary of the results of dissolution experiments on bare silicon.

Substrate	Soaking Solution	Temp.	Observations After 1 week of Soaking
Bare Silicon (500µm thick)	DI Water	85° C	No appreciable etching
Bare Silicon (500µm thick)	Saline	85° C	Etching just started (some inverted pyramids). Etching is particularly bad at one corner
Bare Silicon (500µm thick)	DI Water	95° C	Definite etching. Wafer surface very rough, although no inverted pyramids.
Bare Silicon (500µm thick)	Saline	95° C	Inverted Pyramids obvious from front side. Etching is particularly bad along one entire edge

It is our belief that dissolution of silicon is not significant at body temperature. Neural probes and ribbon cable have been implanted for years without observing any dissolution. It is however something to watch out for in our accelerated tests. It is a dominant failure mechanism for our high temperature accelerated soak tests in saline, and has forced us to temporarily perform our high temperature soak tests in DI water. However we would like to test our packages in as close a solution to biological as we can. For the future tests we will look into other methods to stop the dissolution of silicon and polysilicon in saline.

2.2.10 Analysis of the Failure Modes

The hermetic packages and feedthroughs that have been developed and tested under this contract require a package lifetime of more than 40 years in biological environment at body temperature. In order to improve this lifetime in a harsh body environment, a good understanding and analysis of the failure modes due to moisture is important. The failure modes discussed and analyzed below are those which were observed from all the tests that we have done up to now. The devices in these tests have been checked for moisture penetration every few days both by impedance measurements of the dew point sensors inside the package, and by visual inspection with the aid of a microscope, which allows us to look at the polysilicon bonding surface at the silicon substrate/glass interface.

The possible failure mechanisms are outlined in the Figure 2.24. As far as water outgassing from glass or silicon substrate during high temperature bonding is concerned, as well as adsorption on the internal surfaces of the package and hybrid components, these two sources of moisture penetration can be significantly reduced through proper baking and handling, for instance by vacuum baking at a vacuum level of a few torr at 200 °C for 24 hours prior to the electrostatic bonding. Also, the diffusion of moisture through the glass capsule is negligible for our applications (with a water diffusivity in #7740 Pyrex glass of $\sim 10^{-15}$ cm²/sec at body temperature, it would take tens of thousands of years for enough water to diffuse through the 200µm thick glass). We will thus consider only leakage through the polysilicon layer at the bonding interface, and the leakage through thin films or through the silicon substrate.

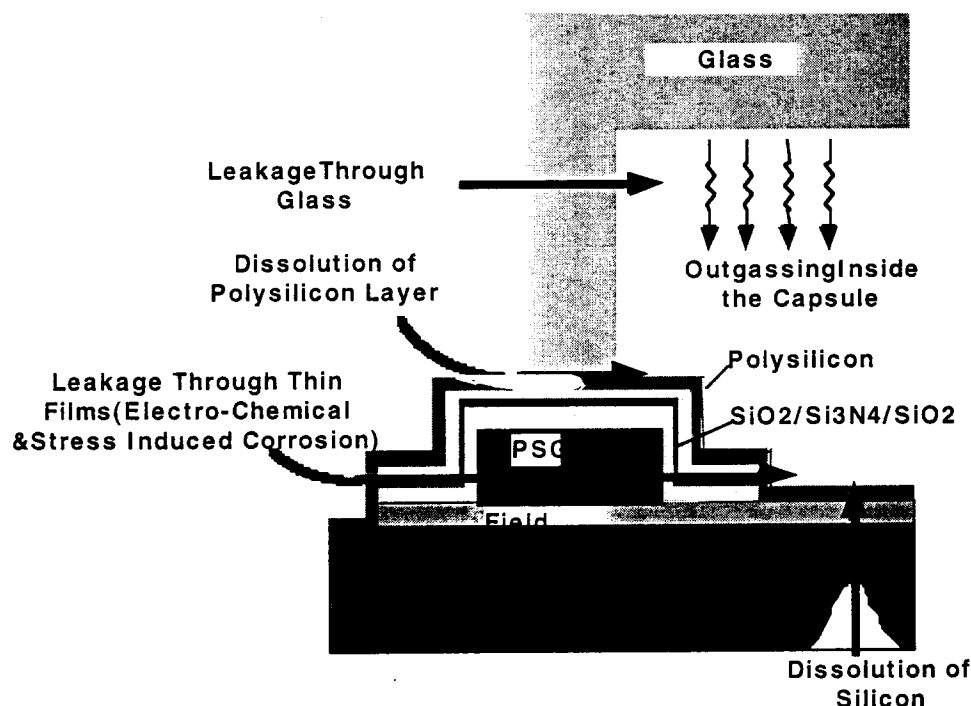


Figure 2.24: The possible failure modes for the microstimulator package.

The main failure mode observed on the packages that have failed during our tests, and that was described previously, concerns the failures attributed to the dissolution of a polysilicon layer just below the glass capsule, at the silicon substrate/glass capsule interface. The dissolution of the polysilicon layer eventually creates a path, a typical one of which can be seen on Figure 2.25a (this is the view from the top). As discussed in the previous sections, this kind of failure

has been significantly slowed down by the use of a silicone rubber coating protecting the silicon/glass interface from the environment, acting as a barrier to the ions present in the solution. Some other coating materials and techniques, will be investigated in the future.

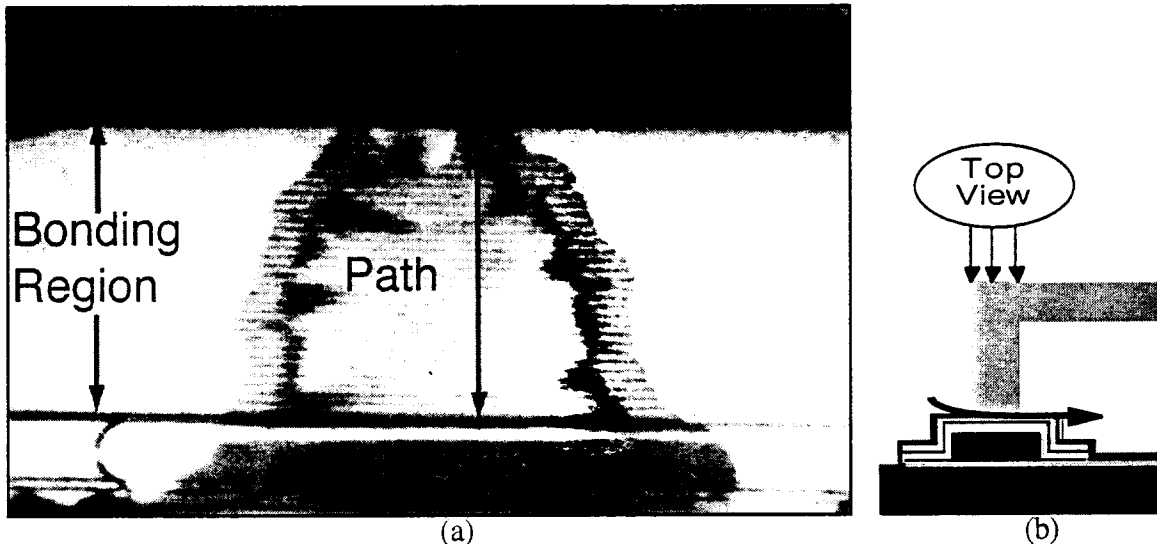


Figure 2.25: Leakage path through the interface between glass and silicon seen from top after soaking for 88 days at 95°C.

Another possible failure mode has been identified, which is the dissolution from the backside of the silicon substrate. However, it seems that the oxide layer is not significantly affected by this dissolution and thus prevents or slows dissolution from penetrating inside the package. Figure 2.26a shows a picture of the backside of the device etched to the point that we can see the inside of the package: region A shows dissolution of the backside of the substrate and of the glass/silicon interface; region B shows dissolution of the backside of the substrate only and region C shows the remaining non etched layers (the Figure 2.26b shows the way the picture is taken from the bottom). It should be noted that on the tests of the packages coated with silicone rubber (described in previously), from among the 6 devices that failed at 95°C, 3 showed backside or side etching significantly enough to create a leakage path.

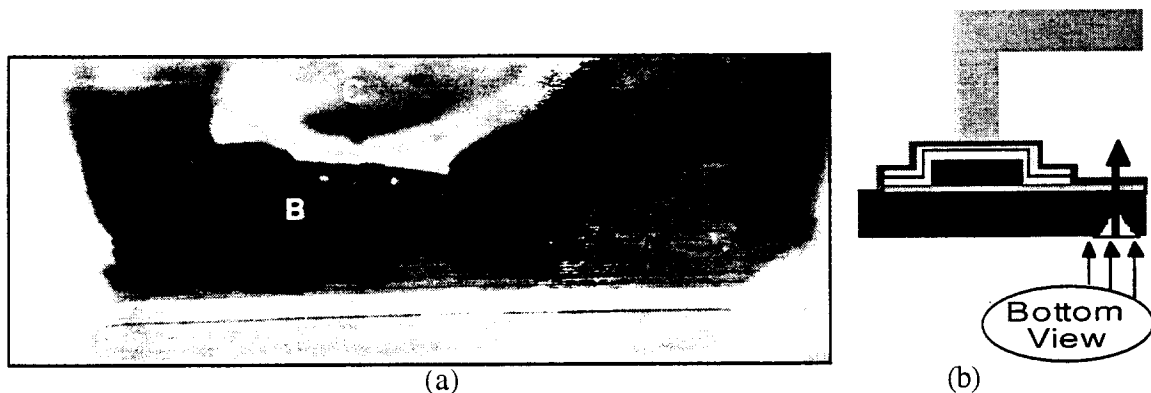


Figure 2.26: Backside view of the device.

However, concerning the dissolution of silicon and the polysilicon layer, as well as the other layers, further corrosion studies will be conducted in order to determine their effect at body temperature. Also, those studies will enable us to use more resistant materials to prevent this dissolution.

2.3 In-Vivo Testing

One of the important objectives of the contract was the testing and characterization of the silicon-glass package in animal models for determining the basic biocompatibility of the materials used. During the past three years we have provided samples of the package to several research groups around the country and have performed some preliminary biocompatibility tests in various biological environments. These groups include:

- University of Michigan (Professors D. Anderson and Wise)
- Hines VA Hospital (Drs. J. Walter and L. Riedy)
- Johns Hopkins University, Wilmer Eye Institute (Dr. M. Humayun)
- Vanderbilt University (Professor D. Zeale)

All of these tests have produced significant and very encouraging results as to the biocompatibility of the glass-silicon package. Some of these results will be discussed below.

2.3.1 Biocompatibility Studies Performed in The University of Michigan Facilities

Initial experiments were performed with 4 custom molded glass capsules bonded to thinned silicon substrates. These devices were placed on top of the dura, in an area where the skull had been cut away. The skin was then sutured together, leaving the devices sitting on top of the dura, not fixed in place. This placement is compatible with the eventual placement of the hermetically packaged telemetry platforms for applications in CNS. The Table 10 summarizes the details of these experiments.

Table 10: A summary of the in-vivo tests conducted with thinned silicon substrates.

Impl. #	Guinea Pig Number	Date of Implant	Number of Days Implanted	Gross Leakage	Device Broke During Explant	Comments
1	GP#1	1/17/95	62 days	No	Yes	Visual inspection in situ showed no sign of leakage
2	GP#1	1/17/95	62 days	No	Yes	Visual inspection in situ showed no sign of leakage
3	GP#2	2/2/95	61 days	Yes	Yes	Visual inspection in situ showed obvious gross leakage
4	GP#2	2/2/95	61 days	No	No	Only package explanted without damage. No gross leakage, but sensors detected moisture penetration.

After 2 months in-vivo, only one of the packages had gross leakage, one had a slight amount of leakage that could be detected only electrically, and the final two packages had no observable moisture inside, although the substrates broke during the explant making it impossible for us to probe the last 2 devices electrically. We believe the failures in this set of devices are probably due to excessive mechanical forces and also the fact that the substrates were thinned to a thickness of around 100 μ m. After 2 months in-vivo, all the implants have healthy tissue growing up around them. There was no sign of infection in any of the implanted animals, and no adverse effects that our histology technician could determine. The first two implants had muscle completely regrown over the entire package, and the skull had grown over the substrate and was beginning to encapsulate the glass. The second two implants had muscle and bone completely regrown over the silicon substrate, but as mentioned already the top of the glass capsule was sticking through the skin. Examination of the silicon substrate from all 4 implanted devices showed no indication of dissolution of the silicon substrate or the polysilicon films. There was no sign of etching of any of the thin films used in the packaging process.

After the fabrication of the ultrasonically machined glass capsules, we have bonded 3 and have implanted these devices into Guinea Pigs, with the results summarized in Table 11. One of the devices before the explant is seen on the dura of a Guinea Pig. With the change to the use of silicon substrates with full thickness (500 microns), the devices became much more robust and strong. As seen in the Table 11, none of them failed during the explant. We have also tested the sensors after we have explanted these devices and all the sensors indicate that the devices had been dry during the entire duration of the implants. Moreover, we have inspected these explanted devices and have seen no indication of the dissolution of any of the films on the substrate including polysilicon. In all of these implants similar to the implants done with the thinned devices, there was bone and healthy muscle tissue growing around the implanted device and there were no adverse effects.

Table 11: A summary of the in-vivo tests conducted with ultrasonically machined glass capsules bonded to full thickness Silicon substrates.

Implant Number	Animal Number	Date of Implant	Days Implanted	Gross Leakage	Device Broke During Explant	Comments
1	GP#1	10/17/97	31 days	No	No	Visual inspection in situ showed no sign of leakage
2	GP#1	10/17/97	31 days	No	No	Visual inspection in situ showed no sign of leakage
3	GP#2	10/17/97	60 days	No	No	Visual inspection in situ showed no sign of leakage

2.3.2 Biocompatibility Studies At the Hines VA Hospital

We prepared 7 packages using the ultrasonically machined glass capsules bonded to full thickness Silicon substrates. Before sending for implants these devices were soaked in deionized water at 95°C to screen for premature failures. After this they were sterilized and implanted into the bladder wall of rats and were later explanted after 1 month. The early observations by the VA team is that all the devices looked very good after explantation, lying in a thin (<0.1mm) connective tissue sheath. One of these devices was covered with silastic before the implant. The

VA team also reports that none of these devices migrated and only one suture was found through the bladder wall. The microstimulators did not adhere to the skin and simply came out of their pouch after cutting a slit with a scapula. After receiving the devices from the VA team, we cleaned the residue from over them and then inspected the polysilicon bonding surface through the glass from the top. There was no indication of a leakage path. We also soaked the devices for 2 days in deionized water at 95°C and afterwards when we examined them, we did not observe any indication of moisture inside the packages. Figure 2.27 shows a typical area on the bonding surface which indicates the absence of corrosion related paths on the top surface. Moreover, we broke one of these packages by removing the glass capsule and looked for any evidence of moisture or stains inside the package. The structures inside the package, namely the dew point sensors and the various other metal lines, had no stains and/or discoloration from moisture penetration into the package which are typical of leaked packages. With this evidence we are very positive that our packages not only stayed intact, but also were hermetic for the duration of the implant. We also inspected the packages under a scanning electron microscope. We have focused on the electrodes and the various metal lines that are exposed to the body fluids. None of these areas showed any sign of damage. We also closely observed the interface between the glass capsule and the silicon substrate for any evidence of dissolution/corrosion. No dissolution or corrosion is observed. Admittedly, these tests were very short term tests and the results can not be used to conclusively verify package hermeticity in biological environments, and its biocompatibility. However, the tests clearly indicate that the packages do possess sufficient mechanical strength and do not appear to cause any adverse reactions in the tissue.

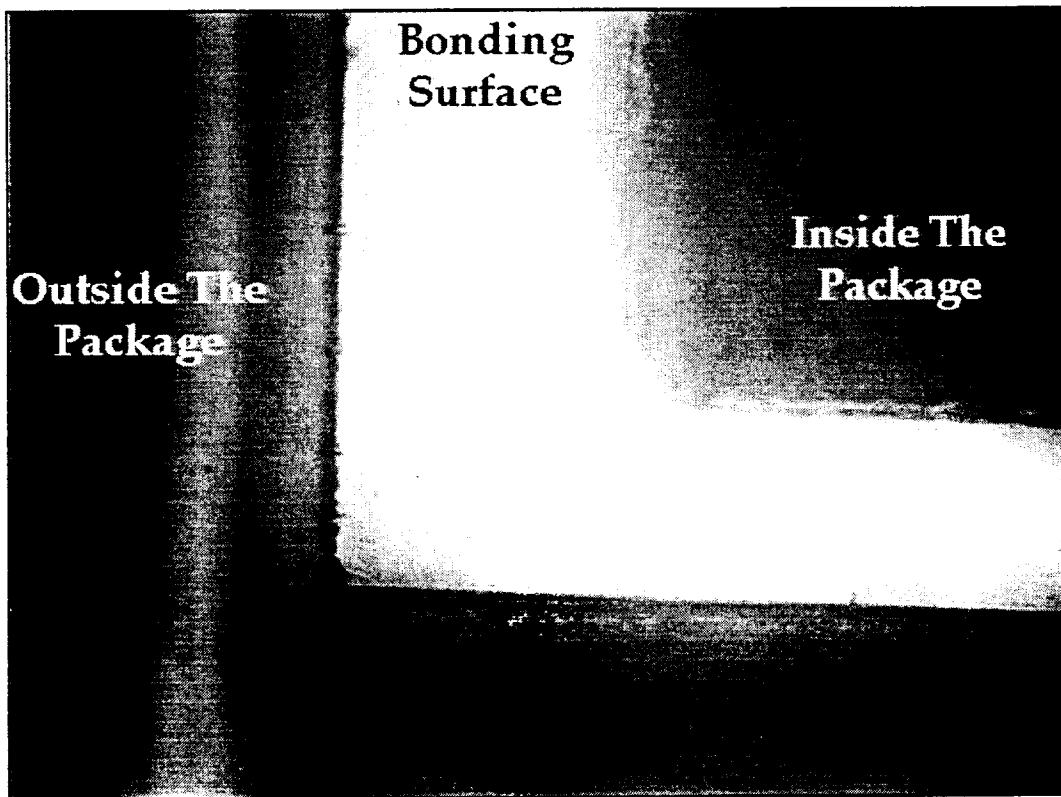


Figure 2.27: A typical region of the bonding surface indicating the absence of any leakage paths and related dissolution.

2.3.3 Animal Studies Conducted Through Consortium With Vanderbilt University

The overall goals of the consortium studies were to design a microstimulation device appropriate for reanimation of paralyzed laryngeal muscles (the openers of the voice box), and to assess the biocompatibility, positional stability and functional status of such a device. Reanimation of these muscles with an injectable microstimulator in a patient with paralysis could provide a nonsurgical method of rehabilitation, restore the airway to a patient, and prevent asphyxiation.

Design of Injectable Microstimulator

In view of the similarity between human and canine larynges anatomically and physiologically, the general configuration and dimensions of the microstimulator package were determined in five acute canine studies during the first year. After pentobarbital anesthetization, the paired posterior cricoarytenoid (PCA) muscles, the abductors of the vocal folds, were exposed and measurements made of their rostral-caudal and medial-lateral dimensions. The average values were 20 mm and 15 mm, respectively. We determined that the total length of the microstimulator package could be no longer than 15 mm so it would not extend beyond the borders of the PCA positioned along either of the muscle axes. The maximum width and thickness of the package was deemed to be 3 mm based upon the estimated gap between the muscle and its cartilage that would be available if ultimately injected into this space. Based on these measurements, two prototype devices were manufactured by the University of Michigan. The first, prototype I, was a single channel bipolar device. The second, prototype II, was a multi cathodal channel bipolar device. A multiple number of cathodes located on the pad would allow a number of different electrode leads of staggered lengths to be attached. This pigtail electrode assembly would provide the redundancy necessary to ensure activation at optimum muscle sites to produce the desired opening response.

Device Biocompatibility Studies

The biocompatibility of each prototype was determined through implantation in both rat and canine models. The goal of the study was to determine if there was any detectable tissue reaction to any material composing these two prototypes. Under halothane anesthesia, the dorsum of five rats was implanted with our first prototype device and the dorsum of an additional four rats with our second prototype device. In each rat, the device was implanted paraxially to the vertebral column in a subcutaneous pocket overlying the latissimus dorsi or trapezius muscles. Additional biocompatible materials, including type 316 stainless steel wire, Teflon sheet, and Silastic tubing (Dow Corning), were implanted under a separate incision for comparison. Each device, implanted materials, and adjacent tissue was harvested after 1 month, 6 to 9 months, or 1 year following implantation as detailed in the addendum.

In Figures 2.28 are shown sequential examples of microstimulators harvested at 1 month, 6 months, and 1 year. At a macroscopic level, there was no evidence of any inflammation, edema, or infection indicative of tissue reaction to a microstimulator, irrespective of the type implanted or the duration of the implant. Some microstimulators became encapsulated, particularly those implanted for longer than one month. The encapsulation process appeared normal, and was not suggestive of any pathological process. At a microscopic level shown in Figure 2.29, trichrome stained and Hematoxylin & Eosin (H&E) stained tissue in direct apposition to each implanted device appeared normal and showed no sign of reaction. In particular, there was no evidence of edema or inflammatory reaction as suggested by macrophage or polymorphonucleocyte (PMN) infiltration of any tissue component including epidermis (E), hair follicle (HF), muscle (M), or connective tissue (CT). Similar results were obtained with the implanted control materials.

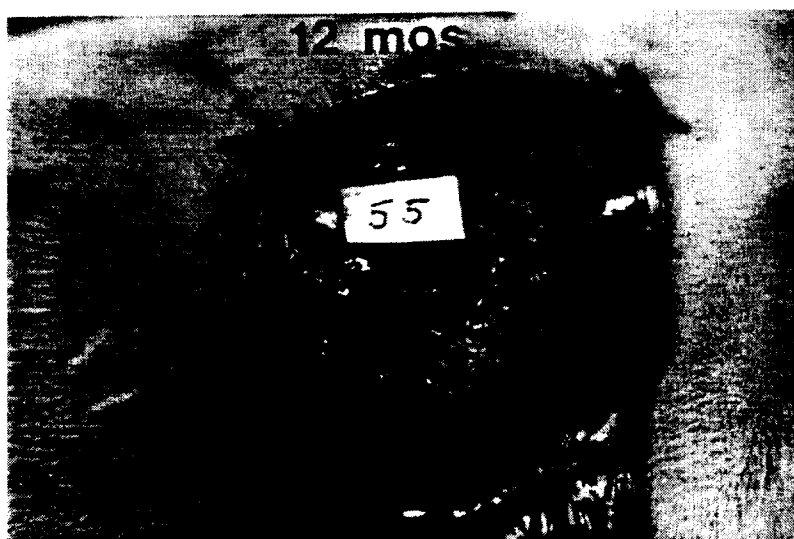
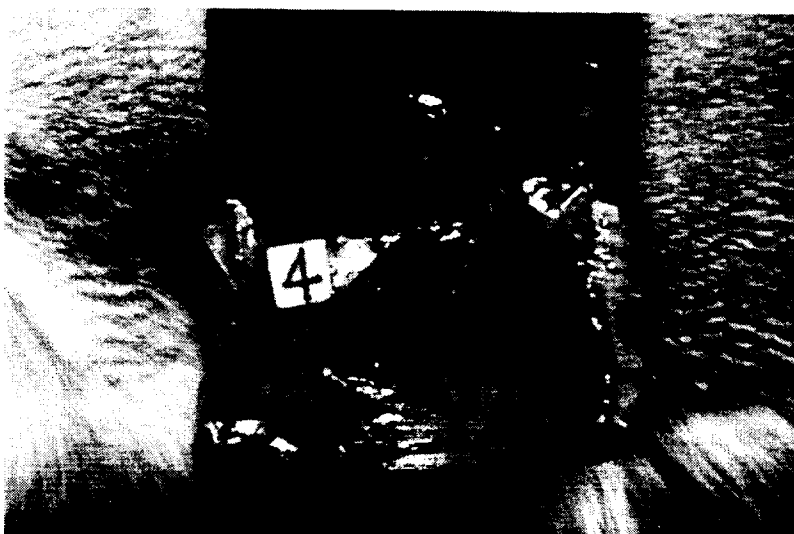


Figure 2.28: Photographs of microstimulator packages after 1, 6, and 12 months of implantation.

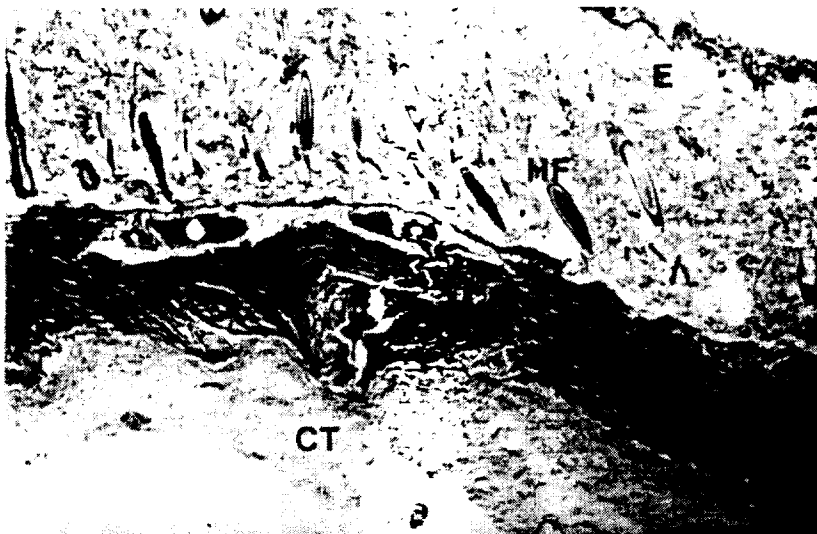
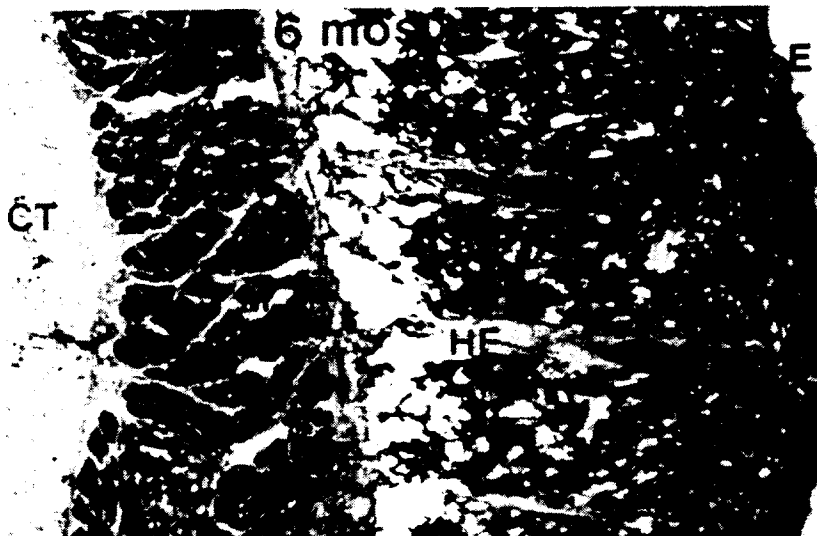


Figure 2.29: Microscopic histologic views of the biological tissue.

The biocompatibility of each prototype was examined in the canine model. Only one prototype I and four prototype II units were implanted because the multi channel device was anticipated to be the preferred configuration for eventual clinical application. Two units were implanted in direct apposition to the PCA muscle. An additional three units were positioned lateral to the larynx. This second site was chosen in the event that placement of an injected microstimulator into the posterior larynx was found to be unstable, necessitating the use of a pigtail array connected to a more laterally located microstimulator unit. The biocompatibility of the implanted devices were assessed over a period ranging from 1 to 6 weeks. Longer duration implants were not evaluated in the canine in view of the demonstrated nonreactive nature of these devices determined in the rat. Upon gross inspection, each device appeared to be normally encapsulated as observed in the rat model, without any obvious tissue reaction. Histological evaluation of tissue adjacent to each implanted microstimulator revealed no evidence of inflammatory changes as suggested by macrophage or PMN infiltration of any tissue component. In figure 6 is shown a high magnification photomicrograph of a portion of PCA muscle in direct contact to a microstimulator. Muscle fibers and extracellular matrix appeared normal in all respects.

Positional Stability of Device

In the five canines entered in the biocompatibility study, the positional stability of each device was also examined anatomically. Migration of the two devices implanted next to the PCA was measured in reference to a natural landmark, the inferior border of the cricoid cartilage. Migration of the three devices implanted outside the larynx was measured in reference to a nonabsorbable suture which served as a landmark. Each device was introduced at the implant site using a conventional and conservative surgical exposure. The extent of migration in each case was found to be directly related to the amount of dissection performed. In one case in which a large subcutaneous pocket was made, migration was measured to be 3 cm. In contrast, no discernible migration was noted in one of the other laterally located implantations in which a very limited exposure had been made. The two devices implanted adjacent to the PCA exhibited migration of 1-2 cm. These microstimulators exhibited greater migration for the amount of exposure than the laterally placed units, presumably because of the displacing forces encountered with laryngeal muscle contraction. There was no difference in the migratory tendency between the two prototype devices implanted adjacent to the PCA.

Studies of Device Function

Harnessed with information regarding the ideal microstimulator characteristics including its dimension, composition, biocompatibility, and positional stability an investigation was conducted using functional devices. The specific aims of this study were to determine if muscle contraction generated by a microstimulator was adequate to produce glottal opening, if so, what were the optimum stimulus parameters for muscle activation, and finally, were the responses stable over time. In Figure 2.30 is shown a microstimulator adapted for this investigation. A prototype II device was equipped with an array of four electrode channels distributed for bipolar stimulation. In each of six animals, a midline neck incision was made to expose the trachea and larynx. Further dissection was performed to make a tissue pocket posterior to the PCA muscles. As shown in Figure 2.31, the functional microstimulator was introduced into the pocket aided by trachea retraction. Following implantation, the incision was closed, and the wires externalized to allow connection to a peripheral stimulator for periodic activation of the chronically implanted unit. Postoperative sessions were conducted on each animal every 3-4 days over a short term of 9-10 days or a long term of 1- 1 1/2 months. In each postoperative session, the vocal fold movement generated by laryngeal muscle activation was monitored intraorally with a 0 degree endoscope.

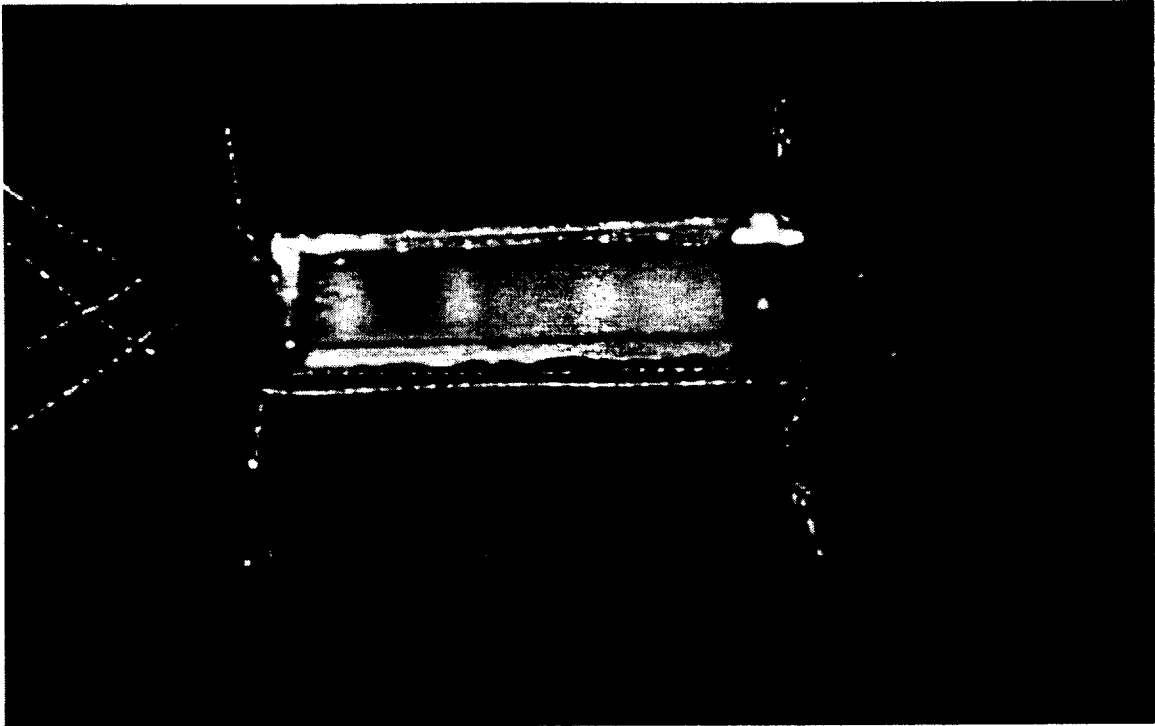


Figure 2.30: A microstimulator adapted for functional in-vivo studies.



Figure 2.31: The functional microstimulator was introduced into the pocket aided by trachea retraction.

Data was obtained from four of the six canines. In the first canine, the microstimulator extruded after implantation and no stimulated vocal fold response could be detected. In the fourth canine, the electrode leads were dislodged by the animal as discovered in the second physiological session. Of the remaining four canines, two were examined over the short term and two over the long term. Stimulated vocal fold movements were generated in all four animals in every session. The optimum stimulus parameters identified for PCA activation and vocal fold abduction were a 1 second train of 1 msec pulses delivered at a frequency of 30 Hz and an amplitude of 2-8 mA. These parameters fit within the design limitations of the second generation device manufactured by University of Michigan. Thus, it is anticipated that a fully functional second generation device, once injected, would be useful for reanimation of the paralyzed larynx. However, the practical application of this technology is predicated on the degree of stability of responses over time.

To assess the functional stability of an implanted device, the magnitude of stimulated vocal fold movement was measured through the endoscope as illustrated in Figure 2.32. In the upper left frame, the left and right vocal folds can be observed at rest in the absence of stimulation. As shown in the upper right frame, stimulation produced abduction of the left vocal fold in the first session on the animal, using any combination of electrode channels (i.e. channel configuration). The magnitude of displacement from the midline was measured using a laser ruler for calibration. Calibration was required because of changes in magnification of the image resulting from movement of the endoscope relative to the vocal fold. The distance between the laser spots shown in each frame was six millimeters. In a subsequent session on the animal, the nature of the response changed dramatically from a primarily left sided movement to a right sided movement, depending upon the electrode configuration used. In the lower left frame, opening of the right vocal fold was noted without any movement of the left vocal fold. Finally, in a later session, stimulation produced a bilateral adduction with a net closing of the airway in some cathode-anode electrode configurations.

From these initial observations, it became apparent that a detailed quantitative assessment of the changes in stimulated vocal fold movement that occurred due to microstimulator migration would be desirable. As illustrated in Figure 2.33, the magnitude of right and left vocal fold displacement was measured over the entire range of stimulus intensities and plotted as a percent change from each vocal fold's resting position. Left vocal fold abductions were plotted as positive values, while right vocal fold abductions were plotted as negative values. Using this graphical format, left and right vocal fold behavior could be appreciated independently. For example, in Figure 2.33, the responses obtained during sequential sessions in an animal using a single electrode channel configuration demonstrated functional migration of the implant. The response in the initial session #1 was a left sided abduction, which gradually changed to a bilateral abduction by session #3, and ended as a predominantly right sided abduction in the terminal session #6 on the animal. The probability of an opening response from either left or right vocal fold displacement could be obtained by measuring the area between the curves over the entire dynamic range of stimulus intensities. This measurement of response area ignored microstimulator migration from one PCA to the other, but was reflective of possible migration outside of the effective activation zone for glottis opening. In each session on an animal, the average response area over all six stimulus configurations was calculated and plotted as a function of time. Values were normalized to the maximum area observed over the course of investigation on an animal, which provided an index of the relative magnitude or probability of glottis opening. As illustrated in Figures 2.34 and 2.35, glottis opening decreased in all animals during the first ten days post implant. This was the most likely period for microstimulator migration because tissue fibrosis and scarring was still in progress and possible inadequate for microstimulator stabilization.

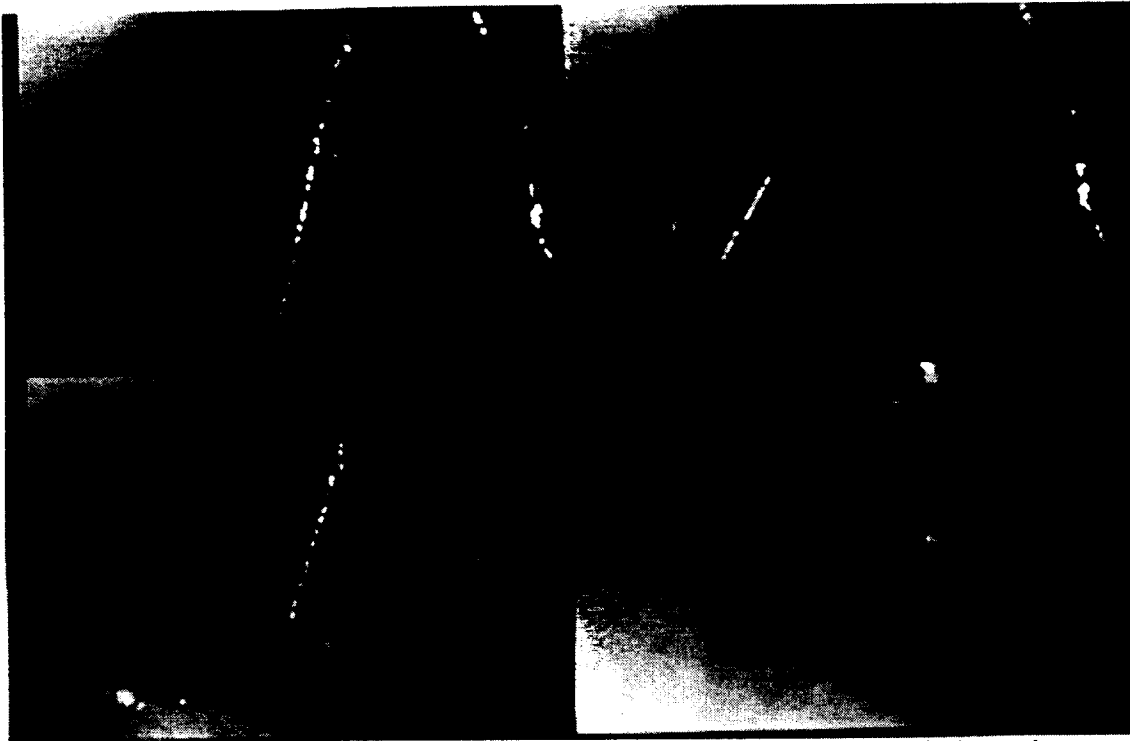


Figure 2.32: Observed magnitude of stimulated vocal fold movement through the endoscope.

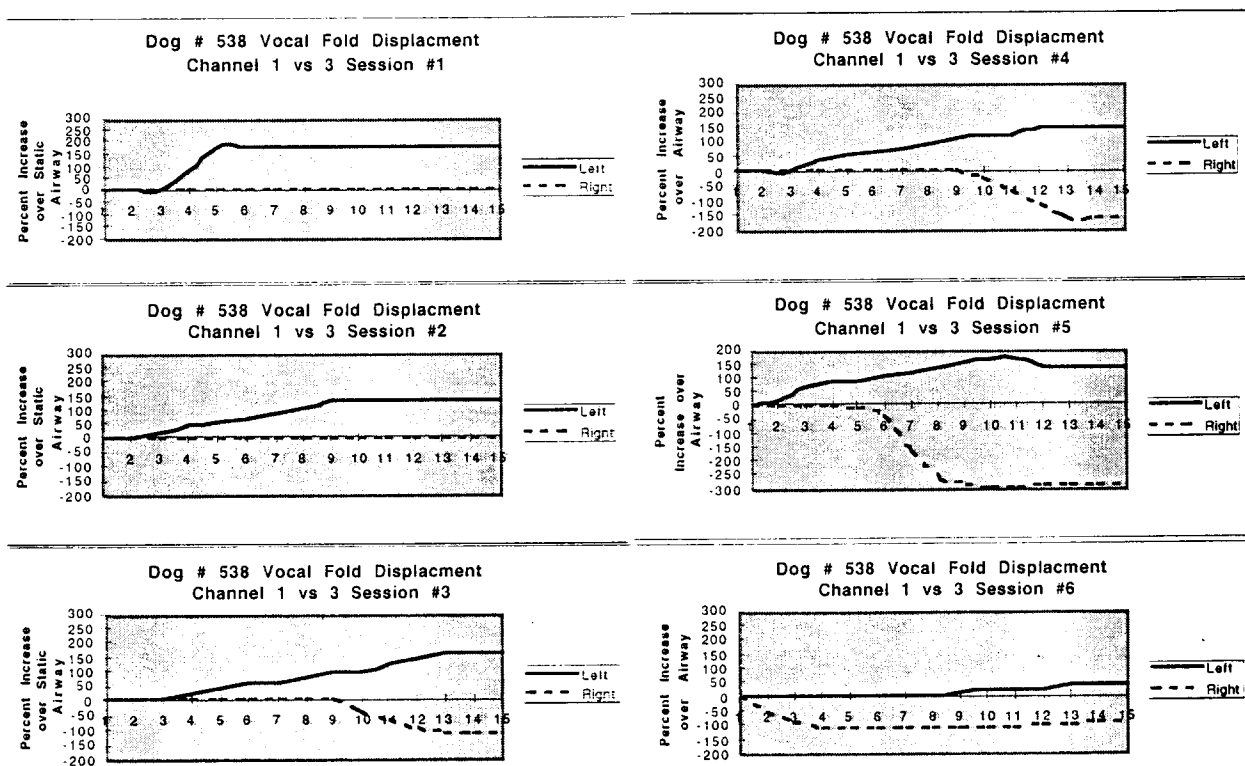


Figure 2.33: Measured magnitude of right and left vocal fold displacement over the entire range of stimulus intensities and plotted as a percent change from each vocal fold's resting position. Left vocal fold abductions are plotted as positive values, while right vocal fold abductions are plotted as negative values.

MICROSTIMULATOR MIGRATION: PHYSIOLOGIC ASSESSMENT

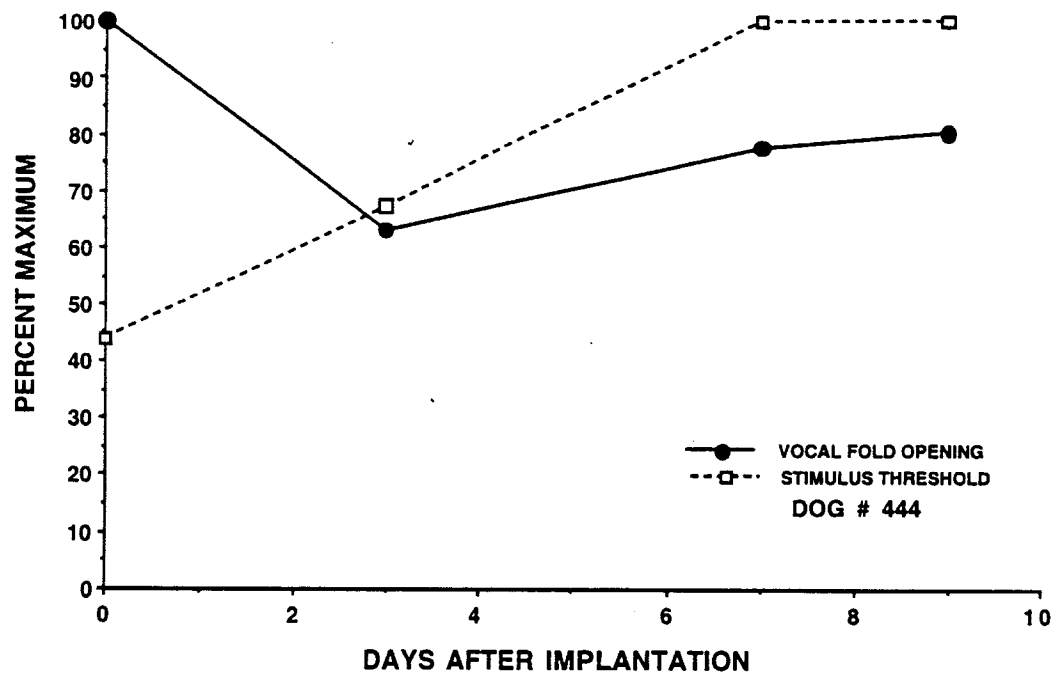


Figure 2.34: Measured glottis opening during short-term studies.

MICROSTIMULATOR MIGRATION: PHYSIOLOGIC ASSESSMENT

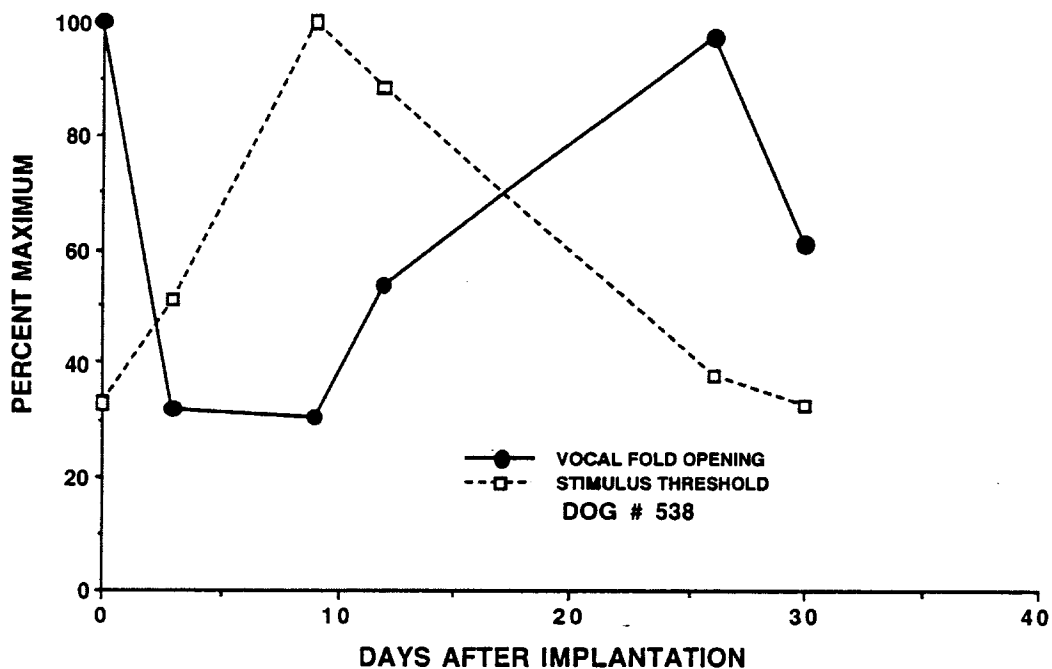


Figure 2.35: Measured glottis opening during long-term studies.

The short term studies were conducted to evaluate migration during this period of time. As shown in Figure 2.34, glottis opening dropped to 65 % by 3 days post implant, and then rebounded to 80 % by day 10. The decrease in response could be attributed to device migration. However, it was more likely a reflection of a change in the effectiveness of the applied stimulation. In particular, the stimulus thresholds increased over the first ten days in every animal, presumably due to postoperative tissue edema. The significance of postoperative edema on the stimulated response was more clearly noted in the long term studies. As illustrated in Figure 2.35, the decrease in response during the first ten days post implant was correlated with a temporary increase in stimulus threshold level. After the threshold returned to normal, the opening response also approached 100 %, indicating no functional migration outside of the PCA activation zone.

At the terminal physiological session on each animal, the microstimulators were harvested. Anatomical measurements of migration were within the range previously observed for nonfunctional devices (i.e. 0.5-2 cm). In Figures 2.36 and 2.37 photographs of the short term and long term microstimulators from Figures 2.34 and 2.35 are shown. The short term microstimulator was found to be intact, while the capsule of the long term microstimulator was breached. The hermetic seal of the capsule was broken in another functional microstimulator as suggested by the presence serosanguinous fluid within the capsule. Since all other microstimulators, with only one exception, were found intact, it was believed that the modification of package for functional studies made it more vulnerable.

Device Integrity Studies

The integrity of the microstimulator package was grossly evaluated with an operation microscope at Vanderbilt University. A more detailed assessment of the capsule hermetic seal and overall integrity was performed at the University of Michigan. Eight of the nine units harvested from the rat showed no evidence of structural damage. The ninth device showed a fracture of the silicone base extending beyond the capsule. There was no indication that damage occurred during either implantation or harvesting, so it was assumed that the damage was sustained in vivo. The damaged unit was a prototype II which had a significantly longer base extension, making it more vulnerable to intrinsic or extrinsic stresses during animal movement.

After devices were received from the Vanderbilt team, we inspected them and observed that the devices were covered with tissue around them. In order to remove this tissue without damaging our samples, we have soaked these samples at 95°C for several hours in deionized water. After this soaking step the tissue became very soft and was peeled off with a tweezer. We next took pictures of each device one of which is shown in Figure 2.38. This device after cleaning was intact and most of the films were present on the sample. Table 12 summarizes our findings from these explanted samples along with the durations that they were implanted.

We have carefully inspected these set of samples after cleaning. We have found out that the polysilicon is being attacked in some of these samples especially for the ones that have been implanted for more than 6 months. We should also be very cautious with these inspections because we have soaked these samples in deionized water at 95°C both before sending for implant to screen for premature failures and also after the explant to soften the tissue surrounding the devices before inspection. It is very possible that the polysilicon is attacked during these screening tests. As mentioned before we have done a set of 4 implants in Michigan each of them lasting for 2 months, but we have never observed any attack on the polysilicon. Similar to the implants performed in Michigan, the thinned samples had been damaged both during the implant and also during handling before and after the implant.

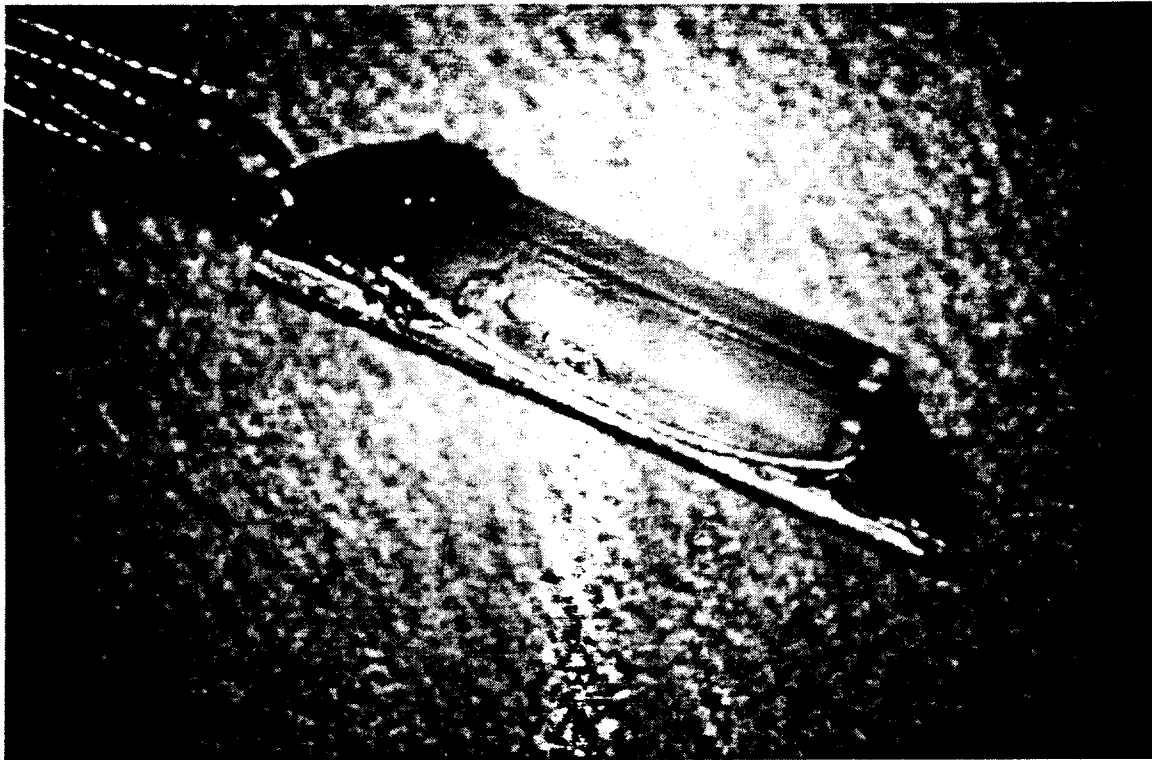


Figure 2.36: Photograph of the short term tested package of Figure 2.34.

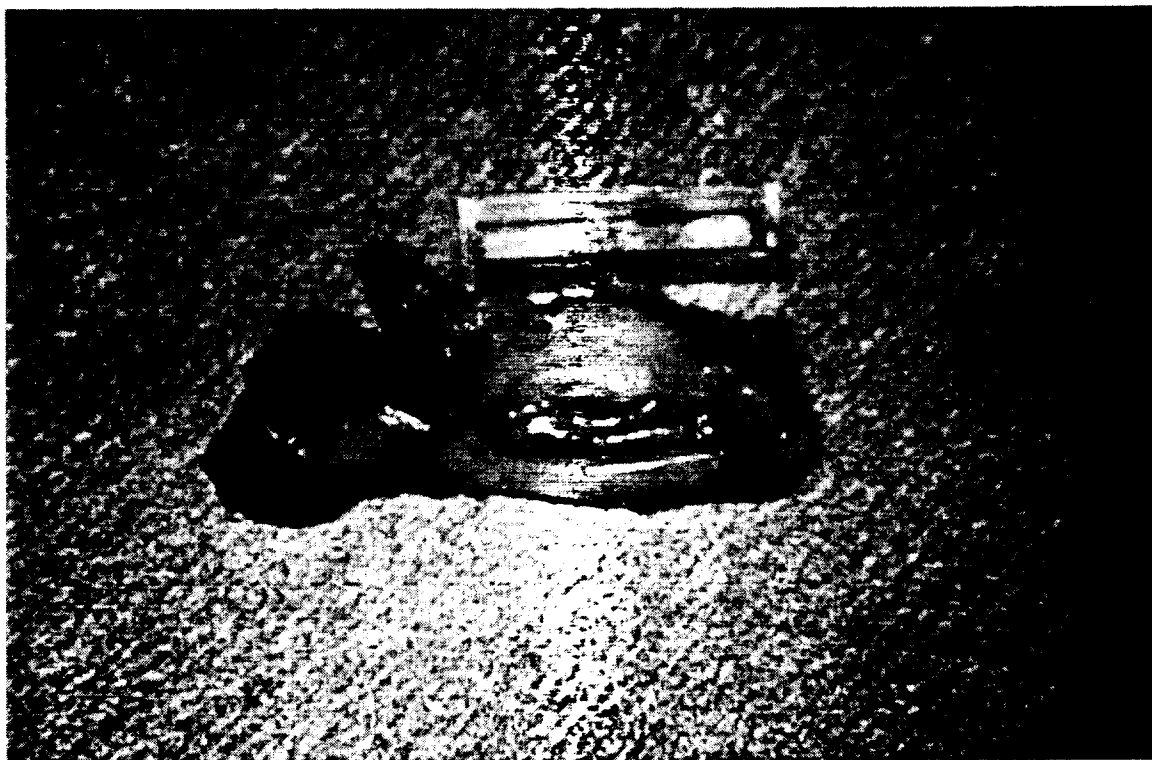


Figure 2.37: Photograph of the long-term tested package of Figure 2.35.



Figure 2.38: Photograph of one of the explanted devices after it is cleaned.

Table 12: The Summary of the samples implanted in Vanderbilt University.

Sample No	Thinned	Duration of Implant	Poly is attacked?	Dry or wet?	Intact or broken?
23	Yes	1 month	No	Wet	Intact
2	No	12 months	Yes	Dry	Intact
3	No	12 months	Yes	Dry	Intact
51	Yes	1 month	Yes	Wet	Intact
1	No	1 month	No	Dry	Intact
53	Yes	9 months	Yes	Wet	Intact
54	Yes	9 months	Yes	Dry	Intact
52	Yes	1 month	Yes	Dry	Intact
55	Yes	11 months	Yes	Dry	Intact
4	No	6 months	Yes	Wet	Broken
727	No	1 month	Yes	Dry	Intact

Summary Of In-Vivo Tests At Vanderbilt

In summary, a single channel and multi channel microstimulator appropriate for injection and reanimation of the paralyzed larynx has been designed. The biocompatibility of both prototypes has been confirmed in the rat dorsum and canine larynx as long as one year of implantation. The devices had sufficient long term durability, since 13 of 14 devices were harvested intact without any structural damage or breach of the package hermetic seal. To prevent fracturing of the silicon base, which occurred in the 14th device, a thicker substrate might be needed. The anatomical stability of implanted units was marginal, in large part, because the units were implanted rather than injected. Dissection created cleavage planes in the connective tissue and provided a pathway for device extrusion. It is anticipated that injected microstimulators requiring no surgical dissection would exhibit superior positional stability. Once these microstimulator packages are equipped with second generation device circuitry, it would produce vocal fold opening similar to that observed in the functional studies in the canine. These devices should also have sufficient functional stability for this clinical application, since an abductory response persisted through the initial days following implantation, during which a device would be most vulnerable to migration. However, the functional stability of this device in other applications would have to be assessed on an individual basis.

Summary Schedule Of Animal Experiments

RATS

The devices were implanted in a subcutaneous pocket overlying the muscle tissue paraxially to the vertebral column in the left side.

Implantation Dates

6/15/95 Prototype I devices were implanted in rats # 51, 52, 53, 54, 55:

Note: Different materials were used as control and implanted using separate incisions in rats # 53, 54, 55 with each rat receiving each of the following:

- 316 stainless steel wire
- Teflon sheet
- Silastic tubing (Dow Corning)

4/8/96 Prototype II devices in rats # 1, 2, 3, 4

Rats # 1, 2 were implanted with Prototype device II and with the control materials noted above

Rats# 3, 4 were implanted with Prototype device II

Harvesting Dates

7/15/95 Prototype device I and surrounding tissue harvested from rats # 51 and 52 after one month

3/21/96 Prototype device I, control materials, and surrounding tissue harvested from rats # 53 and 54 after nine months

5/16/96 Prototype device I, control materials, and surrounding tissue harvested from rat # 55 after eleven months

Prototype device II, control materials, and surrounding tissue harvested from rat # 1 after one month

10/19/96 Prototype device II and surrounding tissue harvested from rat # 4 after six months

4/29/97 Prototype device II, control materials, and surrounding tissue (rat #2) harvested from rats # 2 and 3 after one year

Prototype I

Rats # 51, 52

Rats # 53, 54

Rat # 55

Implantation Dates

6/15/95

6/15/95

6/15/95

Harvest Dates

7/15/95 (one month)

3/21/96 (nine months)

5/16/96 (eleven months)

Prototype II

Rat #1

Rat #2

Rat #3

Rat #4

Implantation Dates

4/8/96

4/8/96

4/8/96

4/8/96

Harvest Dates

5/16/96 (one month)

4/29/97 (one year)

4/29/97 (one year)

10/16/96 (six months)

DOGS

The devices were implanted in several different locations depending on the dog

Implantation Dates

7/25/97 Prototype device I implanted in dog # 727 in plane between the skin and strap muscles on the right side

7/28/97 Prototype device II implanted in dog # 23 in the vicinity of the right posterior cricoarytenoid

7/31/97 Prototype device II implanted in dog # 763 after attachment of electrodes behind the right posterior cricoarytenoid

8/11/97 Prototype device II implanted in dog # 71 after attachment of electrodes behind the right posterior cricoarytenoid

2/2/98 Prototype device II implanted in dog # 508 along the lateral border of the trachea on the right in proximity to the right posterior cricoarytenoid

2/2/98 Prototype device II implanted in dog # 502 adjacent to the right posterior cricoarytenoid

2/7/98 Prototype device II implanted in dog # 538 after attachment of electrodes behind the left posterior cricoarytenoid

2/9/98 Prototype device II implanted in dog # 546 after attachment of electrodes behind the left posterior cricoarytenoid

2/28/98 Two Prototype devices II implanted in dog # 573. First device implanted behind left PCA after attachment of electrodes. Second device implanted lateral to larynx.

3/2/98 Prototype device II implanted in dog # 444 after attachment of electrodes behind the left posterior cricoarytenoid

Harvesting Dates

8/26/97 Prototype device I and surrounding tissue harvested from dog # 727

8/5/97 Prototype device II harvested from dog # 763

8/27/97 Prototype device II and surrounding tissue harvested from dog # 23

9/22/97 Prototype device II not able to be harvested from dog # 71

2/20/98 Prototype device II harvested from dog # 546

2/26/98 Prototype device II and surrounding tissue harvested from dog # 508

2/26/98 Prototype device II and surrounding tissue harvested from dog # 502

3/9/98 Prototype device II harvested from dog # 538

3/10/98 Two Prototype devices II and tissue surrounding nonfunctional device harvested from dog # 573

3/11/98 Prototype device II harvested from dog # 444

Note: All procedure/surgery records from the dogs not included, but available upon request.

The microstimulator used in dog # 71 was the one harvested from dog # 763 which had to be sacrificed due to complications.

Dog #'s 71, 538, 573, 444, underwent successive procedures to stimulate the PCA via electrodes attached to the microstimulator and to study functional stability.

Data from dog # 546 incomplete due to breach of electrode lead wires.

3. Implantable Wireless Microstimulation Systems

3.1 Single Channel Microstimulators

A FNS stimulation system has been developed under this contract called the microstimulator. The microstimulator is about 3 orders of magnitude smaller than conventional implantable stimulation systems that contain multiple discrete components. This device is one of the first wireless FNS systems which is small enough to be injectable. It measures 2 mm by 2.2 mm by 10 mm and is shown in Figure 3.1. It is wireless because it uses RF telemetry to generate power and to receive data. It stimulates with a 10 mA current pulse of a programmable duration of up to 200 μ s. The specifications for the microstimulator are given in Table 13.

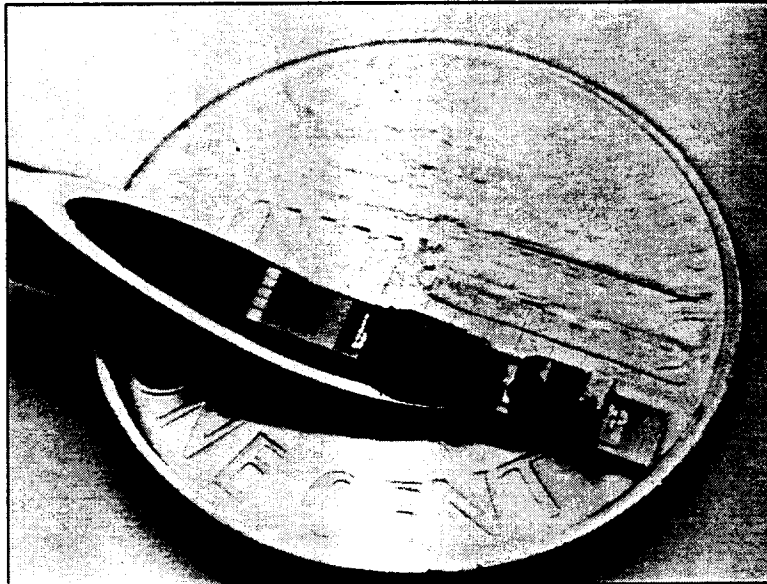


Figure 3.1: Photograph of the single channel microstimulator. This device is shown in the lumen of a hypodermic needle. The glass capsule which provides a hermetic cavity for the circuitry is lying next to the implant so that the components inside can be easily seen.

Table 13: Single channel microstimulator specifications

General	
Device Dimensions = 2.0 mm X 2 mm 10 mm	Power Delivery = Telemetry
Power < 24 mW from 8 V supply	On-Chip Regulated Supply = 8V, 4V, Gnd
Biocompatible Hermetic packaging Operational In-Vivo for Ten Years @ 37 °C	
High Current Thin Film Micro-electrodes Capable of delivering 2 μ C of charge	
Telemetry Link	
Receiver Coil = discrete solenoid (1.2 mm dia.)	Carrier Frequency = 2 MHz
Transmitter Coil = solenoid, air core (9 cm dia.)	Modulation Frequency = 2 kHz to 10 kHz
Modulation = ASK, Pulse width encoded	
Range = Anywhere inside 9 cm diameter transmitter coil	
Device Addressability = up to 32 individually addressable devices per transmitter	
Stimulation	
Stimulation waveform = 10 mA stimulating pulse followed by 100 μ A charge balancing pulse	
Duration (stimulating phase) = up to 200 μ s	Output Channels = 1
Stimulation Frequency \leq 40 Hz	Maximum Output Load = 800 Ω

The components which make up the microstimulator are illustrated in Fig. 3.2. There are 5 major components. First, a silicon substrate containing two iridium-oxide thin-film stimulating electrodes forms the base of the device. These electrodes have been tested and shown to withstand over 5 years of chronic stimulation with minimal performance degradation. The second component is an integrated circuit chip which contains about 1,200 transistors. This chip contains the full RF receiver circuitry, the digital control logic, and the stimulating output circuitry. The third component is a discrete RF receiver coil. This 50 μH solenoid coil receives power and data by inductive coupling. The fourth component is a discrete 700 nF capacitor. The capacitor serves two purposes, first it provides the output current during stimulation, which reduces the peak current draw on the telemetry link, and secondly it serves as a blocking capacitor ensuring that the electrodes remain properly charge balanced. The final component of the microstimulator is a glass capsule which is electrostatically bonded to the silicon electrode substrate to form a hermetic encapsulation for the circuitry.

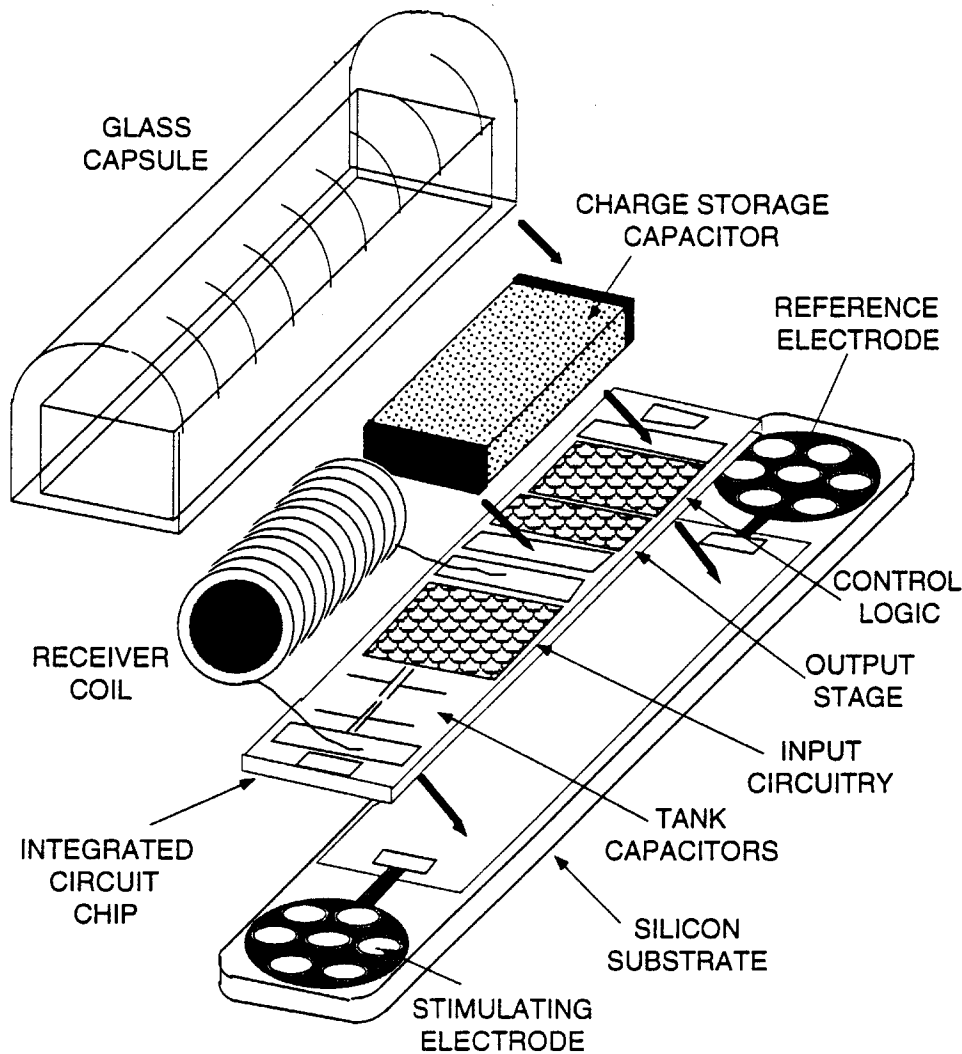


Figure 3.2: Overall construction of the single channel microstimulator.

Recently we fabricated working single channel microstimulators which consume 2/3 of the power of earlier microstimulators. This was done by redesigning the circuitry to reduce power and by changing some layout design rules to reduce leakage. The stimulating output current source was also redesigned to be better regulated and to have an adjustable amplitude. Note that the capabilities and reliability of the microstimulator has not been affected in any way

by the redesign. The microstimulator is still capable of delivering $2\text{ }\mu\text{C}$ of charge in $200\text{ }\mu\text{s}$ pulses at 40 Hz . The redesigned circuitry was fabricated and our testing shows that it works nicely. We now have ample working single channel microstimulator circuits which take less power than any of our previous designs.

Figure 3.3 shows is an oscilloscope trace shown the fully working new low power microstimulator circuitry. The stimulating output shown in Figure 3.3 has been set to 8 mA (this is done by laser trimming). It is shown sending a $200\text{ }\mu\text{s}$ stimulation through a $1\text{ k}\Omega$ load. The power requirements of the microstimulator circuitry has successfully been reduced by a factor of $1/3$ from our earlier designs. Microstimulators from our earlier fabrication runs consume a current of about 3 mA . The current consumption of the microstimulators that we fabricated this quarter is 1.6 mA DC during very low frequency stimulation, and about 1.9 mA during 40 Hz stimulation.

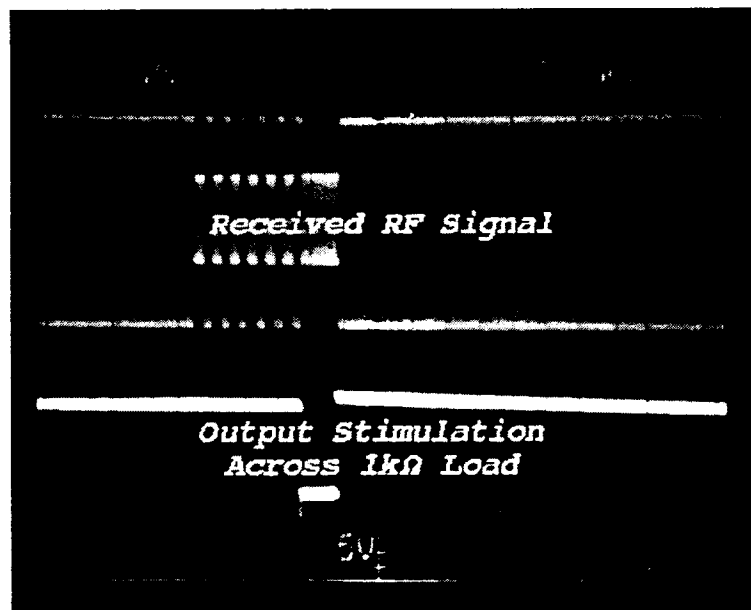


Figure 3.3: The stimulating output of the microstimulator across a $1\text{ k}\Omega$ load. The amplitude of the stimulating output for this device has been set to 8 mA .

3.2 Multichannel Microstimulator With A Bi-Directional Telemetry Link

The single-channel microstimulator discussed above is a major improvement over previous stimulation systems which are orders of magnitude larger. However, for many applications, microstimulator systems will need much more functionality than the single channel microstimulator offers. One of the largest limitations of the single channel microstimulator is that it only has one directional telemetry (data can be sent to the implant; but there is no mechanism for the implant to send data out). Bi-directional telemetry is needed for transmission reliability (data handshaking), for monitoring malfunctions and hermetic packaging integrity, and for sending out data from implanted sensors. Other limitations of the single channel device include the limited extent of user programmability (the stimulating output pulse is a fixed amplitude, not user programmable), and the fact that it has only one stimulation channel. The multichannel microstimulator has been developed to address the limitations of the single channel device. It has an active on-chip transmitter and an integrated transmission coil giving it bi-directional telemetry capability. The multichannel device also has greater user programmability

(the stimulating pulse amplitude as well as the pulse duration can be programmed), and it can support up to 8 stimulating electrodes.

Figure 3.4 shows the overall structure of the multichannel microstimulator. It consists of six discrete elements: a micromachined silicon substrate; a silicon IC chip; a hybrid capacitor used for charge storage of the stimulation pulse; a hybrid receiver coil for power and data reception; an electroplated transmitter coil; and a custom machined glass capsule. The silicon substrate contains one return electrode and up to 8 stimulating electrodes. The IC chip is used for data reception, transmission, and microstimulator control and is affixed atop the silicon substrate. The hybrid capacitor and receiver coil are mounted on the IC chip, while the electroplated transmitter coil is IC compatible and is fabricated on-chip at the end of the BiCMOS process. Lastly, a hermetic package is formed by the glass-silicon bonding technique discussed before. Figure 3.5 shows a photograph of the multichannel microstimulator without the hermetic packaging or the stimulating electrodes.

3.2.1 Overall System Architecture

Table 14 lists the specifications for the multichannel microstimulator. This second generation multichannel microstimulator receives power and data through wireless RF telemetry and incorporates voltage regulators, clock recovery, data detection, output drivers, and an active on-chip transmitter onto a single BiCMOS IC chip measuring 1.4mmx13.5mm. The system nominally dissipates about 20mW of power, and it can deliver programmable amplitude (1-10mA) and duration (1-256 μ sec) current pulses into tissue through eight on-chip electrodes. An on chip transmitter and integrated coil allow data transmission out of the body on an AM modulated 30 MHz RF carrier. In the multichannel microstimulator the on-chip transmitter is used for echoing received data. This not only allows the system to detect erroneous data and to retransmit the same data, but it also lets the external control system know whether or not the implant is powered up and functioning properly. With the addition of a sensor and digitizing circuitry, the on-chip transmitter can eventually be used for closed loop control of muscle. Figure 3.6 shows a system block diagram for the multichannel microstimulator which illustrates the forward and reverse telemetry links.

The strength of the externally applied telemetry signal is orders of magnitude larger than the strength of the signal from the on-chip transmitter because the externally applied signal must be strong enough to inductively power the implant. For this reason, steps had to be taken to insure that the externally applied high power signal would not overwhelm the relatively weak on-chip transmitter signal. One seeming simple solution is to shut off the externally applied telemetry signal during on-chip transmitter operation, but that would require additional components such as high energy capacitors to power the on-chip transmitter during the time that the inductive powering link is shut off. Instead, two other design techniques insure that the on-chip transmitter signal can be correctly received externally. First, the signal from the on-chip transmitter is over order of magnitude higher in frequency than the externally applied powering signal. This allows the high energy powering signal to be filtered out with minimal loss to the on-chip transmitter signal. Second, as shown in Figure 3.6, the on-chip transmitter coil is physically perpendicular to the power transmission/reception coils. This reduces the amount of energy coupled from the forward telemetry system to the reverse telemetry system.

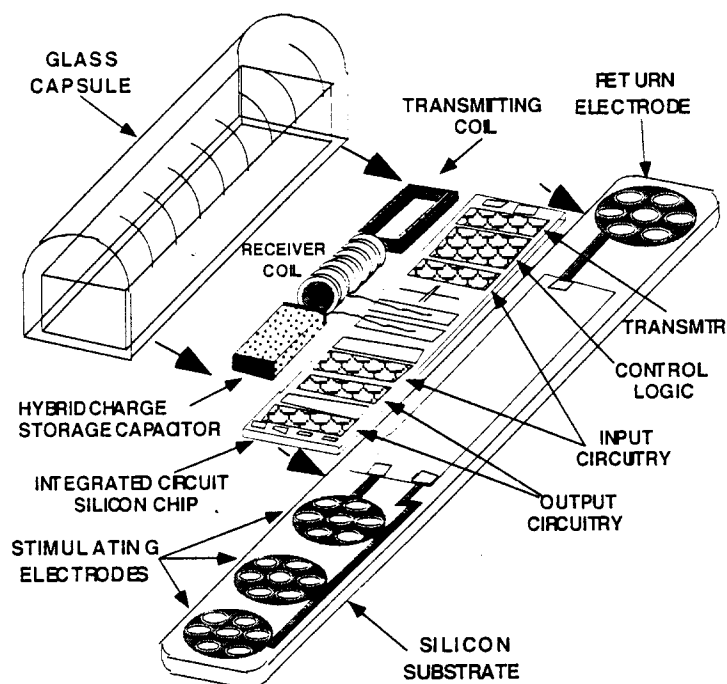


Figure 3.4: Exploded view of the multichannel microstimulator

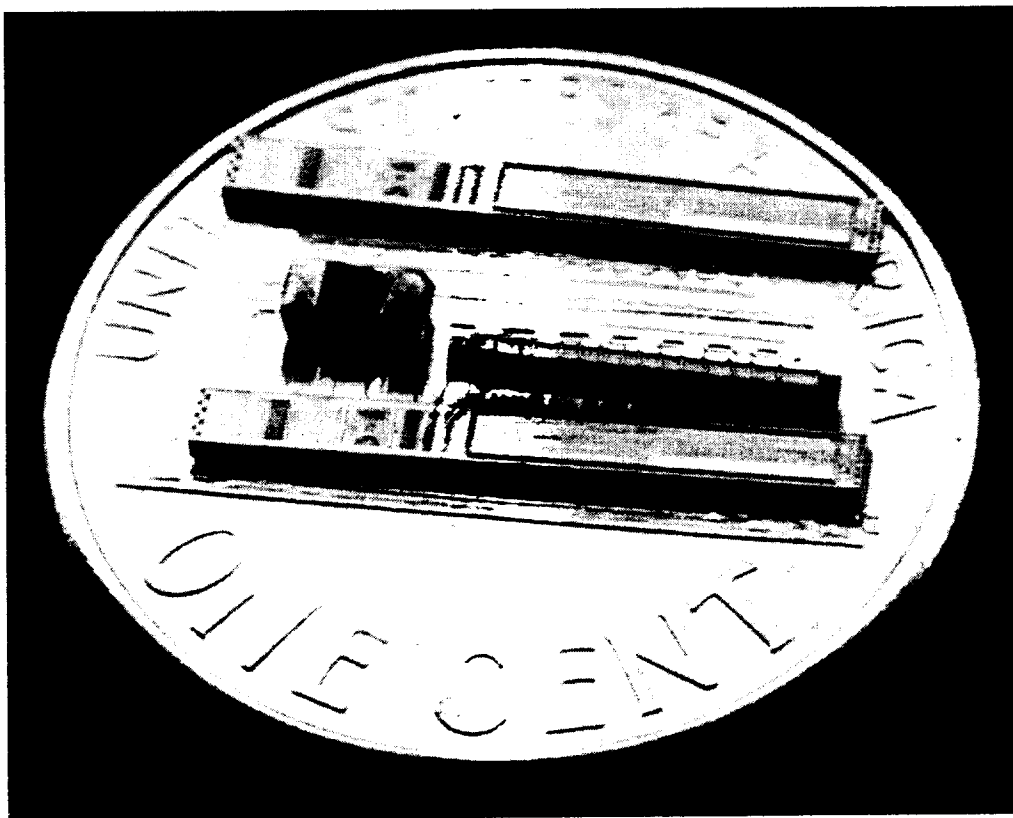


Figure 3.5: Photograph of the multichannel microstimulator without the electrodes or the hermetic packaging. Shown is the IC chip, the discrete charge storage capacitor, the power reception coil, and the on-chip transmission coil.

Table 14: Specifications for a telemetry powered multichannel stimulator.

General	
Dimensions = 2.0mm X 2.0mm X 10 mm	Power Delivery = Telemetry
Power Consumption < 20 mW	On Chip Supply = 4V, 8V, and Gnd
Forward Telemetry	
Carrier Frequency = 1.8 MHz	Modulation = ASK, 20 k-BPS
Implanted Receiver Coil = 1.8 mm diameter	Discrete solenoid
Reverse Telemetry	
Carrier Frequency = 30 MHz	Modulation = On/Off Modulation
Implanted Transmitter Coil = Integrated on-chip coil	
Stimulating Output	
Output Channels = 8	Amplitude = 0 to 10 mA (1.42 mA steps)
Duration = 0 to 256 μ S (1 μ S steps)	Output Load < 800 Ω

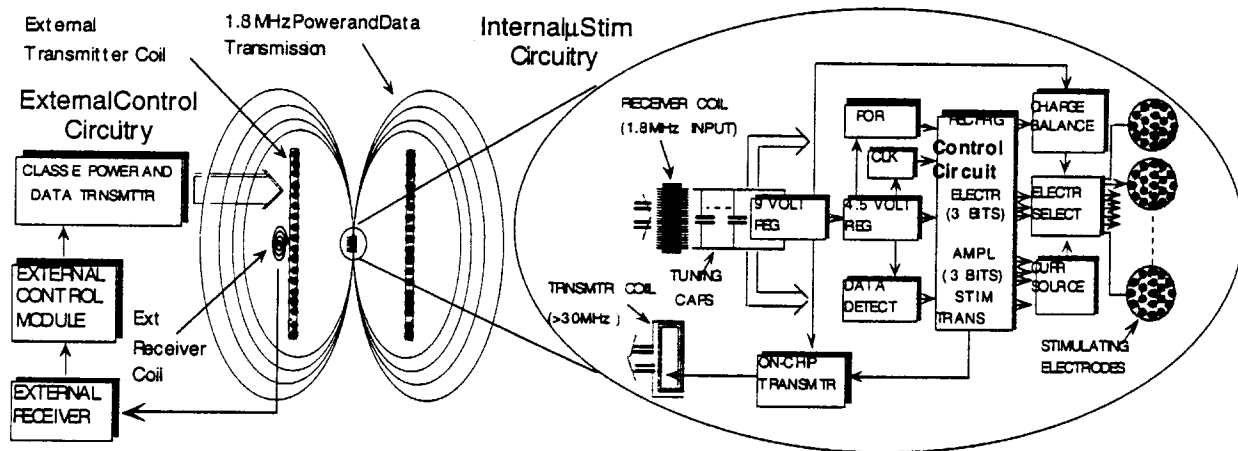


Figure 3.6: Overall system block diagram for the multichannel microstimulator

Figure 3.7 shows the data transmission protocol for the multichannel microstimulator. At the start of data transmission the external transmitter sends a start up signal to indicate that data transmission is about to begin. Since multiple devices may be implanted in the same general area, the first data to be sent is the address of the microstimulator that is being programmed, along with a parity bit. If the received address matches the address that is hard wired in a given microstimulator, it will respond by transmitting back the data it just received. All other microstimulators will stand by until the next start up signal is received. Once the external circuitry receives the transmission from the selected microstimulator, it can send either a continue or a reset signal. If a continue is transmitted, then the next data word, along with a parity bit, is sent. The information in subsequent data words includes the function to be performed, the stimulation pulse duration and amplitude, the selection of the stimulating electrodes, etc. After each word of additional information is sent, the on-chip transmitter is used to send back the information that was just received by the device. This ensures that any errors in

transmission are detected. After each word of data, the external controller can either allow the device to continue or force it to reset. If the device is allowed to continue, it will perform the proper stimulation or circuit/package self-test and then automatically reset. A maximum of 24 bits of data need to be sent to program the device to stimulate.

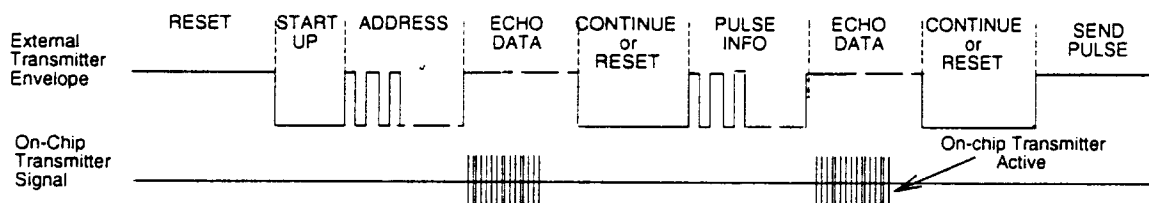


Figure 3.7: Data transmission protocol for the multichannel microstimulator

3.2.2 Bi-directional Telemetry Link

One of the most important features of this device is the active on-chip transmitter, as it allows for bi-directional communication and a much more fault-tolerant system. The on-chip transmitter consists of a coil and active driver similar to the external power/data transmitter. Figure 3.8 shows the schematic for the on-chip active transmitter. It consists of an inductor L_t for RF-telemetry of data to the outside world, capacitor C_t for tuning the LC resonance of the transmitter coil, tuning capacitor C_{set} for frequency setting of the self-oscillating NAND-inverter-inverter loop, an NMOS drive transistor for driving the inductor, and a transmit signal to the NAND that turns the oscillator on and off. All of the elements of this transmitter are integrated on chip, without the use of hybrid components which would consume a large volume and require large bonding pads to connect them to the circuit. The most critical element of this design is the transmitter coil. We have developed a fabrication process that allows to construct a high quality coil that can function with low losses at $\geq 20\text{MHz}$. This process consists of depositing an electroplating base on a wafer, then forming a thick photoresist mold, followed by electroplating copper (chosen for its low resistivity) using the photoresist mold.

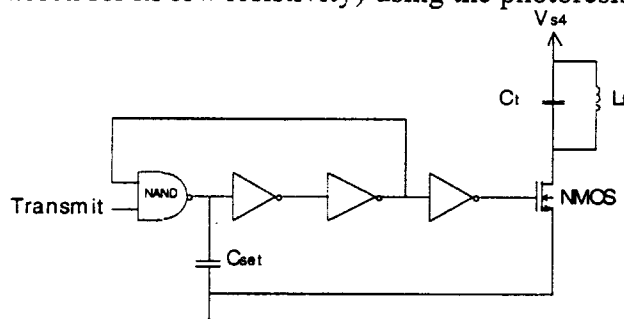


Figure 3.8: On-chip transmitter circuit design.

Figure 3.5 also shows the on-chip electroplated copper coil used for data transmission. It is a $12\mu\text{m}$ thick, 10 turn rectangular coil with average dimensions of 1.24mm by 7.42mm , a measured inductance of $1.2\mu\text{H}$, a series resistance of 36Ω , and a self resonance of $>40\text{MHz}$. The transmitter operates at a nominal frequency of 33MHz , but can be tuned to a range of between 20MHz and 60MHz . The transmitter has been operated with this coil, and Figure 3.9 shows an unbuffered and unfiltered 33MHz AM voltage received with an external coil >2 feet away from the transmitter coil.

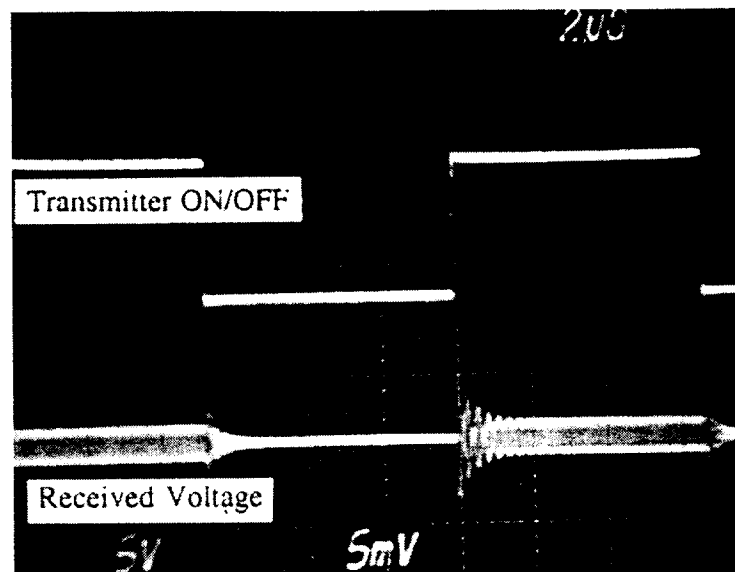


Figure 3.9: Photograph showing the functioning reverse telemetry link. The top trace shows the signal turning on and off the on-chip transmitter, and the bottom trace shows the reverse telemetry signal received by an antenna 2 feet away from the on-chip transmitter.

The multichannel microstimulator has been fabricated and is fully functional. Figure 3.10 shows a scope trace of the proper stimulating output of the system while under full telemetric operation. This first version of the multichannel microstimulator circuitry requires a high intensity field to power it, and as a result a 9-volt battery powered class-E transmitter can only power the system with a 6-cm diameter transmitter coil. Currently we are working on reducing the power consumption of the device so that they can be powered by a transmitter coil 9 cm diameter.

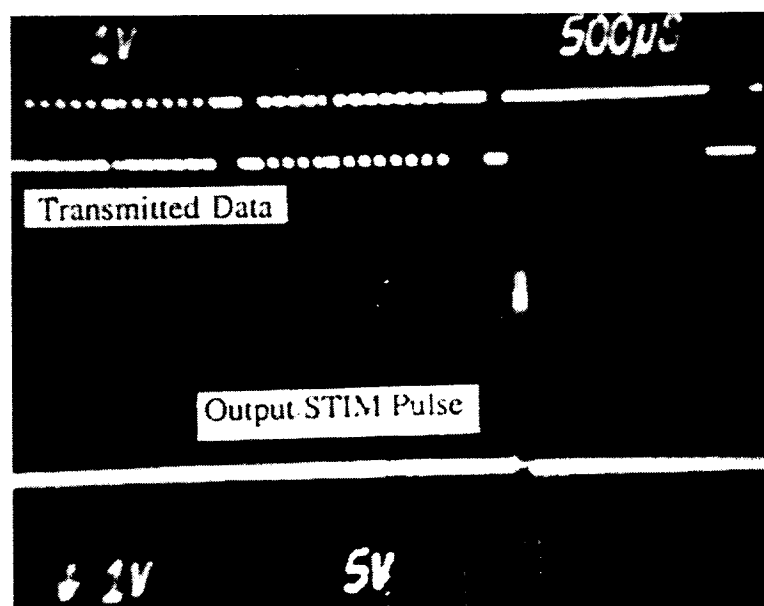


Figure 3.10: Oscilloscope trace showing the digital address sent to the multichannel microstimulator (top trace), and the output current pulse delivered to the programmed channel (lower trace).

3.3 FINESS System Overview

An inductively powered peripheral nerve stimulation system which is fully integrated on a single chip has been developed under this contract in order to demonstrate the small size of the systems that can be achieved using chip scale hermetic packaging techniques. The system is called FINESS (An acronym for Fully Integrated Nerve Electrical Stimulation System). FINESS is the smallest wireless implantable FNS system known. It is about an order of magnitude smaller than the microstimulator, as illustrated in Figure 3.11. This remarkably small size was achieved by eliminating discrete hybrid components altogether. By far the largest components in the microstimulator are the charge storage capacitor and the discrete receiver coil. These two components take up about 90% of the total microstimulator volume. As shown in Fig. 3.11, the volume of FINESS was minimized by integrating the receiver coil directly on the CMOS substrate and by not using a charge storage capacitor. The result is an inductively powered stimulator which is fully integrated on a single chip with no discrete components. While the microstimulator is about 2.5 mm thick and has a volume of about 50 mm³, the hermetically packaged FINESS chip can be as thin as 300 μ m with a volume of about 6 mm³ (provided that the FINESS chip is sufficiently thinned).

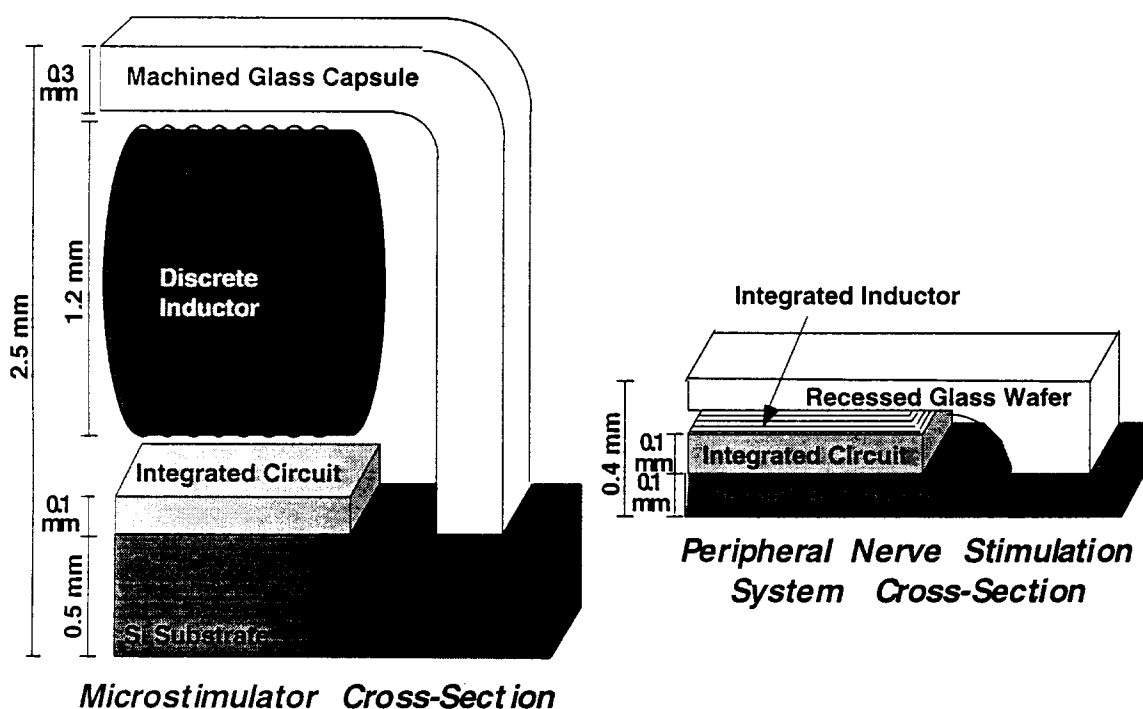


Figure 3.11: A scale drawing comparing the volume of the peripheral nerve stimulation system with the volume of the microstimulator.

The FINESS chip is designed specifically for peripheral nerve stimulation because of the relatively low current level requirements. Typical peripheral nerve stimulation levels of 100 μ A to 3 mA are a good fit with the 3 mA output that is feasible using on-chip coils and no charge storage capacitor (for comparison the microstimulator stimulates with an output of 10 mA or more). A complete FNS system using the FINESS chip is illustrated in Fig. 3.12. In this system the FINESS chip is embedded in a silicone encapsulated stimulating electrode array containing up to 8 pairs of electrodes. The result is a totally leadless peripheral nerve stimulation system which is not much larger than the target peripheral nerves. A transmitter and transmitter coil located outside of the body provide both power and control signals to the implanted system through an inductive link. The transmitter is portable, and a 9 volt battery powered version is capable of powering a FINESS chip implanted up to 3 cm deep into tissue.

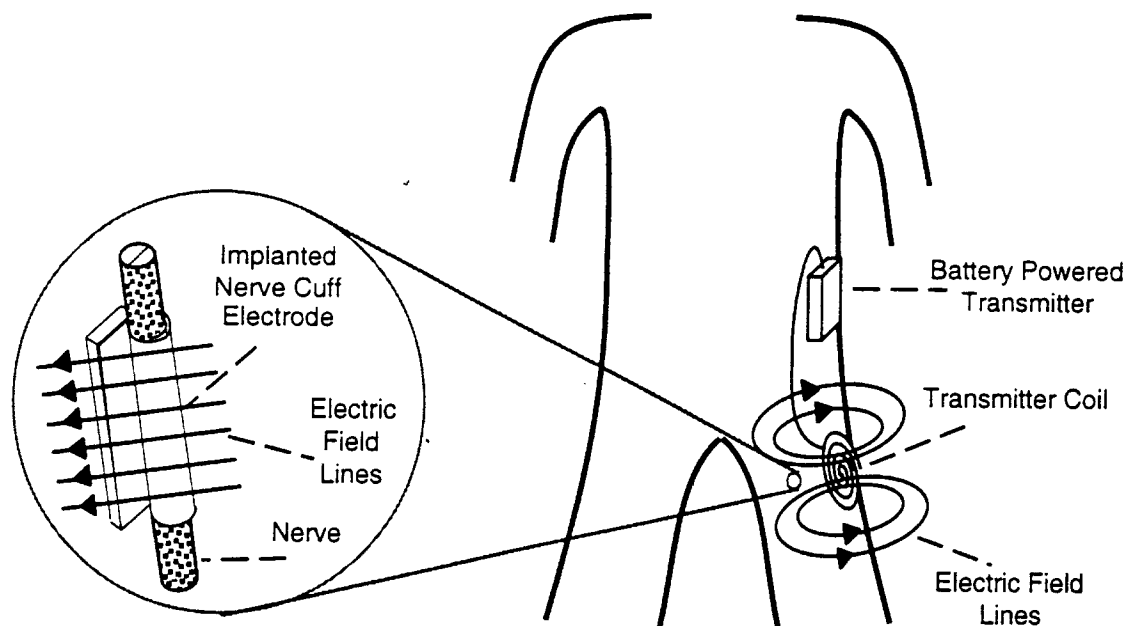


Figure 3.12: Illustration of a complete cuff electrode system.

A block diagram for the Bi-CMOS FINES chip is shown in Figure 3.13. The chip contains a full analog RF receiver front end (including an integrated receiver coil, tuning circuit, power regulation, clock recovery, and data detection circuitry) a digital control block (which includes data registers, error detection circuitry, and a finite state machine), and analog output circuitry (including the programmable stimulating current source and de-multiplexers for selecting electrodes). The integrated RF receiver coil is fully CMOS compatible, and consists of electroplated copper windings with an electroplated nickel-iron core. Table 15 gives the specifications for the FINES chip. The system has a one directional telemetry link through which it generates power and receives data. The system can support up to 8 sets of stimulating electrodes and is capable of supplying a current amplitude of up to 2 mA for a duration of up to 2 ms through loads of up to 1.5 k Ω . Due to power constraints, simultaneous stimulation of more than one set of electrodes is not possible. The stimulating current output is a bi-phasic pair of square pulses as shown in Figure 3.14. The delay between the phases of the output are programmable, and each phase has an independently programmable duration (10 bit resolution) and amplitude (5 bit resolution). Forty bits of data (and five parity bits) are required to be sent telemetrically in order to program the FINES chip for each stimulation.

The FINES chip can be connected to a great variety of peripheral nerve stimulating electrodes such as sieve electrodes or hook electrodes, but the system was specifically designed to be incorporated into nerve cuffs. Figure 3.15 illustrates how FINES might be incorporated into a nerve cuff. In this figure, the FINES chip is electrically connected to any one of a variety of available nerve cuffs by wire bonds or flip chip techniques. The stimulating chip and interconnects are then encapsulated in silicone rubber to protect them from body fluids. The result is a leadless nerve cuff. Since the FINES chip is about as wide as a typical nerve, and can be thinned to be as slim as a piece of paper, it is designed to be easily incorporated into a nerve cuff without adding significantly to the cuff's size.

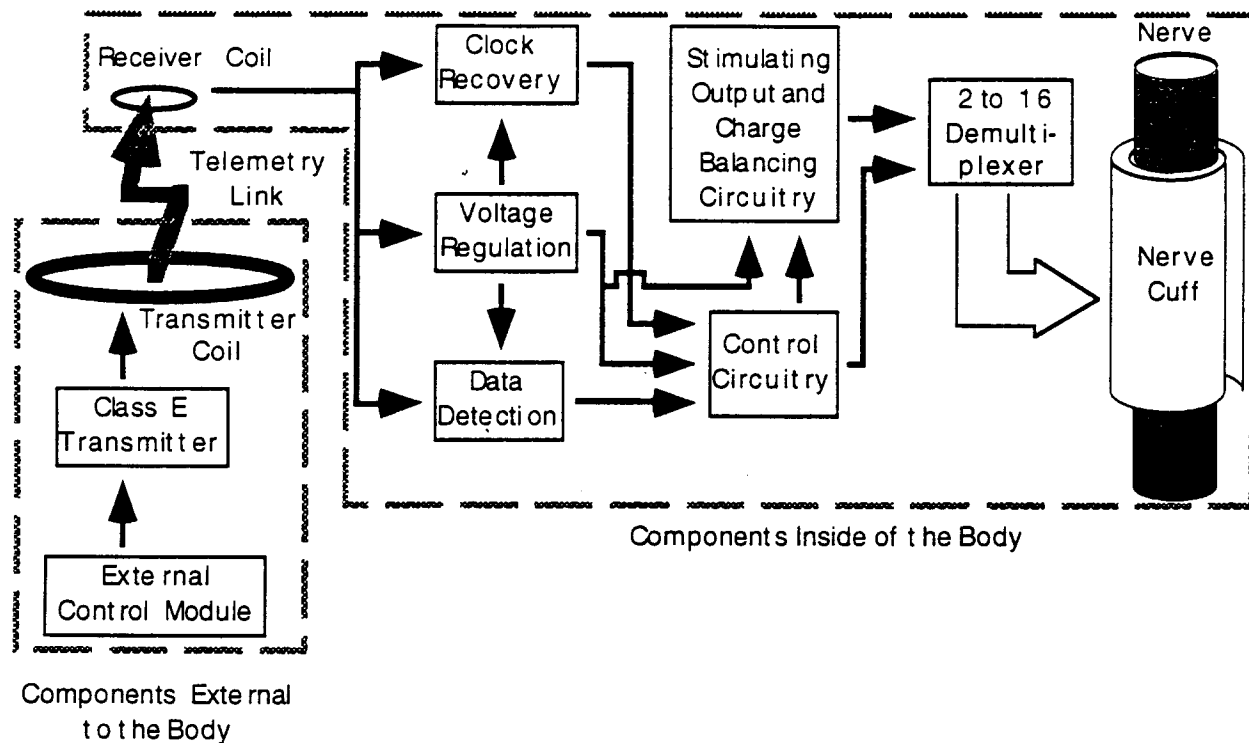


Figure 3.13: A block diagram of the FINES chip.

Table 15: 8-channel peripheral nerve system specifications.

General	
Circuit Area = 2.0 mm X 8.5 mm	Power Delivery = Telemetry
Power Consumption < 15 mW from 4 V supply	On-Chip Regulated Supply = 4 Volts, Gnd
Telemetry Link	
Receiver Coil = On-chip (2.0 mm X 8.0 mm)	Range (coil to coil distance of link) = 3 cm
Transmitter Coil = Planar, air core (80 mm dia.)	Carrier Frequency = 4 MHz
Modulation Frequency = 1 kHz to 50 kHz	Modulation = ASK, Pulse width encoded
Device Addressability = up to 8 individually addressable devices per transmitter	
Stimulation	
Stimulation waveform = Two independent phases of opposite polarity	
Amplitude = 0 to 2 mA (64.5 μ A steps), each phase independently programmable	
Duration (each phase) = 4 to 2050 μ s (2 μ s steps), each phase independently programmable	
Output Channels = 8	Inter-phase delay = 12 to 1932 μ s (16 steps)
Stimulation Frequency \leq 170 Hz	Maximum Output Load = 1.7 K Ω

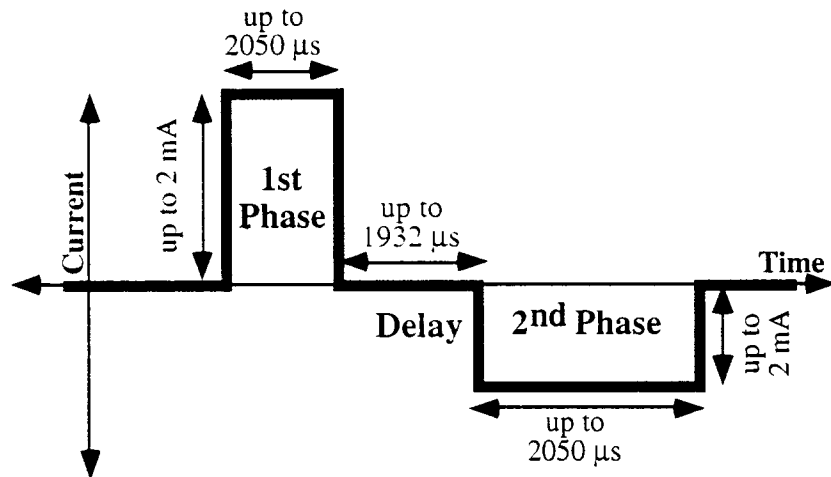


Figure 3.14: The stimulating output of the FINESS chip.

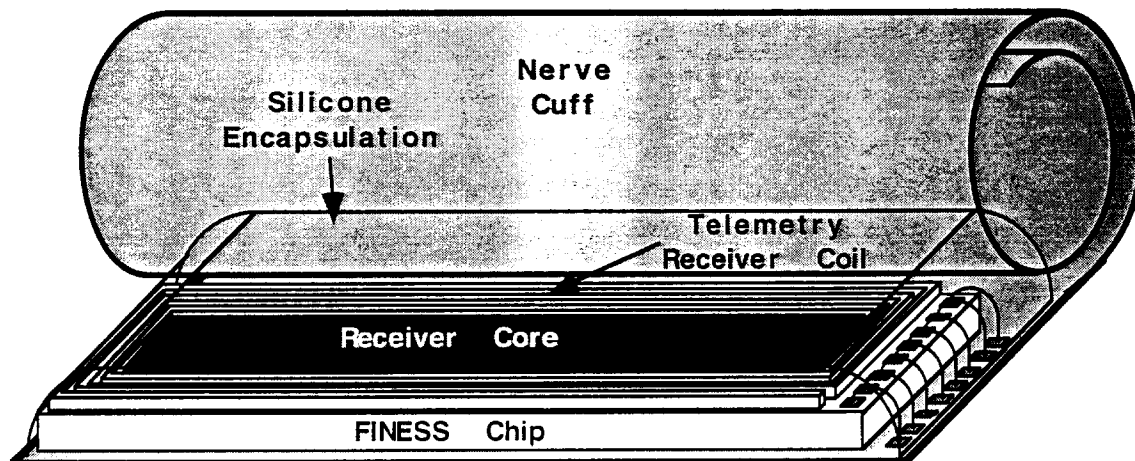


Figure 3.15: Illustration of the FINESS chip in a nerve cuff.

3.3.1 On-Chip Coils For Inductive Powering

The telemetry link used in the FINESS system is illustrated in Fig. 3.16. It consists of two planar, coaxial coils, one of which is a large transmitter coil, while the other is an integrated on-chip receiver coil powering an integrated circuit. To maximize the amount of power delivered to the on-chip coil, the windings are made of electroplated copper, which was chosen because of its low resistivity ($r = 2.0 \times 10^{-6} \Omega\text{-cm}$, which is slightly higher than the resistivity of bulk copper). The core is made out of electroplated NiFe (iron content of 20% by weight), which was chosen because of its high permeability ($\mu_r = 500$ at 4 MHz), and its compatibility with semiconductor processing. Of the many different shapes of receiver coils, a planar spiral receiver coil (shown in Figure 3.17) works best for inductive powering. Although higher inductance can be obtained with solenoid type electroplated coils, a planar coil has a larger cross-sectional area, which maximizes the coupling to the large transmitter coil. The external transmitter coil can either be a planar spiral coil or a short solenoid (short enough to be near planar so that it will not be too bulky when worn on the skin).

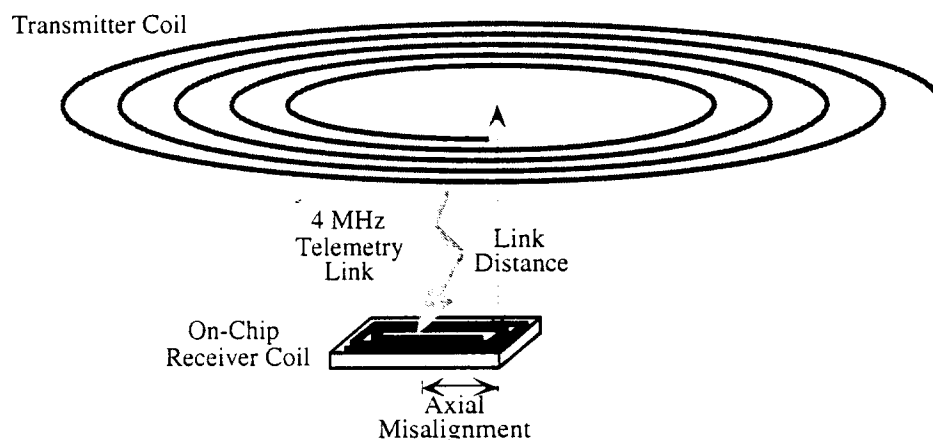


Figure 3.16: A telemetry link using a planar spiral transmitter coil and a planar spiral on-chip receiver coil.

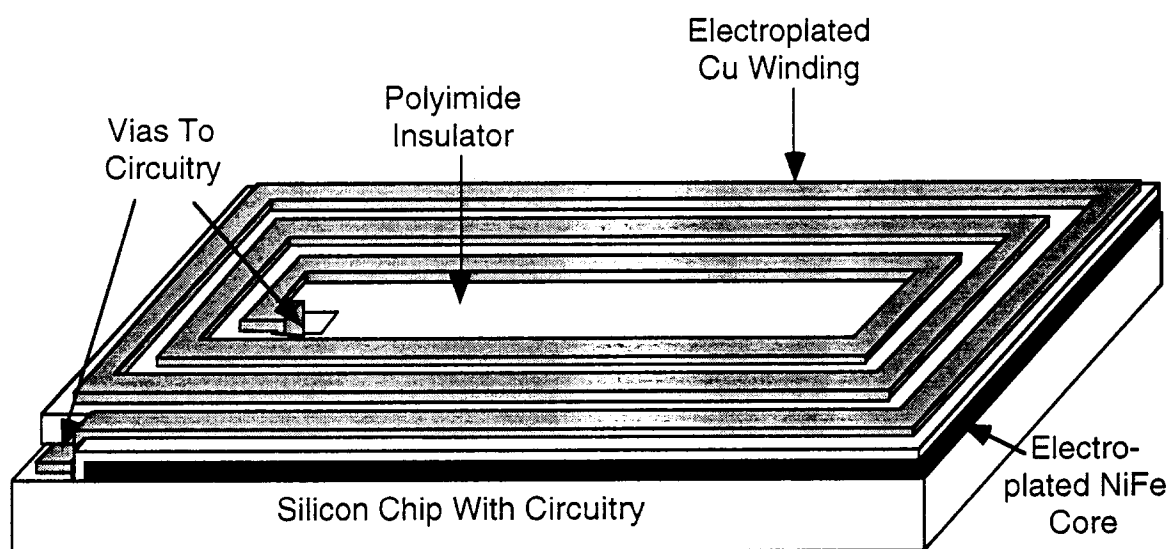


Figure 3.17: An illustration of a 3 turn, planar spiral on-chip coil.

The transmission frequency for this link was chosen to maximize efficiency. For biomedical applications, a transmission frequency of 4 MHz is high enough to provide an adequate Q , but not so high that a significant amount of the RF signal is absorbed by the body. Also, 4 MHz is not so high that degradation of Q due to parasitic substrate capacitance occurs (the self resonance for most of the fabricated coils are over 30 MHz). Finally, screening due to the many conductive layers in the integrated circuit is not a problem at 4 MHz. Conductive layers which can cause screening at higher frequencies include the silicon substrate, the copper electroplating base, and the CMOS metal interconnect layer. Screening can be a problem when the skin depth for one of these conductive layer is comparable to the thickness of that layer. Skin depth is given by equation 1, where σ is the conductivity, ω is the angular transmission frequency, and μ is the permeability of the conductive layer. Table 16 gives the skin depth at 4 MHz for the various conductive layers in the on-chip coils as well as the actual thickness of the various layers. As can be seen, the actual thickness of these layers is almost 2 orders of magnitude less than the skin depth, so screening effects are negligible at 4 MHz.

$$\delta = \sqrt{2 / \sigma \omega \mu}$$

Equation 1

Table 16: The thickness of various FINESS chip conductive layers compared with the skin depth at 4 MHz.

Material	Conductivity	4 MHz Skin Depth	Thickness in FINESS Chip
Silicon Substrate	$0.1 \Omega^{-1} \text{cm}^{-1}$	79.6 mm	0.5 mm
Copper Plating Base Under core	$5.8 \times 10^5 \Omega^{-1} \text{cm}^{-1}$	33 μm	0.2 μm
Aluminum Interconnect Layer	$3.54 \times 10^5 \Omega^{-1} \text{cm}^{-1}$	42 μm	0.8 μm

3.3.2 Modeling the Telemetry Link

In general, an implantable microsystem inductively powered through an on-chip receiver coil has a very weakly coupled inductive link (The FINESS chip has a coupling coefficient of about 0.005). In order to successfully power such systems, all of the design parameters of the link must be optimized for receiving power. Therefore the relationship between these design parameters and the received power must be well understood. Some of the design parameters that affect the efficiency of the link include the number of turns of both the transmitter and receiver coil, the shape and dimensions of both of the coils, the transmission frequency, the distance separating the two coils, and the line width and thickness of the electroplated receiver coil turns. An analytical model of the telemetry link was developed which relates the power received by the implanted circuitry to all of the basic physical dimensions and design parameters of the system. The model was used to calculate the power received for a wide range of receiver coils, transmitter coils, transmission frequencies and circuit loads. By analyzing the effect of each design parameter on received power, the FINESS telemetry links was optimized.

One of the key sets of equations from the analytical model gives the inductance of the rectangular, planar, spiral, electroplated, receiver coil. The inductance (L_r) can be approximated by equations 2 through 4. In these equations dimensions are in centimeters, and inductance is in Henrys. n_r is the number of turns, w_r is the width of each turn, L_{coil} and W_{coil} are the average coil winding length and width, h_r is the electroplating height of the windings, and μ_{core} is the effective relative permeability of the core. The relative permeability of electroplated NiFe at 4 MHz is about 500, however, because electroplated core is extremely thin, the *effective* relative permeability is much less. An effective relative permeability of 1.7 was measured for the on-chip coil in the FINESS system. A number of rectangular, planar, electroplated coils have been fabricated and their inductances measured, and it was observed that equations 2 through 4 agree with measurements to within about 5%.

$$k_1 = L_{coil} \cdot \log \left(L_{coil} + \sqrt{L_{coil}^2 + W_{coil}^2} \right) \quad \text{Equation 2}$$

$$k_2 = W_{coil} \cdot \log \left(W_{coil} + \sqrt{L_{coil}^2 + W_{coil}^2} \right) \quad \text{Equation 3}$$

$$L_r = 9.21 \cdot 10^{-9} \cdot n_r^2 \cdot \mu_{core} \left[(L_{coil} + W_{coil}) \cdot \log \left(\frac{8L_{coil}W_{coil}}{n_r w_r + n_r h_r} \right) - k_1 - k_2 \right] \quad \text{Equation 4}$$

A second key equation from the analytical model gives the mutual inductance for the transmitter and receiver pair. Assuming round parallel planar coils which are centered on the same axis, the mutual inductance is given by equation 5. In this equation, d_{link} is the distance separating the transmitter and receiver coils, d_r is the receiver coil diameter, and μ_o is the permeability of free space. This model is valid as long as $d_r \ll d_t$, and $d_r \ll d_{link}$, which is true for the FINESS system. However, FINESS has a rectangular receiver coil (rather than circular) in order to maximize the inductance obtainable in a rectangular space. Also, the two coils in the FINESS system may not be perfectly parallel. Equation 5 can still be used to accurately model the mutual inductance if the receiver diameter (d_r) is calculated to be the diameter of a round coil with an area equivalent to the rectangular coil reflected on the plane of the transmitter. Equation 6 gives the receiver diameter that should be used in equation 5 in terms of the length (L_{coil}) and width (W_{coil}) of the rectangular receiver coil and the angular misalignment of the coils (θ). The results from equation 5 have been compared to graphs giving the mutual inductance of two planar coils as found in the Bureau of Standards Circular 74, and it was found that for the size coils in the FINESS system, the mutual inductance obtained from the two methods agree to within 7%. Although the transmitter and receiver coils may not be centered on the same axis in actual use, the mutual inductance actually increases when these coils are slightly misaligned, and reaches a peak when the center of the smaller coil is aligned to a point on the larger axis about half way from the rim to the center. Because the equations given here assume that the coils are perfectly aligned, they give a slightly lower coupling than can be expected in practice.

$$M = \frac{n_r \cdot n_t \cdot \sqrt{\mu_{core}} \cdot \mu_o \cdot \pi \cdot \left(\frac{d_r}{2}\right)^2 \cdot \left(\frac{d_t}{2}\right)^2}{2 \left(d_{link}^2 + \left(\frac{d_t}{2}\right)^2 \right)^{3/2}} \quad \text{Equation 5}$$

$$d_r \cong 2 \sqrt{\frac{W_{coil} \cdot L_{coil} \cdot \sin(\theta)}{\pi}} \quad \text{Equation 6}$$

3.3.3 Results from On-Chip Coil Models

Figures 3.18 through 3.21 show the received voltage as a function of various link design parameters. These figures show that the FINESS chip is capable of receiving 25 or 30 mW of power at an implant depth of 3 cm, and that larger coils at closer ranges can receive 100's of mW. The FINESS circuitry requires a maximum of 25 mW from the coil to function properly at its highest stimulation output levels, and it requires only about 10 mW at low stimulation amplitudes. Table 17 gives all of the design parameters for the telemetry link that powers the FINESS chip. Figures 3.18 through 21 each show the effect of varying a single design parameter of the link while all of the other parameters are held constant at the values given in Table 17. As can be seen, the coil parameters given in Table 17 are near optimal for the FINESS chip at 3 cm link distance. Also, it should be noted that measured results from the FINESS chip are in good agreement with the graphs in this section.

Table 17: The FINESS system telemetry parameters used calculations to generate Figures 3.18 through 3.21.

Frequency of link	4 MHz	On-chip receiver coil length	10 mm
Link distance (between transmitter and receiver coils)	3 cm	On-chip receiver coil width	2 mm
Arrangement of transmitter and receiver coils	Coplanar & coaxial	Line width of receiver coil windings	40 μm
Diameter of transmitter coil	8 cm	Spacing between receiver coil windings	10 μm
Transmitter coil number of turns	20	On-chip receiver coil number of turns	17
Transmitter coil geometry	Short Solenoid	On-chip receiver coil geometry	Planar Spiral
Transmitter coil core	air core	Effective relative permeability of 10 μm NiFe core	1.7
Transmitter power supply	9 V battery	Electroplating thickness of receiver coil Cu windings	10 μm
Transmitter coil Q setting series resistance	7 Ω	Implanted circuitry equivalent load	2.5 k Ω

Figure 3.18 shows the received power as a function of the distance separating the transmitter and receiver coil. The shorter the link distance the more power is transferred. Figure 3.18 shows that the 25 mW maximum required by the FINESS chip can be transmitted over link distances of about 3 cm with these coils.

Figure 3.19 shows the received power as a function of the diameter of the transmitter coil. If the transmitter coil is too small, the transmitted field from the coil doesn't penetrate very deeply into tissue and very little power is received. On the other hand, if the transmitter coil is too large, the size mismatch between the transmitter and receiver coils results in very low coupling, and very little power is received. Figure 3.19 shows that clearly the optimum diameter for the transmitter coil is about 8 cm for the FINESS system.

The received power as a function of the load resistance is shown in Figure 3.20. At load resistances below about 1 k Ω , the load dominates the Q of the receiver system, and as a result there is a sharp decrease in received power as the load is decreased. At load resistances higher than about 1 k Ω , the series resistance of the coil windings dominates the Q of the receiver system, and as a result the received power remains relatively constant and independent of the load. The FINESS circuitry is equivalent to about a 2.5 k Ω load during maximum stimulation, and a 7 k Ω load when not stimulating. Since the FINESS chip requires the most power during maximum stimulation, the telemetry link has been optimized to provide maximum power at load levels of about 2.5 k Ω .

The received power as a function of the angular misalignment of the coupled coils is shown in Figure 3.21. Ideally the receiver coil should be parallel to the transmitter coil, but in practice the coils will not be perfectly aligned, and implant migration and movement may cause the angular alignment to change with time. The figure shows that slight angular misalignment of the coils can be easily tolerated, but severe angular misalignment will result in a significant reduction in the received power.

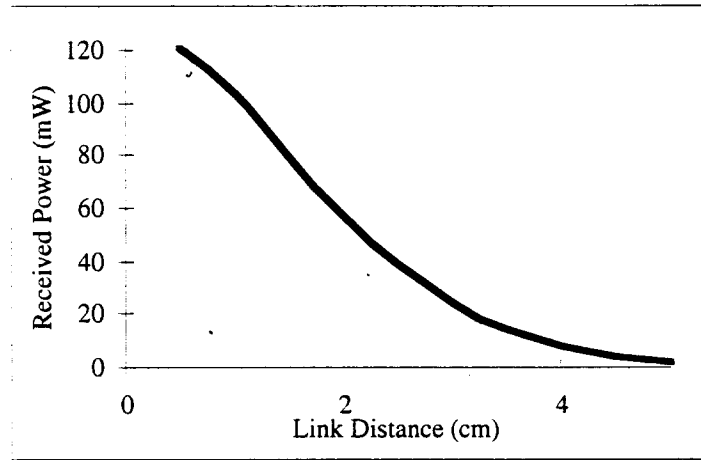


Figure 3.18: The DC received power as a function of link distance.

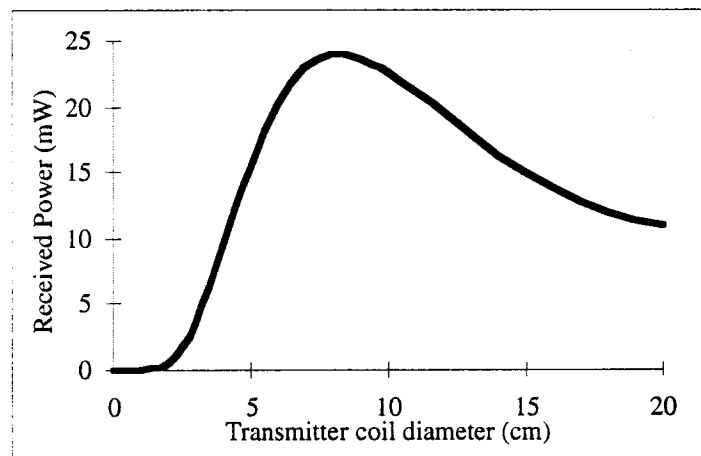


Figure 3.19: The DC received power as a function of the transmitter coil diameter.

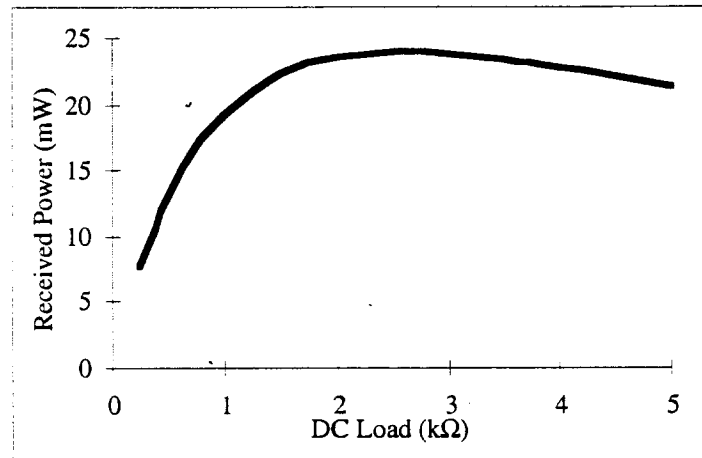


Figure 3.20: The DC received power as a function of load resistance.

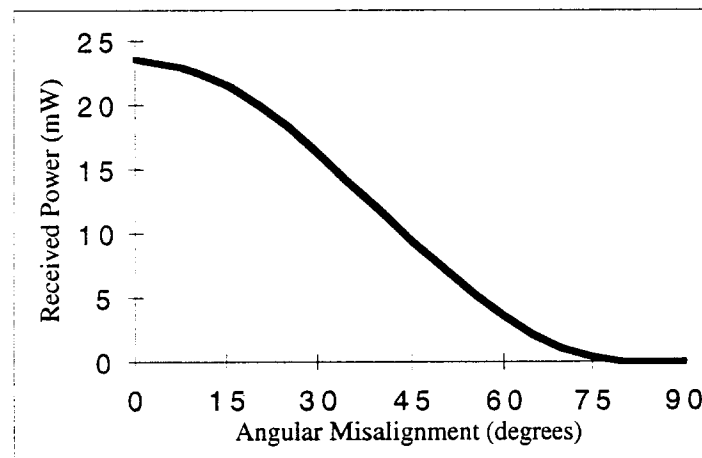


Figure 3.21: The DC received power as a function of the angular misalignment of the coupled coils.

3.3.4 Fabrication and Testing of On-chip Coils

This section reports on fabrication techniques and test results from the on-chip coils that were developed for the FINESS system. Figure 3.22 shows a photograph of two of the fabricated coils. This section begins by reporting on six different on-chip coil structures which were fabricated and tested. Although all of the coil structures are planar spiral, they differ in fabrication complexity and final coil quality. The fabrication sequence for the most complicated (and best performing) coil structure is then described. Finally measured results are given, showing how much power these coils receive in an inductively coupled link. The measured power received by these coils under a variety of conditions deviate less than 20% from the values predicted by the analytical model.

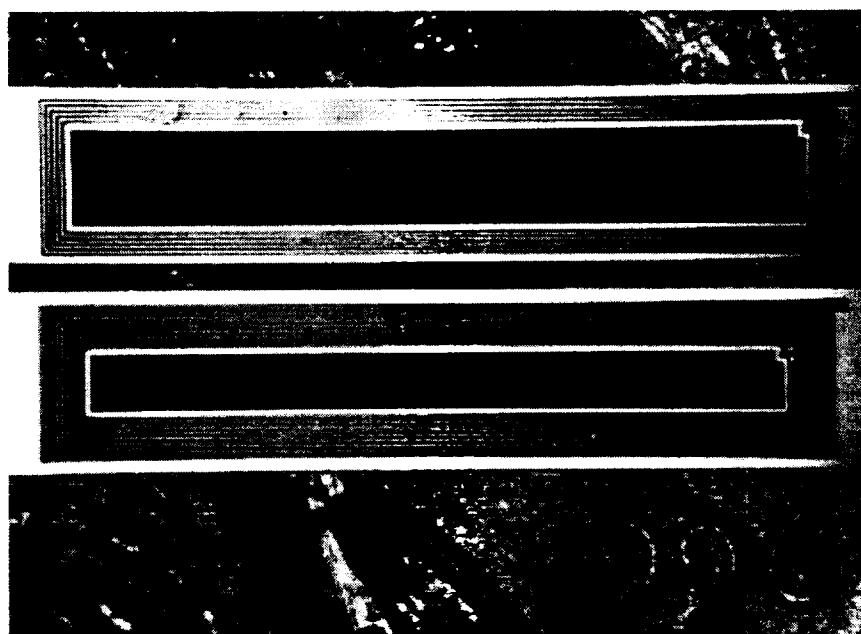


Figure 3.22: Photograph of a 5 and 10-turn Cu on-chip coil with NiFe core on a US penny. These coils are 2 by 10mm.

The six different on-chip coil structures, shown in Figure 3.23, were fabricated, tested, and compared. Table 18 summarizes measurements from 5-turn, 10-turn, 17-turn and 19-turn versions of these coil structures. Inductances of over $2.0 \mu\text{H}$ and quality factors around 6 were obtained at 4 MHz from the 10 turn versions of the best of these coil designs.

Design A is an air-core coil. Coils of this design were fabricated as a control against which all of the coils with cores could be compared. The air core coils together with a receiver and a voltage regulator, are able to deliver about 15mW of DC power to a $2.5 \text{ k}\Omega$ load when excited by a 4 MHz signal at a link distance of about 1 cm. Because the air core coils are the simplest coils to fabricate, they may be useful for lower power or shorter range applications, however, they are not the best choice for powering systems requiring 10's of mW of power at larger link distances, such as the FINESS system.

Design B is a coil with a NiFe core confined to the center of the windings. This coil did not perform significantly better than the air-core coil, primarily because of the small area in the center of the windings available for the core and because these samples had a thin NiFe

electroplating thickness. As can be seen in Figure 3.24, the NiFe on this batch of coils was only a few μm thick. These coils were only fabricated in 5 and 10 turn versions.

Design C, which uses NiFe for both the windings and core, had the highest inductance of any of these coils. However, the high resistance of the NiFe windings makes this a very inefficient receiver.

Design D is the best performing design that did not use a hybrid attached commercial core (the best performing fully integrated design). In this design, the NiFe core is located underneath the windings, separated by an insulating polyimide layer. Although this stacked structure makes these coils more complicated to fabricate than coils of Design B, it has the advantage of allowing the core to be the full size of the chip, rather than being confined to the center of the windings. A cross-sectional SEM photograph of a coil with this structure is shown in Figure 3.25. This design is the most complex to fabricate because both the core and the polyimide need to be patterned to allow the copper windings to contact the circuitry beneath it. Ten turn versions of these coils with approximately $25\ \mu\text{m}$ thick cores have inductances more than twice as high as identical coils with air core, although the yield on these coils is low due to material stresses. Five, seventeen and nineteen turn versions of this coil were fabricated with cores approximately $8\ \mu\text{m}$ to $10\ \mu\text{m}$ thick, and these coils had a high yield (due to the thinner core) and inductances approximately 75% higher than their air core counterparts. Note that the relatively thick polyimide layer in these coils (about $3\ \mu\text{m}$) helps to reduce parasitic substrate capacitance.

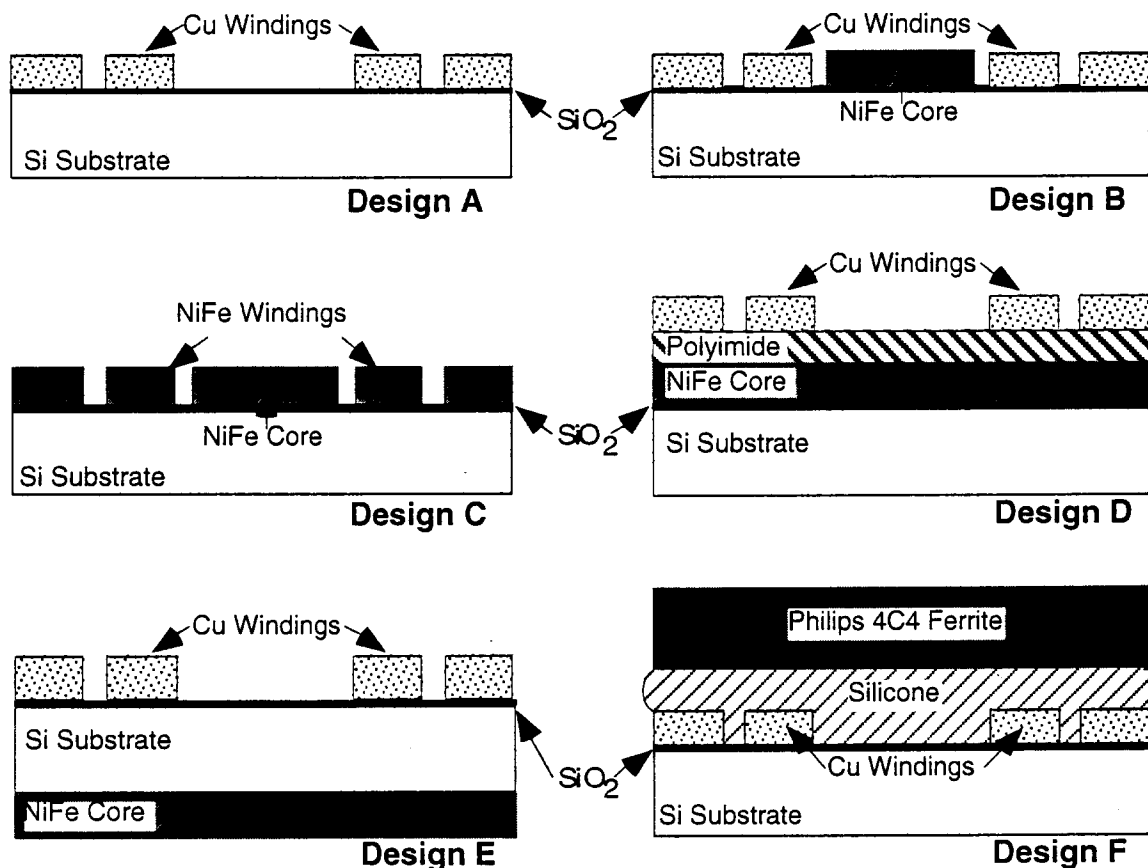


Figure 3.23: Cross sections of six different coil structures which were fabricated and tested.

Table 18: Measurements from the six coil designs shown in Figure 3.22. Data is given for 5, 10, 17, and 19 turn coils. These coils are all 2 by 10mm with 10 μm thick copper windings.

Five turn coils

Design From Error! Reference source not found.	Design A	Design B	Design C	Design D	Design E	Design F
Inductance (4 MHz)	0.35 μH	0.4 μH	3.0 μH	0.5 μH	-	-
Resistance	5 Ω	5 Ω	75 Ω	5 Ω	-	-
Q (4MHz)	1.8	2.0	1.0	2.5	-	-
Self resonance	> 40 MHz	> 40 MHz	-	> 40 MHz	-	-
Core thickness	-	3 μm	10 μm	10 μm	-	-

Ten turn coils

Design From Error! Reference source not found.	Design A	Design B	Design C	Design D	Design E	Design F
Inductance (4 MHz)	0.95 μH	1.0 μH	9.0 μH	2.4 μH	1.2 μH	2.6 μH
Resistance	10 Ω	10 Ω	160 Ω	10 Ω	10 Ω	10 Ω
Q (4MHz)	2.4	2.5	1.4	6.0	3.0	6.5
Self resonance	> 40 MHz	> 40 MHz	-	>40 MHz	-	>40 MHz
Core thickness	-	3 μm	10 μm	> 20 μm	25 μm	500 μm

Seventeen turn coils

Design From Error! Reference source not found.	Design A	Design B	Design C	Design D	Design E	Design F
Inductance (4 MHz)	1.76 μH	-	-	2.9 μH	-	-
Resistance	28 Ω	-	-	28 Ω	-	-
Q (4MHz)	1.6	-	-	2.6	-	-
Self resonance	-	-	-	29 MHz	-	-
Core thickness	-	-	-	10 μm	-	-

Nineteen turn coils

Design From Error! Reference source not found.	Design A	Design B	Design C	Design D	Design E	Design F
Inductance (4 MHz)	2.12 μH	-	-	3.8 μH	-	-
Resistance	33 Ω	-	-	33 Ω	-	-
Q (4MHz)	1.6	-	-	2.9	-	-
Self resonance	-	-	-	14 MHz	-	-
Core thickness	-	-	-	10 μm	-	-

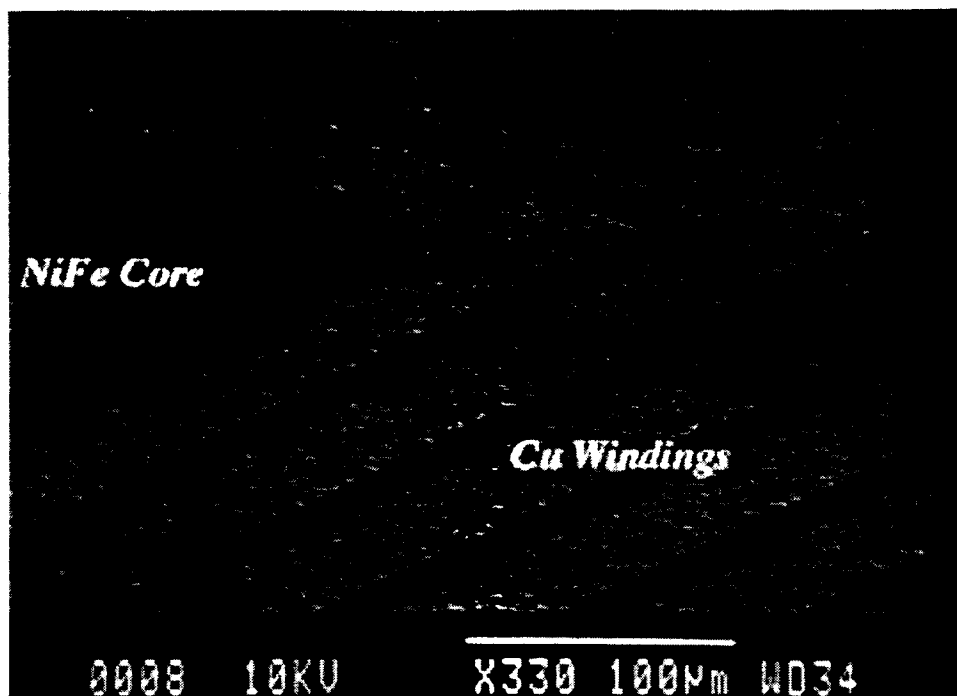


Figure 3.24: SEM photograph of one of the fabricated on-chip coil structures. This coil has a NiFe core in the center of the Cu windings.

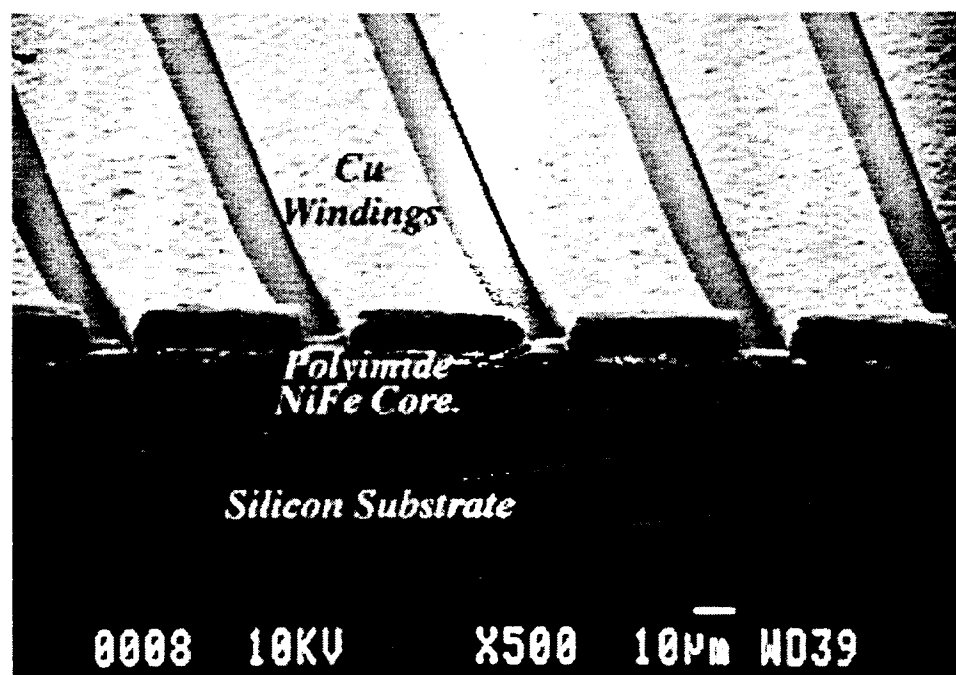


Figure 3.25: SEM photograph of the best performing fully integrated on-chip coil design. This coil has a NiFe core of about 10 μm thickness underneath the Cu windings.

Design E coils have some of the advantage of Design D, but without the added fabrication complexity. These coils have the NiFe core electroplated on the back side of the chip while the copper winding are electroplated on the front. These coils do not perform as well as Design D coils because the NiFe core is on the opposite side of the wafer as the windings. In the samples tested, the core and the windings were separated by the full 500 μm wafer thickness. However, if the wafer had been thinned to 200 or 150 μm before plating the coil on back, these coils would have had better performance. Also, because the core is plated on the back, these wafers can have a much thicker core than any of the other designs. This is because issues such as winding step coverage and compounded thin film stresses do not limit the core thickness of these coils. Since backside plating requires no electroplating mold for patterning, the core of Design E could possibly be plated hundreds of microns thick fairly easily (although shielding of the RF signal by the core may be a concern at this thickness).

Finally, Design F was fabricated for comparison. These coils are not fully integrated because they have a 500 μm thick commercial ferrite core ($\mu_{\text{rel}}=125$ at 4 MHz) attached to them. The commercial ferrite cores can be attached with either silicone rubber or non-conductive epoxy. As expected, these coils have the highest inductance and Q of all, primarily due to the thickness of the core. However, the inductance and Q are only about 10% higher than the best fully integrated coils of Design D. This small gain may not justify the added expense of a non-batch process for many applications. Also it should be remembered that the commercial core of Design F would double the thickness of the FINES chip.

3.3.5 Fabrication of the On-Chip Coils

The six different coil structures each have a different fabrication sequence. However, the fabrication sequences for all of these structures are similar and involve the same basic steps: deposit a plating base, form an electroplating mold, electroplate copper or NiFe, and finally strip the mold and electroplating base. Because the fabrication steps for each coil are so similar, only the fabrication of the most complex and best performing coil structure (Design D in Figure 3.23) will be described in detail in this section. The fabrication steps for each of the other coil designs can easily be inferred from the fabrication steps for Design D.

The fabrication processes for the on-chip coils of Design D is illustrated in Figure 3.26. It begins with a passivated silicon wafer with the full FINES circuitry on it. An electroplating base of 500 \AA titanium and 2000 \AA copper is sputtered on the wafer. It was found that 2000 \AA of copper is thick enough to provide a uniform electroplating potential across the wafer (no significant resistive loss across the wafer), but not so thick that it will cause significant screening of the RF telemetry signal. An electroplating mold for the NiFe core is then formed using a standard thick photoresist process (a 20 μm thick mold was obtained using AZ 4620). The NiFe mold should be patterned to allow for connections from the copper windings above the core to the circuitry below the core. Also, if desired, core losses due to eddy currents can be minimized by patterning the electroplating mold to break the NiFe core up into small islands (this was not done in any of the coils reported on here).

After the mold is patterned, the NiFe core is electroplated. The highest permeability with low losses and near zero magnetostriction is obtained when the plated alloy is about 80% nickel and 20% iron. As a result this alloy ratio is commonly used in many applications and it is known as *permalloy*. The actual concentration in the plated alloy can be measured by x-ray emission spectroscopy. A ratio of 79.73% Ni and 20.27% Fe was measured for the NiFe used in the on-chip coils reported on here. For best performance, the core should be electroplated as thick as possible. However, if the core is too thick there are three concerns. First stress can cause delamination of the core (this is especially true when the core is buried under polyimide). It was

found that ten micron thick cores adhere well to the substrate, but 25 μm thick cores tend to delaminate. Note that changing the plating conditions, adding stress reducing additives, using a better stress matched insulating layer than polyimide, or segregating the core into many small islands may eliminate this problem. Second, step coverage of the windings over the core may be a problem if the core is too thick. There were not any step coverage problems in the 10 to 20 μm thick cores reported on here, but this may be an issue in thicker cores. Finally, losses due to screening by the core and core eddy currents may be a problem if the core is too thick. There was virtually no core losses in the 10 to 20 μm thick cores reported on here at 4 MHz, however, thicker cores will have core losses. The effect of core losses can be minimized by segregating the core into many small islands.

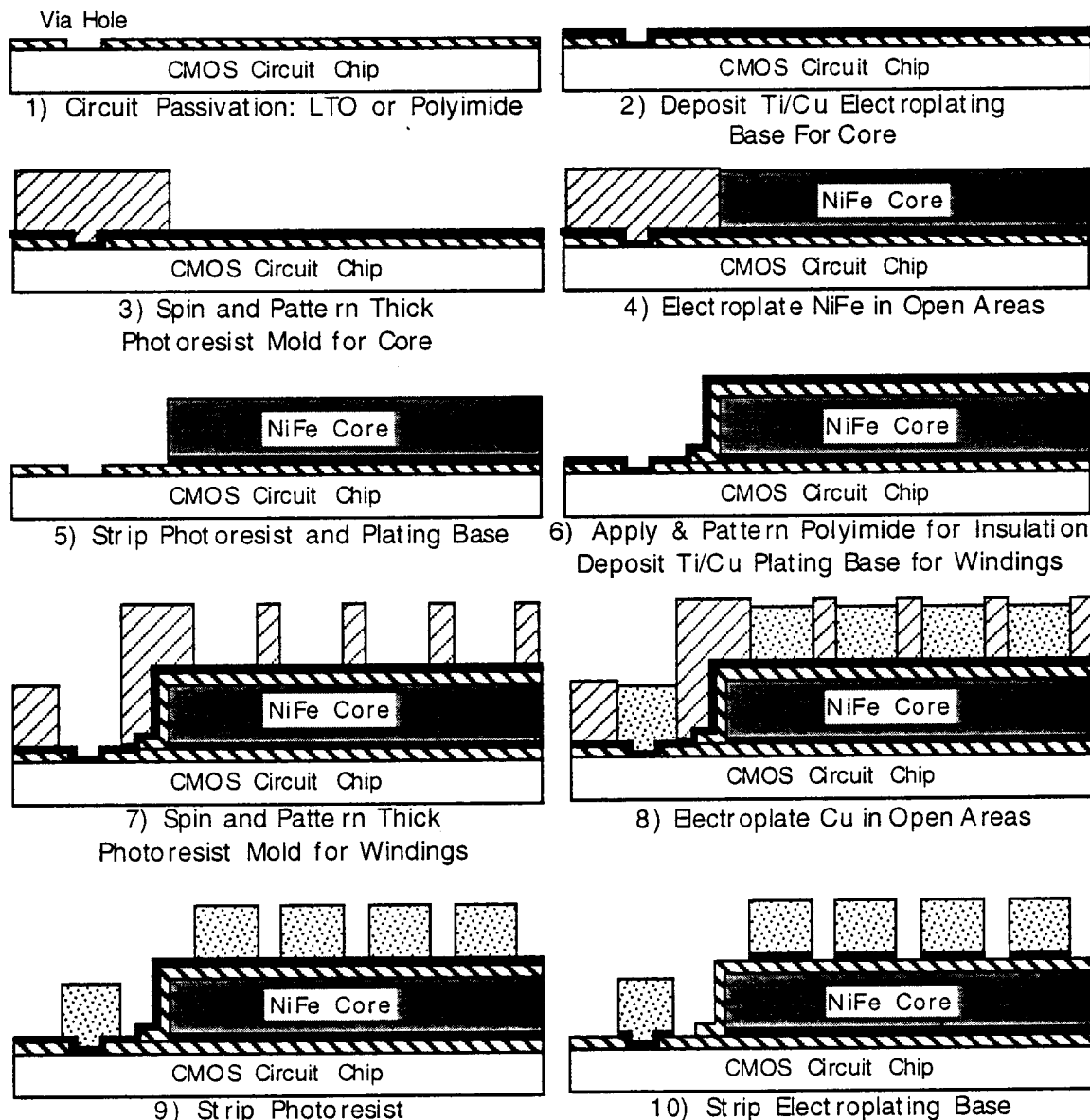


Figure 3.26: Processing steps for fabricating on-chip coils over a CMOS circuit. These steps yield the coil of design D in Figure 3.23.

After the core is electroplated, the photoresist mold is removed and the plating base in the open areas is stripped by wet etch. Polyimide is then spun on to insulate the windings from the core underneath. This thick dielectric layer minimizes the parasitic substrate capacitance, and results in coils with a measured self resonance of over 30 MHz. If this polyimide is cured above about 200° C, stresses tend to delaminate the NiFe core layer, so a long, low temperature cure is best (the crack that can be seen between the NiFe and the silicon substrate in Figure 3.25 is due to this stress). The polyimide then is patterned to allow the copper windings which will be electroplated on top of it to connect with the circuitry below. Either an O₂ plasma and aluminum mask or a photoresist mask and MF-319 can be used to pattern the polyimide.

The electroplating base for the copper windings is then sputtered onto the polyimide surface (500Å Ti and at least 4000Å Cu). The copper plating base for the windings is thicker than the plating base for the core because the windings need to have good step coverage over the core. The electroplating mold for the windings is then formed using a standard thick photoresist process. Ten microns or more of copper is then electroplated to form the windings. Finally, the copper electroplating mold is removed, and the plating base is stripped by wet etch.

3.3.6 Measured Power Reception Of The On-Chip Coils

The fabricated on-chip coils were tested by putting them in an actual telemetry link, and measuring the power received by these coils. The measured power received was compared with the theoretical power received as given by the model. Measurements were made under a variety of conditions, and in every case the actual measured power received agrees remarkably well with the theoretical power received. In the worst case the measured power was about 20% less than the theoretical model predicted, and in many cases it was higher than predicted by the model.

Figure 3.27 is a photograph of the testing setup for measuring the power received by the on-chip coils. A class-E transmitter was used to drive a 16-turn, 25 μ H planar spiral transmitter coil with average winding diameter of 8 cm. The class-E was powered by a 4.5 V DC supply, and it delivered well over 200 V peak amplitude to the transmitter coil at 4 MHz. Note that this setup is not quite identical to the optimized parameters used obtained from the analytical model. One difference is that the analytical model assumed that the transmitter was powered by a 9 V battery, while the actual class-E transmitter used for measurements was powered by a 4.5 V supply. The reason that the actual class-E was powered by a 4.5 volt supply is that this class-E was originally designed and built to work at 2 MHz for powering the microstimulator and this particular class-E did not operate as efficiently at 4 MHz. It was found that when tuned to 4 MHz, components in this class-E would overheat and burn out if more than about 4.5 V was supplied. With a class-E specifically designed to operate at 4 MHz, a 9 V supply can be used, and the transmitted power would be much greater. A second difference is that the transmitter series Q setting resistance was reduced from 7 Ω to about 5 Ω in the actual measurement setup to help make up for the reduced power supply level.

All of the test results reported on here were obtained with 2.9 μ H, 17-turn on-chip receiver coils of Design D in Figure 3.23. The on-chip coils were prepared by attaching them to a small printed circuit board by wire bonds. A parallel capacitor was added to tune the coil to resonate at 4 MHz, and a parallel resistive load was also added. The on-chip coil was powered inductively by the transmitter, and the resulting peak voltage across the load was recorded and used to calculate the power delivered. The FINESSE system requires the received inductively coupled AC signal to be converted to a DC supply voltage. It is the DC power that is of importance, not the AC power. However, in order to keep the measurement setup simple, the peak AC power without rectification was recorded in these experiments. The AC load was then converted to an equivalent DC load, and the peak AC peak power delivered to the AC load was converted to the equivalent DC power delivered.

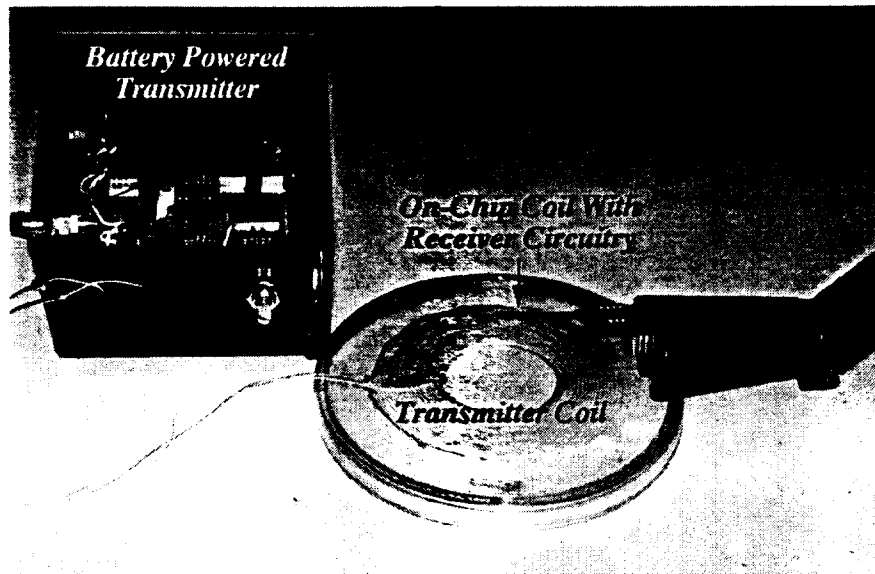


Figure 3.27: The testing setup used to measure the power received by the on-chip coils in an inductively coupled link.

The measured DC power received with an on-chip coil as a function of link distance is given in Figure 3.28. These measurements were made with a $2\text{ k}\Omega$ equivalent DC load. As can be seen, the 25 mW maximum power required by the FINESSE chip can be received at a link distance of just over a centimeter even with the inefficient class-E transmitter running with only half of the target supply voltage. Figure 3.28 includes a curve from the analytical model showing the expected received voltage under these conditions. As can be seen, the measurements closely agrees with the modeled results.

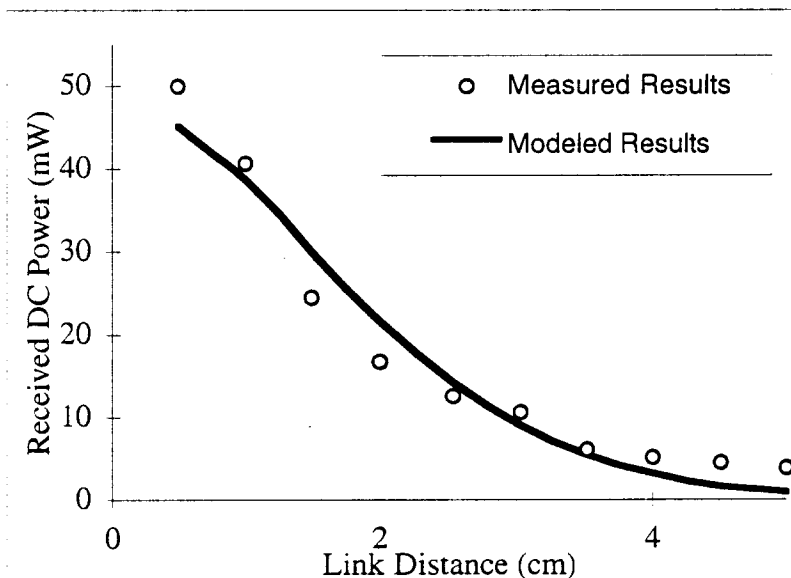


Figure 3.28: Measured DC power received as a function of link distance for a 17-turn, 2 by 10 mm on-chip receiver coil with a $2\text{ k}\Omega$ load, when powered by a 4 MHz class E transmitter with a 4.5 V supply.

The measured power received as a function of DC load resistance is given in Figure 3.29. These measurements were made at a link distance of 1 cm, with a 17-turn on-chip receiver coil. Also shown is the expected power received under these conditions as given by the analytic model. It can be seen that the modeled behavior closely match actual measurements.

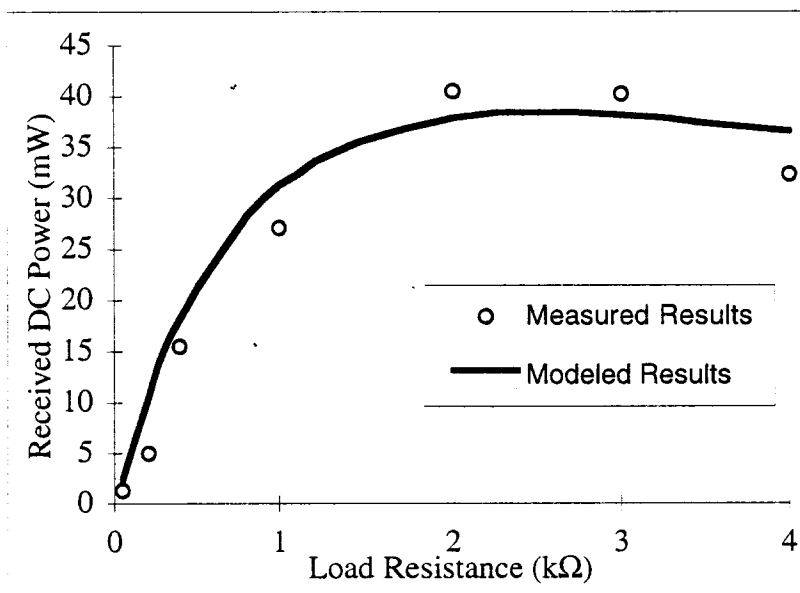


Figure 3.29: Measured DC power received as a function of load resistance for a 17-turn, 2 by 10 mm on-chip receiver coil at 1 cm link distance, when powered by a 4 MHz class-E transmitter.

Figure 3.30 shows the measured power received as a function of the axial misalignment of the coils at a link distance of 1 cm. Also shown in Figure 3.30 is the radius of the transmitter coil. Since the transmitter coil is 8 cm diameter, an axial misalignment of 4 cm means that the relatively small on-chip coil is located right at the edge of the large transmitter coil. As can be seen, a large coil misalignment of up to 2 cm in any direction can be tolerated by this inductive link with almost no degradation in performance. This is important for the FINESSE system because the transmitter coil will most likely be applied and removed from the skin frequently, without careful alignment. It also means that multiple microsystems spread out over a 12.6 cm² area (a circle with 2 cm radius) can be powered by a single 8 cm transmitter coil.

The on-chip coils were also tested by hybrid attaching the analog front end circuitry of the FINESSE chip, as shown in Figure 3.31. The attached chip includes an integrated tuning capacitor, and a full wave rectifier, so that true DC load driving measurements could be obtained. However because the attached chip also includes a 4 Volt regulator, the power delivered to the load was clamped at 4 Volts by this circuit. For this reason it was not possible to measure the maximum power able to be delivered to the DC load by the link with this testing configuration. For this reason only a few measurements were made with this setup, but they did help to confirm the results obtained with AC measurements.

Figure 3.32 shows the 4 V regulated supply from the hybrid attached circuit under full telemetric operation. A 1 μ H, 10-turn, 2 by 10 mm coil with no core (Design A in Figure 3.23) was used as the receiver coil for this photograph. This coil is much less efficient than the 17 turn coil with NiFe core that has been optimized for use with the FINESSE system. However, even this inefficient receiver coil, together with the receiver circuitry and voltage regulator, was able to provide a 4 Volt DC supply and source about 1.5 mA of DC current over link distances of up to about 0.5 cm. This measured 6 mW of DC power agrees with the 8 mW that the model predicts for these 10-turn, air core coils under these circumstances. Notice that the regulated

supply in Figure 3.32 has ripple of a few tenths of a volt. This is because the regulated 4 V supply is just barely able to source 1.5 mA to the load with the inefficient 10-turn, air core coils.

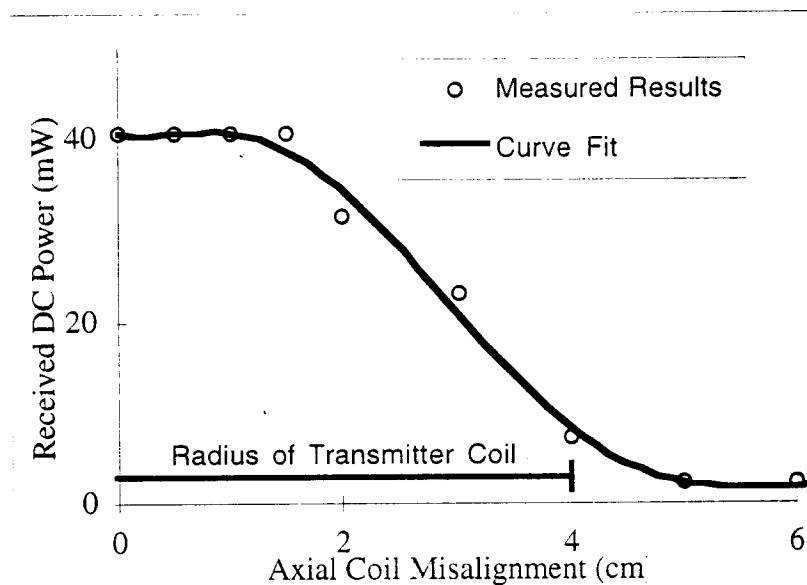


Figure 3.30: Measured DC power received as a function of axial coil misalignment for a 17-turn, 2 by 10 mm on-chip receiver coil with 2 k Ω load at 1 cm link distance, when powered by a 4 MHz class-E transmitter with a 4.5 V supply.

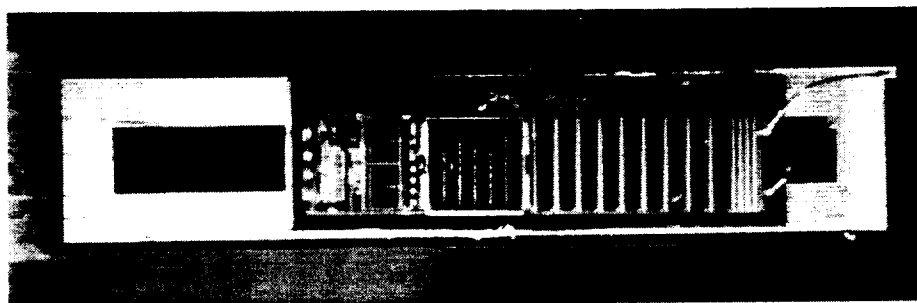


Figure 3.31: An on-chip coil with receiver circuitry hybrid attached for testing.

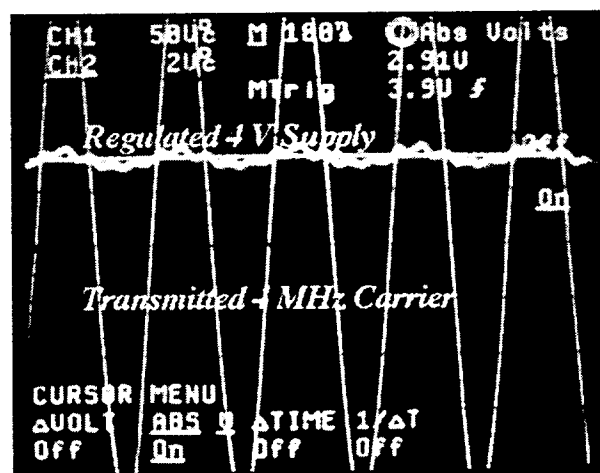


Figure 3.32: The regulated 4 V supply.

3.3.7 Circuit Design

Figure 3.33 shows the layout of the 3.108 transistor, 2.0 mm by 8.7 mm FINESS circuitry. This Bi-CMOS chip consists of an integrated coil for receiving power and data, an analog front end, digital control circuitry, and analog output circuitry. The 2.0 mm by 8.4 mm integrated receiver coil is electroplated directly on top of the circuitry. Power conservation was critical in the circuit design because the FINESS chip is powered through a poorly coupled inductive link, and because there is no capacitor for storing the output charge. Power conservation was less of a concern in previously developed telemetry powered FES systems because they contained a large discrete capacitor which slowly built up the output stimulation charge over time. However, in the FINESS chip the power supply must be able to provide the stimulation current (2 mA) directly from the telemetry link rather than from stored charge. This means that a majority of the received power must be available for stimulation (14 mW out of a total received power of 25 mW), and this puts severe power constraints on the rest of the system circuitry.

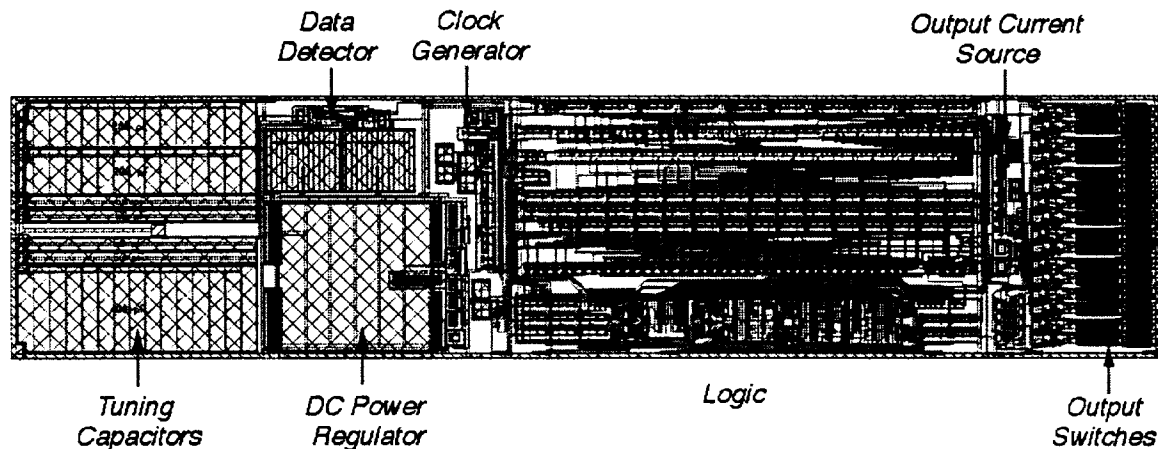


Figure 3.33: The layout of the FINESS circuitry.

Analog Front End Circuitry

The analog front end contains the complete RF receiver circuitry, a 4V power supply generator, a 500 kHz system clock recovery circuit, data detection circuitry, and a power-on detector for reset. This circuitry takes the received RF signal and generates from it the basic signals and supply voltage which the digital circuit and stimulating output circuit need to operate. Because the front end circuitry is the only circuitry in the system which is exposed directly to the received RF signal, it has a number of unique design challenges. This circuitry had to have over voltage protection, and be able to properly operate with input voltages well outside of the power rails. Since the coupling coefficient of the telemetry link vary over a wide range due to such factors as implant depth, transmitter placement, loading, and movement, this circuitry had to be sensitive to a wide range of input conditions, and yet be immune to interference. Also, the front end circuitry needed to operate faster than any other circuitry in the system because it operates at RF speeds. Finally, the front end circuitry needed to consume as little power as possible so that it does not put unnecessary strain on the telemetry link.

System Logic

The FINESS system logic has four functions. First, it takes the signal from the envelope demodulator and recovers the pulse width encoded data. Second, it stores the recovered data until it is needed. Third, it checks the recovered data for proper start codes, device address, and parity. Fourth, it controls all of the timing, amplitudes, and switching of the chip's output waveform. A block diagram for the system logic is shown in Figure 3.34. It contains 5 major blocks: a 10-bit counter/timer, logic associated with the counter/timer to determine what its value means, a 45-bit data register to capture the incoming data, logic associated with the data register to check the parity bits and to check the address, and a 16 state finite state machine for overall control of the system.

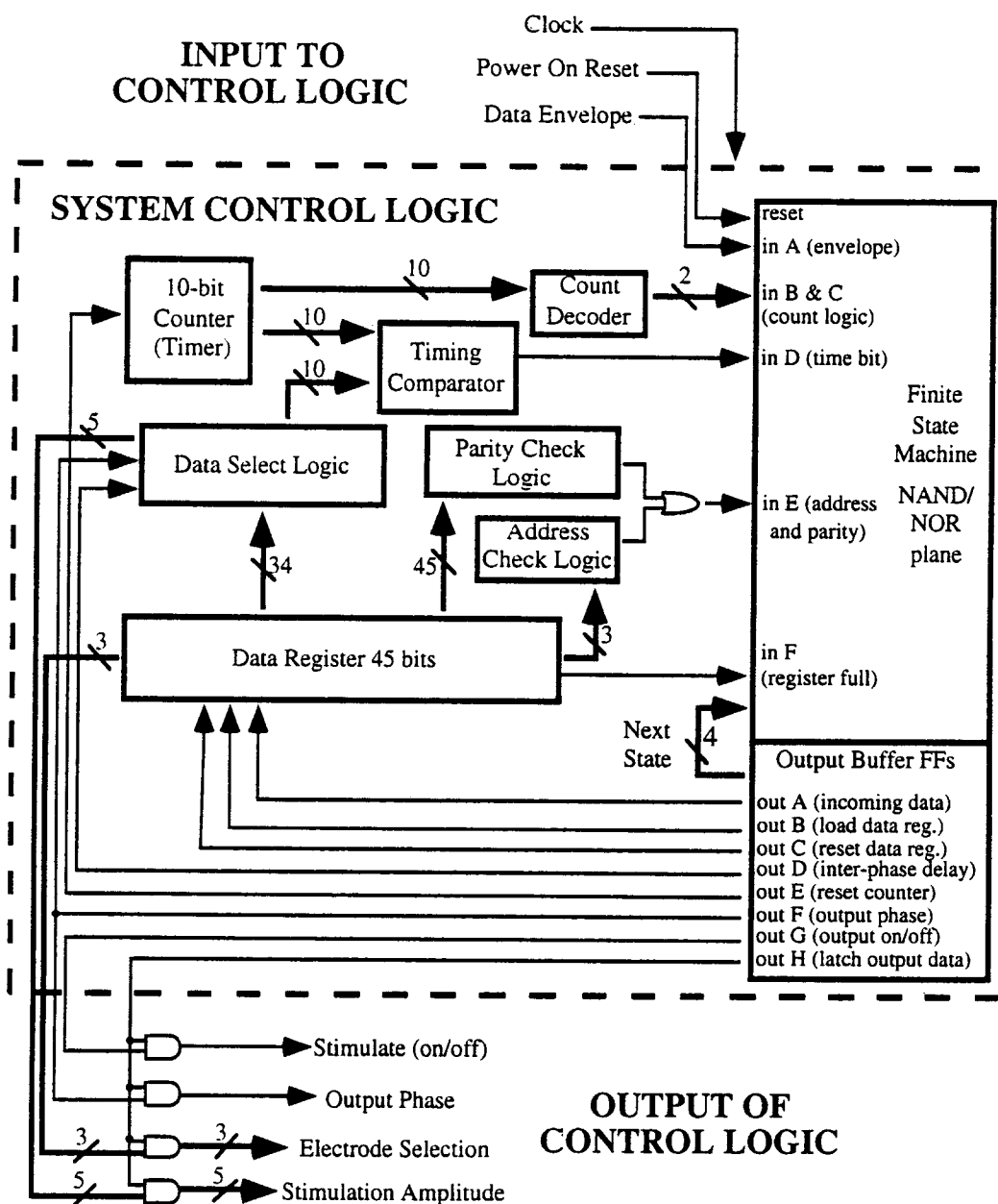


Figure 3.34: A block diagram of the FINESS system logic.

The 10 bit synchronous counter/timer has two purposes. First, it helps to recover the pulse width encoded data from the telemetry envelope by timing the duration of the high and low modulations. Second, it times the duration of the system's stimulating output phases. Using the same counter for both of these tasks saves power and die area, however, it does put one limitation on the system. It means that when the FINESS chip is stimulating, the counter is busy timing the output phases, and hence the system cannot time any incoming pulse width encoded telemetry data. Because of this, all telemetry input is ignored during stimulation.

The logic associated with the counter/timer includes the count decoder and the timing comparator. The count decoder is used to decode the pulse width encoded telemetry data. The decoder monitors the counter/timer and interprets whether a pulse duration signals a bit 1, a bit 0, or a special timing pulse. The timing comparator is used to time the output stimulation duration. The timing comparator constantly compares the output of the counter/timer with the programmed stimulation duration stored in the data register. When the two values match, the timing comparator signals the finite state machine to stop stimulating.

The 45-bit data register is implemented as a serial loading shift register. Logic associated with the data register includes the parity check, the address check, and the data select logic. The data select logic consists of digital multiplexers which pass required bits from the data register on to other system circuitry. The parity check and address check are simple combinational logic blocks which generate a signal indicating whether the received data contains an error or is improperly addressed.

Analog Output Circuitry

The stimulation current generated by the output circuitry is bi-phasic. The two phases are each of programmable amplitude and duration, with a programmable delay between them. In the FINESS system, charge balancing is ensured by exact balancing of the amplitude and duration of the two phases of the stimulation pulse. Although it is easy to implement charge balancing when a blocking capacitor is placed in series with the electrodes, this was not possible in the FINESS system because the required capacitor is too large to reasonably integrate. As a result, charge balancing depends on an accurate system clock to match the relative duration of each phase of the output, and an accurate current source to match the relative amplitude of each phase of the output. Proper charge balancing is also contingent on properly programming of the amplitude and duration of the two stimulation phases so that the charges are equal. It will be up to the external transmitter control circuitry to ensure that the programmed waveforms result in a stimulation output which is charge balanced. The implanted system logic does not check for this.

Output current source

The output current source must be low power, stable (insulated from supply fluctuations), and able to operate over very close to the full supply voltage range. The reason for the latter requirement is that as much of the supply voltage as possible needs to be available to drive the output current through the impedance of the tissue being stimulated, the electrodes, and the interconnect leads.

The FINESS system uses the circuit shown in Figure 3.35 to meet these design constraints. This 5-bit programmable current source provides a stable current over an output voltage swing of 3.7 V when powered by a 4 V supply. It does this by operating the drive transistors (M1 through M5) in the linear region. The proper V_{ds} is established by forcing a reference current (generated by M6 through M8) through a reference FET (M9). A differential

amplifier (consisting of M10 through M16) with negative feedback (through transistor M17) is used to make sure that the V_{ds} of the current source drive transistors (M1 through M5) are identical to the V_{ds} of the reference FET (M9). The reference current is insulated from supply voltage fluctuations because it is generated from a stable V_{be} voltage (generated by Q1 and M18). The current source is 5-bit programmable because it has 5 binary weighted drive transistors (M1 through M5) which are turned on and off by the system logic. In order to minimize the voltage drop across the drive transistors, they are quite large (the largest has a channel which is 320 μm wide).

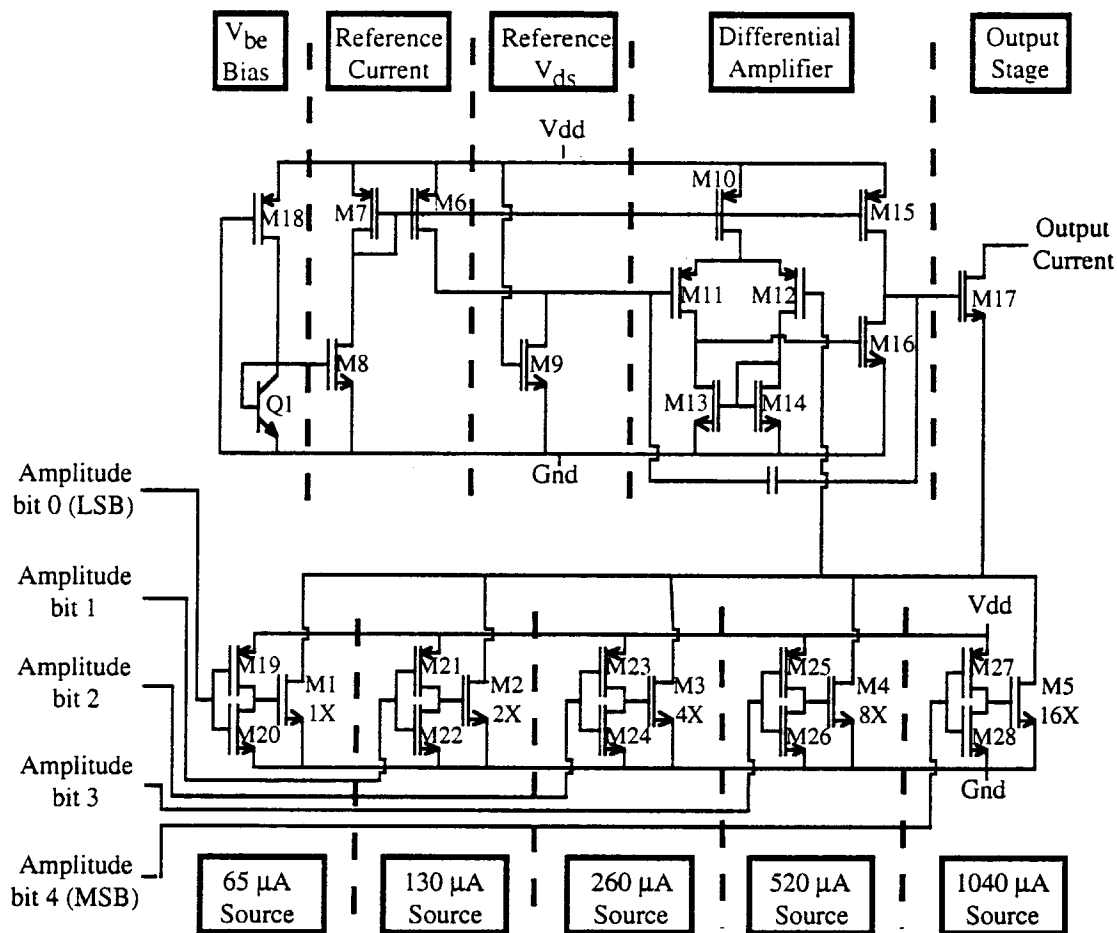


Figure 3.35: The output current source.

The current consumption of the output current source is a constant 90 μA (not including the stimulating output current). Typical supply voltage ripple (8 MHz, 10 mV ripple) causes 2.85 μA of ripple (worst case) on the full scale output current. This current source has less than 8% variation in output current over the output voltage range of 0.3 to 4 volts and less than 3% variation over the output voltage range of 0.4 to 4 volts. When this current source is turned on, the output settles to within 2.5% of its programmed value within 1 μs . The current source has several metal links that can be used to change the full scale output. The links were included to add flexibility, and to allow the stimulation level to be hand trimmed to counteract process variations. 2 mA was chosen as the default full scale current level because it is anticipated that most applications will require currents in this range. However, for some applications a larger current range (with a correspondingly coarser 5-bit current resolution) or a smaller current range (with a correspondingly finer 5-bit current resolution) may be desirable. By cutting links the full scale output of the FINES chip can be reduced to less than 0.3 mA or increased to over 10 mA.

It should be noted that increasing the current source to over 2 mA will not work if the FINESSE chip does not receive enough power from the telemetry link to supply this much current.

Output current switching and demultiplexing

The current generated by the output current source is directed to one of eight possible sets of electrodes by the output switching and demultiplexing circuitry shown in Figure 3.36. Both phases of the output current are generated from a single supply voltage. During the first phase (the stimulation phase) the current source sinks current from the cathodic electrode while the anodic electrode is held at V_{dd} . During the second phase (the charge balancing phase) the same current source sinks current from the anodic electrode while the cathodic electrode is held at V_{dd} . The switching of the cathodic and anodic electrodes occurs during the interphase delay. All of the electrodes not being used during a stimulation period, and all of the electrodes in between stimulation periods are left floating by the output switches. This ensures that no significant charge is passed by these electrodes. As can be seen in Figure 3.36, the switching of the output current between the various pairs of stimulating electrodes is done by FETs. These FETs are made very wide so that excessive voltage is not lost across them during stimulation. When stimulating with a full scale output, the total voltage drop across the switching FETs is 0.3 Volts (0.15 across each of the anodic and cathodic electrode switches).

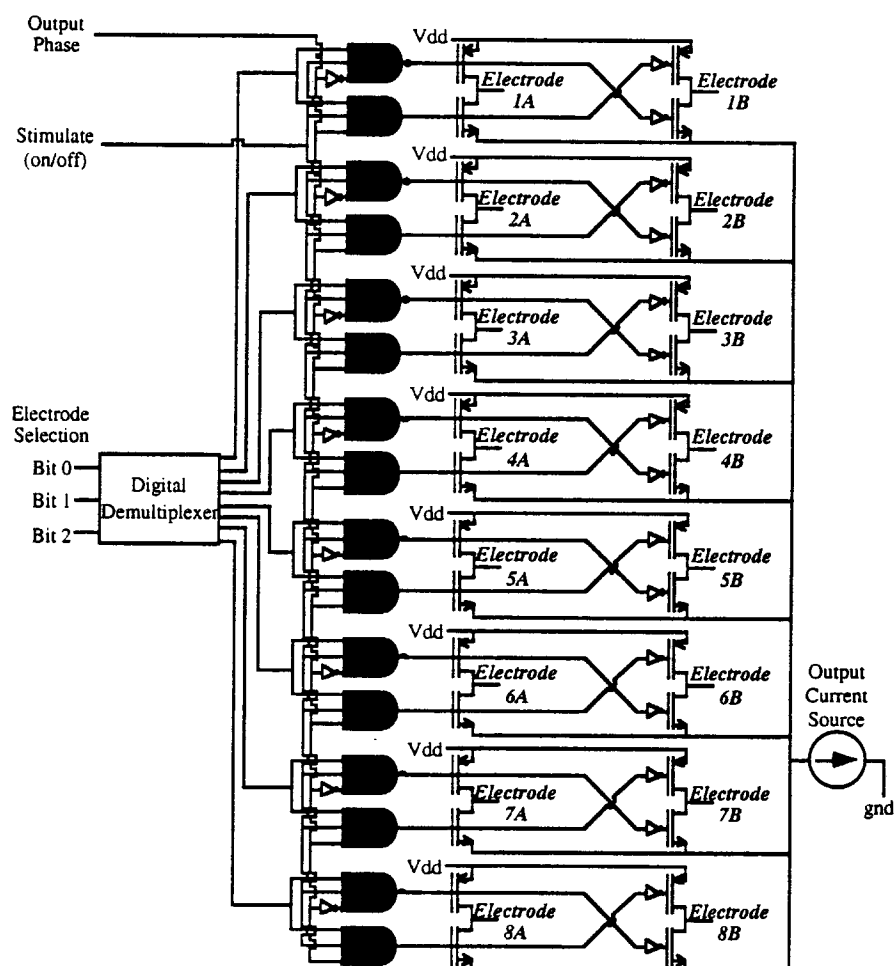


Figure 3.36: The output switching and demultiplexing circuitry.

3.3.8 Telemetry Communications Protocol

The FINESS system is controlled through the same 4 MHz inductive link through which it receives power. The power carrying signal is amplitude shift keyed at about 15 kHz with pulse width encoded digital data. Amplitude shift keying was chosen over frequency shift keying because it makes it much easier to implement the demodulation circuitry in the limited die area and limited power budget available on the FINESS chip. The FINESS chip is designed to respond to an amplitude modulation factor of about 10% (the amplitude of the modulating signal should be about 10% of the amplitude of the carrier). A lower modulation factor may not trigger the detection circuitry, and a higher modulation factor will be less efficient at providing power. The data is encoded in pulse widths of 66% duty cycle (for a bit = 0) and 33% duty cycle (for a bit = 1), as shown in Figure 3.37. Pulse width encoding is a reliable way to transmit data because each bit contains two amplitudes which can be read differentially. It is important that the data be read differentially since the absolute amplitude of the transmitted signal may vary due to transmitter placement, receiver orientation, transmitter loading, battery drain, and other reasons.

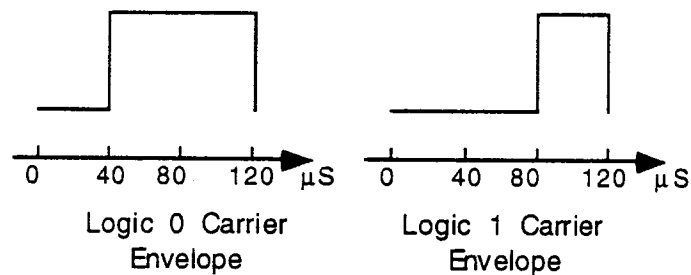


Figure 3.37: Nominal envelope for a transmitted bit 0 and bit 1.

Figure 3.38 shows an illustration of the transmission protocol, and Table 19 gives a breakdown of the transmitted bits required for stimulation. Each stimulation pulse requires a total of 45 digital bits to be transmitted, plus two synchronization pulses. The complete data stream along with the synchronization pulses nominally requires 5.8 ms to transmit, as shown in Table 20. This means that a theoretical maximum of 172 stimulations can occur each second. However, the actual maximum stimulation frequency of the FINESS chip varies depending on the programmed duration of the output stimulating waveform.

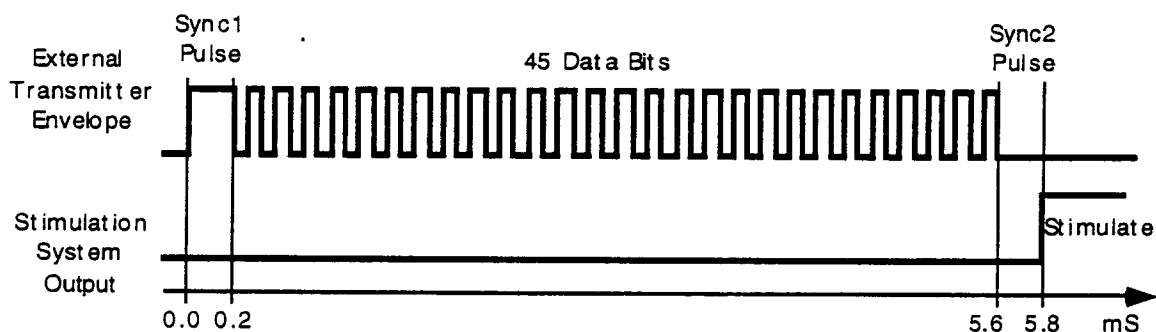


Figure 3.38: The nominal timing for the data envelope.

Table 19: The 45 data bits which are transmitted for each stimulation.

Parameter	Range	Required Bits
Address of Device	Selection from up to 8 devices	3 bits
1st Phase Current Magnitude	0 to 2 mA (32 steps of 64.5 μ A)	5 bits
2nd Phase Current Magnitude	0 to 2 mA (32 steps of 64.5 μ A)	5 bits
Electrode Selection	Selection from 8 electrodes pairs	3 bits
1st Phase Duration	4 to 2050 μ s (1024 steps of 2 μ s)	10 bits
Inter-phase Delay	12 to 1932 μ s (16 steps of 128 μ s)	4 bits
2nd Phase Duration	4 to 2050 μ s (1024 steps of 2 μ s)	10 bits
Parity Bits		5 bits
<i>Total</i>		<i>45 bits</i>

Table 20: Breakdown of the required time to telemetrically program the FINESS chip.

Transmission for new stimulation	Transmission Time
1st Sync. Pulse	0.2 ms
40 data + 5 parity bits (each bit)	5.4 ms (120 μ s)
2nd Sync. Pulse	0.2 ms
<i>Total</i>	<i>5.8 ms</i> <i>(172 per sec)</i>

The telemetry protocol for the FINESS chip is a strict one, designed to minimize the chance of an error going undetected. It is important to realize that since the FINESS chip has only a unidirectional telemetry link, there can be no data handshaking in the transmission protocol. Therefore, data is sent to the device only once, with a very strict transmission protocol and 5 parity bits. If an error is detected in the received data, the FINESS chip will not stimulate. Instead, the chip will reset and wait for the next transmission sequence. This strict telemetry protocol helps to avoid unwanted stimulation even in noisy environments.

Before transmitting any data bits, the transmitter sends the first of two synchronization pulses, as shown in Figure 3.38. The first synchronization pulse is an unmodulated high amplitude pulse of at least 135 μ s duration. Since data bits contain high amplitude pulses of 40 μ s or 80 μ s (depending on if the bits are a 1 or a 0), the 135 μ s synchronization pulse is a unique signal which is easily distinguishable in this transmission scheme. The first synchronization pulse resets the FINESS chip, and lets the device know that data transmission is about to begin. Any data sent that is not preceded by the first synchronization pulse is ignored.

Immediately following the first synchronization pulse, the 40 pulse width encoded data bits and 5 pulse width encoded parity bits are transmitted at 120 μ s per bit (nominally) as illustrated in Figure 3.37 and Figure 3.38. Both the time that the envelope is low and the time that the envelope is high are monitored for each bit, and if the high and low times do not clearly indicate whether the bit is a 1 or 0, the FINESS chip will recognize that an error has occurred, and it will reset itself without stimulating. The order in which the data and parity bits are transmitted is given in Table 21. One parity bit is transmitted after every 8 data bits, forming a 9 bit word. An even parity scheme is used, meaning that the parity bit is selected such that there is an even number of 1's in each 9 bit word. If any received word does not pass parity check, the FINESS chip will reset itself without stimulating.

Immediately following the 45 data and parity bits, a second synchronization pulse must be transmitted, to confirm that data transmission is complete. This second synchronization pulse is an unmodulated low amplitude pulse of at least 135 μ s duration (unique and easily distinguishable from the 40 and 80 μ s low pulses which make up data bits, and from the 135 μ s high pulse which makes up the first synchronization pulse). If the implanted FINESS chip has not yet received the required 45 data bits when the second synchronization pulse is received, a transmission error has occurred and the device resets without stimulating. Likewise, if the system has received the required 45 data bits, and more data is received rather than a second synchronization pulse, a transmission error has occurred and the system will reset without stimulating.

Only after the second synchronization pulse is correctly received by the FINESS chip does stimulation begin. During stimulation, the FINESS chip ignores all telemetry signals until the entire stimulation sequence is complete. There is no way to abort stimulation once it has begun, except by powering down the chip. Only after the entire stimulation sequence is completed will the FINESS chip recognize a first synchronization pulse, and accept new transmitted data. It is up to the external transmission system to wait the required stimulation time before sending sequential stimulation commands to the same implanted device, and this stimulation time varies from 0.020 ms to 6.03 ms depending on the programmed output duration. If there are multiple FINESS chips with unique addresses, then sequential stimulation commands can be sent to different chips without having to wait for the output stimulation sequence from the first chip to finish.

Up until now only nominal transmission times for a zero bit, a one bit, and a first and second synchronization pulse have been given. However, there is actually a range of allowable transmission times for each of these signals. For example, in order to transmit a zero bit, the RF telemetry envelope is nominally low for 40 μ s as shown in Figure 3.37, however, the envelope can actually be low for anywhere from 4 μ s to 68 μ s. Similarly, the high duration for a zero bit is nominally 80 μ s, but the signal can actually be high for anywhere from 69 μ s to 134 μ s. Table 22 lists the allowable duration for the telemetry envelope to be low and high in this telemetry protocol. The ranges of allowable times for each signal are unique and do not overlap, so that each signal can be uniquely identified by the FINESS chip without ambiguity. Any envelope state lasting less than 4 μ s is interpreted as a glitch, and if the FINESS chip receives a glitch it will reset without stimulating.

Table 21 lists the order in which the 40 data bits and five parity bits need to be sent. First, the 3 bit address of the particular FINESS chip to stimulate is sent. Up to 8 implantable chips can be individually addressed from a single transmitter. If the address sent does not match the address of a particular FINESS chip, then the chip will ignore all further input until the next first synchronization signal is sent. The address of each individual chip is programmed prior to implant by cutting metal links with a laser.

The next 13 data bits to be sent are the 5 bit first phase current magnitude, the 5 bit 2nd phase current magnitude, and the 3 bit electrode selection. This data (and in fact all of the data in this transmission protocol) is sent most significant bit (MSB) first. The current magnitude bits program the stimulating amplitude of each phase of the output waveform. The electrode selection bits choose the desired pair of stimulating electrodes from the 8 sets of bi-polar electrodes.

The final 24 bits of data control the timing of the output waveform, and are made up of the 10 bit first phase duration, the 4 bit interphase delay, and the 10 bit second phase duration. The durations of the first and second phase are independently programmable, and any combination of phase magnitude and duration is allowed, whether they properly charge balance the electrodes or not.

Table 21: The order in which the 45 data bits must be transmitted.

1	MSB of device address	24	next bit of phase 1 duration
2	next bit of device address	25	next bit of phase 1 duration
3	LSB of device address	26	next bit of phase 1 duration
4	MSB of phase 1 current mag.	27	parity for preceding 8 bits
5	next bit of phase 1 current mag.	28	next bit of phase 1 duration
6	next bit of phase 1 current mag.	29	LSB of phase 1 duration
7	next bit of phase 1 current mag.	30	MSB of inter-phase delay
8	LSB of phase 1 current mag.	31	next bit of inter-phase delay
9	parity for preceding 8 bits	32	next bit of inter-phase delay
10	MSB of phase 2 current mag.	33	LSB of inter-phase delay
11	next bit of phase 2 current mag.	34	MSB of phase 2 duration
12	next bit of phase 2 current mag.	35	next bit of phase 2 duration
13	next bit of phase 2 current mag.	36	parity for preceding 8 bits
14	LSB of phase 2 current mag.	37	next bit of phase 2 duration
15	MSB of electrode selection	38	next bit of phase 2 duration
16	next bit of electrode selection	39	next bit of phase 2 duration
17	LSB of electrode selection	40	next bit of phase 2 duration
18	parity for preceding 8 bits	41	next bit of phase 2 duration
19	MSB of phase 1 duration	42	next bit of phase 2 duration
20	next bit of phase 1 duration	43	next bit of phase 2 duration
21	next bit of phase 1 duration	44	LSB of phase 2 duration
22	next bit of phase 1 duration	45	parity for preceding 8 bits
23	next bit of phase 1 duration		

Table 22: The allowable timing of the data envelope.

State of Envelope	Meaning of Envelop State	Allowable Duration of State (μ s)
high	Time high for transmitted bit=1	4-68
	Time high for transmitted bit=0	69-134
	2nd synchronization pulse	>134
low	Time low for transmitted bit=0	4-68
	Time low for transmitted bit=1	69-134
	1st synchronization pulse	>134

3.3.9 FINESS Chip Test Results

The FINESS chip was fabricated, tested, and found to work perfectly. Figures 3.39 through 3.41 are photographs of fabricated and fully functional FINESS circuitry. In order to allow the circuitry to be clearly seen, the die in Figure 3.39 does not have an electroplated coil on top of it. Figure 3.40 shows a photograph of the chip with an integrated electroplated coil. This coil has 17 turns, and the electroplated copper lines are 10 μm thick. As can be seen, the links for tuning the receiver circuitry are still accessible even after the coil is electroplated on top. Figure 3.41 shows a close up optical photograph of the FINESS chip with integrated coil.

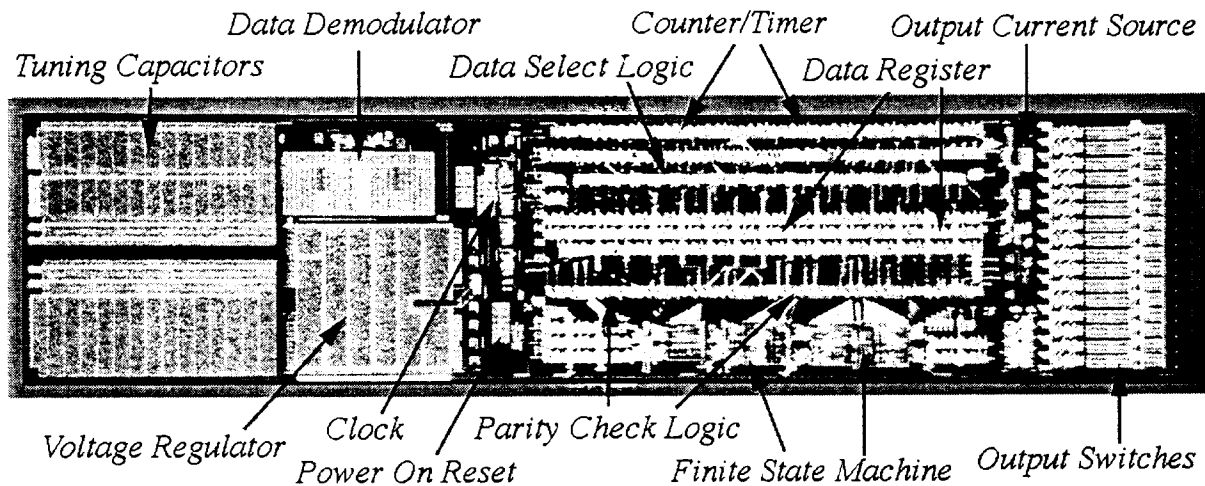


Figure 3.39: A photograph of the fabricated FINESS circuitry without the on-chip coil.

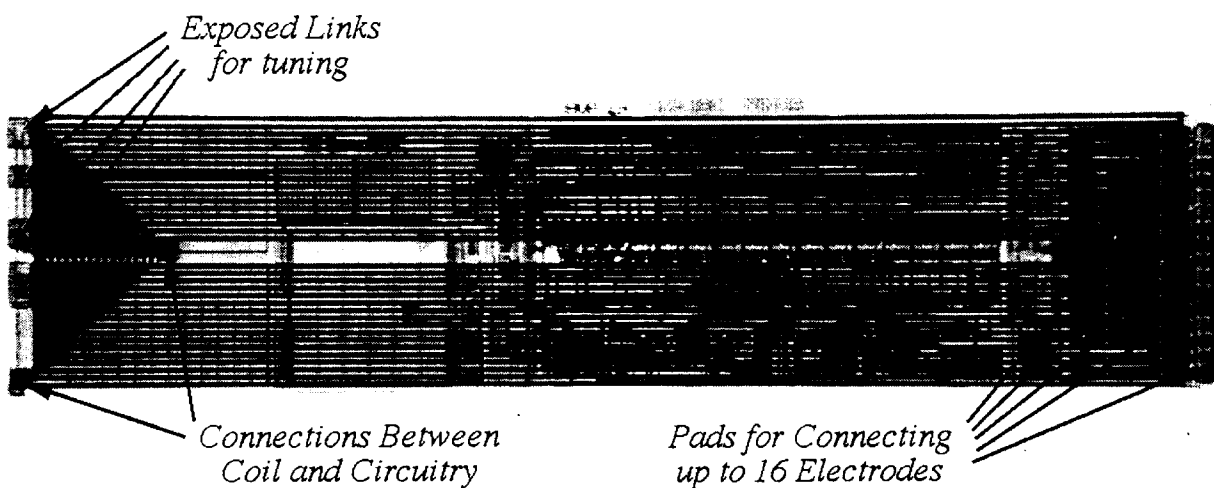


Figure 3.40: A photograph of the fabricated FINESS circuitry with an integrated 17 turn on-chip coil.

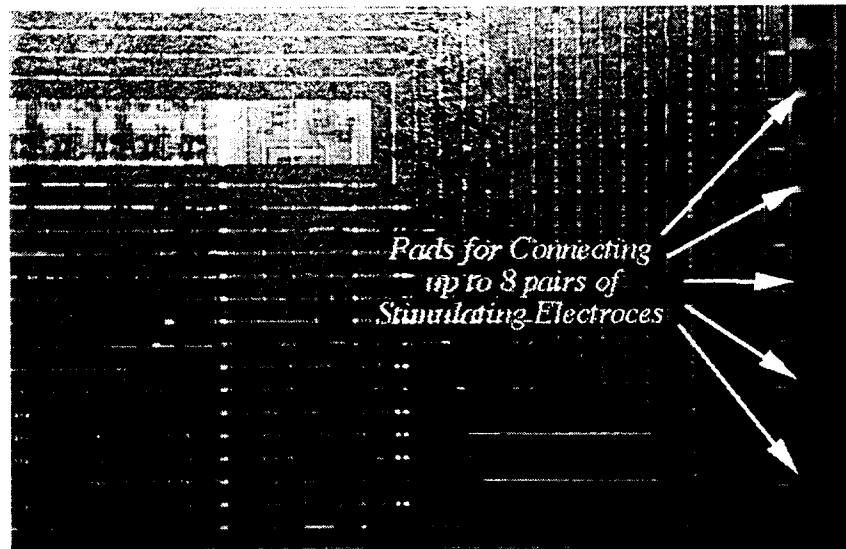


Figure 3.41: Detail of the FINESS circuitry with an integrated 17 turn coil.

3.3.10 Electrical Test Results From The FINESS Chip

Figure 3.42 shows the bi-phasic stimulating output of the FINESS chip across a $1\text{ k}\Omega$ load when the proper amplitude modulated RF signal is applied to the coil pads. In this figure, the chip is programmed to stimulate with a first phase of 1.5 mA amplitude and 1 ms duration, and a second phase of 0.75 mA amplitude and 2 ms duration. The inter-phase delay is programmed to be 0.3 ms. As can be seen, the output stimulation waveform is exactly as programmed. This photograph was taken with no external inputs applied to the FINESS chip other than the modulated RF signal. The chip is generating its own voltage supply from the received RF signal; it is generating its own system clock from the received RF signal, and it is correctly decoding the digitized data from the modulated RF signal. Notice that the applied RF signal is loaded down slightly during both phases of the stimulation pulse due to an increased current draw of the chip when stimulating. Figure 3.43 shows a series of stimulating pulses from the FINESS chip. As can be seen, stimulation frequencies of 150 Hz can easily be obtained with this chip.

Many different combinations of programmed stimulation phase amplitudes, stimulation phase durations, electrode pair selections, and inter-phase delays were tested, and in every case the FINESS chip did exactly what it was supposed to do. Figure 3.44 shows the output of the FINESS chip when the RF received signal is exactly the same as in Figure 3.42, except for a single parity bit which was changed to be wrong. As can be seen, the FINESS chip correctly recognized the bad parity and did not stimulate. In a similar test, a single bit in the device address in the RF signal was changed to be wrong, and again the FINESS chip correctly recognized the bad address and did not stimulate. In a third test, a single bit of data was changed to be inconsistent (the envelope high duration indicated a zero bit, and the envelope low duration indicated a one bit) and again the chip correctly recognized the inconsistent data and did not stimulate. Finally, an improperly timed synchronization pulse was sent to the chip, and the chip correctly recognized an error and did not stimulate. In each of these cases, as soon as the error was corrected in the transmitted data stream, the FINESS circuit immediately started stimulating with the exact waveform shown in Figure 3.42.

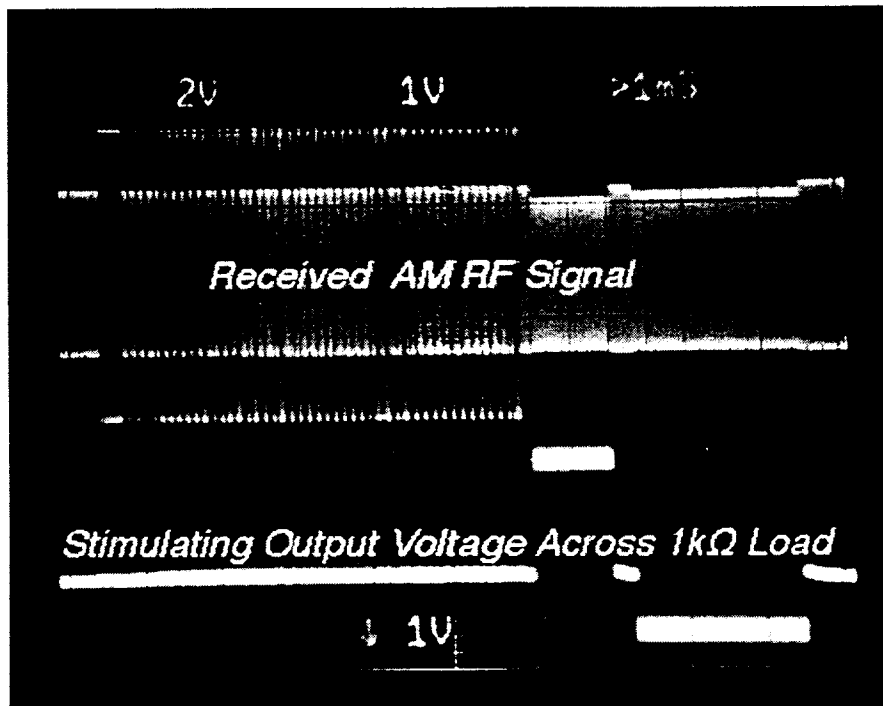


Figure 3.42: An oscilloscope trace showing the stimulating output across a 1 k Ω load resistor.

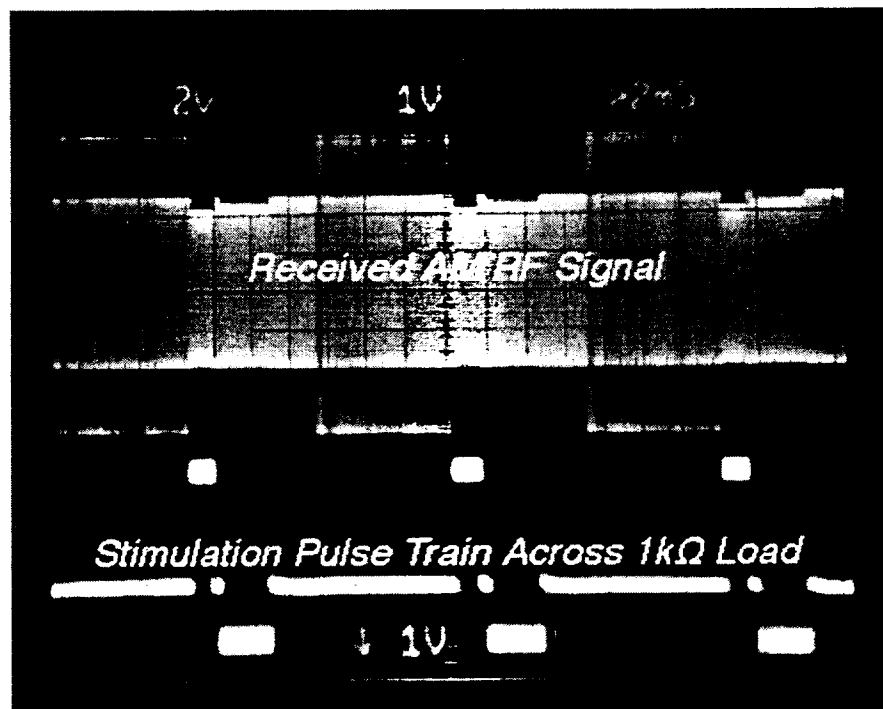


Figure 3.43: A photograph trace showing a train of 150 Hz stimulating outputs pulses.

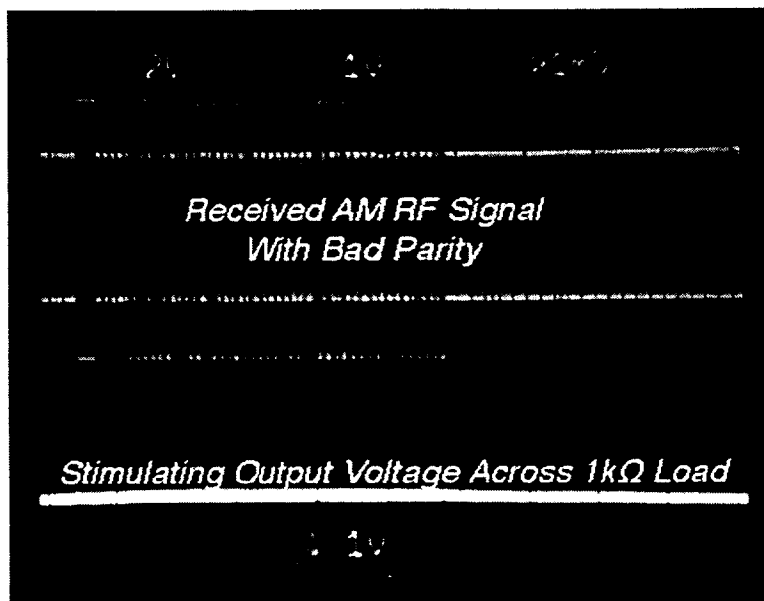


Figure 3.44: The stimulating output when the telemetry input signal is exactly the same as in Figure 3.42 except one parity bit has been changed to be invalid. The circuitry correctly recognizes the bad parity bit and does not stimulate.

The logic of the FINESS chip was tested by cycling through many of the possible 45-bit programmed input possibilities (but obviously not all of the input possibilities because there are over 10^{13} of them). Every single one of the dozens of tested input combinations resulted in the logic doing exactly what it was programmed to do. First, the system was programmed to stimulate at many different output pulse durations. The logic correctly timed the output pulse duration in every case. The system was then programmed to stimulate each of the eight electrode pairs. In each case, the logic selected the correct electrode pair. Finally, the system was programmed to stimulate at each of the 32 output stimulation magnitudes, and again in every case the proper magnitude bits were output by the logic at the proper time. The logic was also tested to see that it correctly rejected incoming data which contained either one or more incorrect parity bits, an incorrect device address, a data bit with inconsistent pulse width encoding, or incoming data that did not contain the proper synchronization codes. In each of these cases it was found that the logic correctly rejected the incoming data, and reset.

The programmable output current source of the FINESS chip has an amplitude which is 5-bit programmable (32 discrete levels). Figure 3.45 shows the programmable output current source of the FINESS chip ramping through all 32 discrete stimulation levels. As can be seen, the response of the output current source is almost perfectly linear with respect to the programmed amplitude. Although the current source was designed to have a full scale amplitude of 2 mA, the actual measured full scale current amplitude is about 2.8 mA. This is due to the transistor threshold values being lower than target. However, there are ample links in the output current source which allow the full scale amplitude to be adjusted by laser cutting. Cutting a few links in the circuit will set the full scale stimulating magnitude to be 2 mA or any other reasonable value.

The measured power requirements of the FINESS chip are given in Table 23. The system was designed to have a non-stimulating current draw of 0.63 mA, but it has a measured non-stimulating current draw of 1.56 mA, or 2.4 times higher than designed. Most of this excess current is due to junction leakage. The designed current draw does not include junction leakage

because the SPICE models used to simulate the circuitry do not include this effect. A second reason for the excess current is that the threshold for both n and p channel FETs are both 10% lower than their target value. The lower thresholds result in higher currents in all of the analog circuit blocks. Although the current draw of the system is higher than anticipated, the inductively coupled link for powering should still be able to supply enough power in all cases, except when the link is at its most distant.

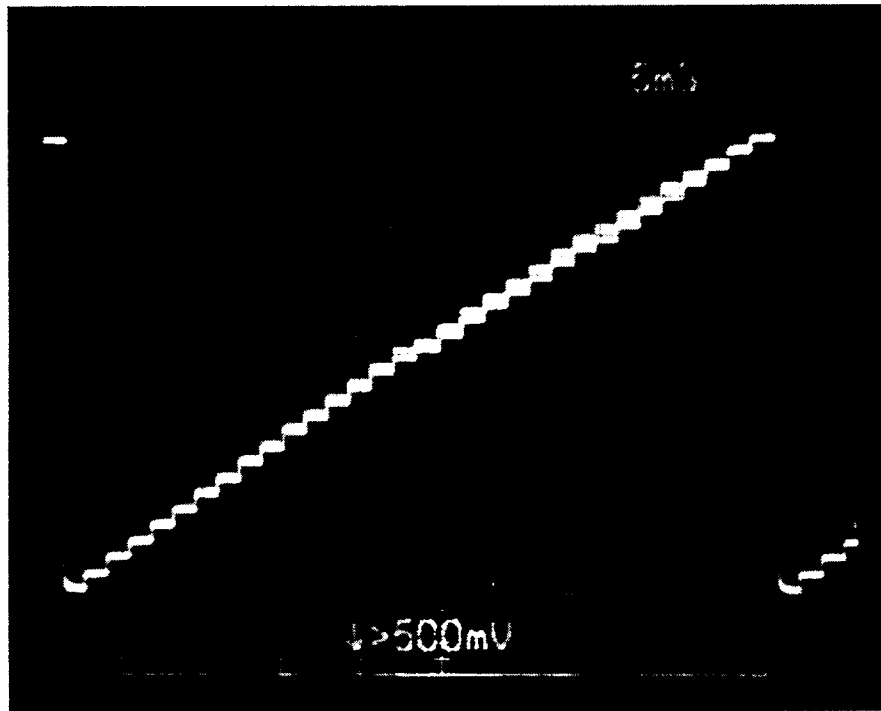


Figure 3.45: The FINESS chip stimulating output current source ramping through all 32 programmable stimulation levels.

Table 23: The measured power requirements of the FINESS chip.

Measured Parameter	Average	Designed Target
DC current (non-stimulating)	1.56 mA	0.63 mA
DC current (maximum stimulation)	3.7 mA	2.63 mA
Power draw from on-chip 4 V supply (non-stimulating)	6.28 mW	2.52 mW
Power draw from on-chip 4 V supply (maximum stimulation)	14.8 mW	10.52 mW
Peak voltage system needs to receive from coil to generate 4 V supply	6.78 V	7 V
Power needing to be received through coil (non-stimulating)	10.57 mW	4.41 mW
Power needing to be received through coil (maximum stimulation)	25.1 mW	18.41 mW

4. Conclusions

This final report summarized work performed over the past three and a half years to develop hermetic packages and feedthroughs for a variety of implantable neural prostheses and stimulators, as well as work on the development of implantable single- and multi-channel implantable microstimulators for use in functional neural stimulation. The primary objectives of the past contract were: 1) the development and characterization of hermetic packages for miniature, silicon-based, implantable three-dimensional structures designed to interface with the nervous system for periods of many decades; 2) the development of techniques for providing multiple sealed feedthroughs for the hermetic package; 3) the development of custom-designed packages and systems used in chronic stimulation or recording in the central or peripheral nervous systems in collaboration and cooperation with groups actively involved in developing such systems and establishing the overall biocompatibility of these packages; and 4) the development of single-channel and multichannel microstimulators that will serve as a vehicle to demonstrate the suitability of the packages and feedthroughs.

During the past three contract periods, our research and development program has made considerable progress in a number of areas related to the above goals. A hermetic packaging technique based on electrostatic bonding of a custom-made glass capsule and a supporting silicon substrate has been developed. This technique allows the transfer of multiple interconnect leads between electronic circuitry and hybrid components located in the sealed interior of the capsule and stimulating electrodes located outside of the capsule. The glass capsule can be fabricated using a variety of materials and can be made to have arbitrary dimensions as small as a few cubic millimeters. Long-term tests of glass packages in high temperature saline and deionized water baths has shown them to be hermetic for a period of at least 40 years.

A multiple sealed feedthrough technology has been developed that allows the transfer of electrical signals through polysilicon conductor lines located on a silicon support substrate. Several hundred feedthroughs can be fabricated in a length of less than 1.5mm. The feedthroughs have also been tested under accelerated test conditions and have shown to be functional in these conditions. The packaging and feedthrough techniques utilize materials that are biocompatible and can be integrated with a variety of micromachined silicon structures.

The packaged and feedthroughs have been implanted in several animal models in collaboration with colleagues at Vanderbilt University, University of Michigan, Hines VA Hospital, and several other groups. These implants have been performed for periods ranging from a few weeks up to one year. The results from all of these in-vivo tests are consistent and show no sign of significant damage to the biological tissue. The packages have also been tested after explantation for sign of moisture penetration and they seem to be intact, unless mechanically damaged during surgery. The project provided several tens of packages to investigators around the country for biocompatibility tests and will continue to do so in the future.

A mixed analog-digital circuit block based on CMOS and bipolar technologies has been developed. This circuit receives a modulated RF carrier from the transmitter and generates regulated power supplies, control data, clock, and regulated stimulation currents that are delivered to the tissue through the on-chip stimulating electrodes. Voltage and current regulators are implemented using bipolar devices, while control logic is implemented using low-power CMOS circuits. These devices are fabricated using a unique Bipolar-CMOS technology that has been developed in our laboratory during our previous contracts.

During this past contract several implantable microstimulators were developed. An inductively-powered single-channel microstimulator capable of delivering charge-balanced pulses through IrOx electrodes formed on a silicon substrate has been developed and shown to be

fully functional. We also developed a multi-channel version of this microstimulator. This device provides eight electrodes for stimulation, has programmable amplitude and duration, and utilizes much more reliable circuit blocks for power generation, clock recovery, data recovery, and current delivery. The circuit blocks are designed to operate with very small amount of power, and are much more tolerant to process parameter, and data modulation variations. In addition, the second generation device has incorporated an on-chip active transmitter, thus providing a bi-directional telemetry link. The on-chip transmitter, allows the microstimulator to communicate with the outside world in order to perform several functions, including hand shaking for reliable data transfer and package integrity tests to inform the user when the package is compromised. In the future, this device design can be used to transmit sensed data from the implant to the outside world, which is a crucial function for many next generation implantable systems needed for neural prostheses.

Since many future implantable systems, such as those used for peripheral nerve stimulation, require smaller profiles (i.e., smaller heights), it is desirable to eliminate the use of hybrid components such as coils and capacitors which are required for telemetry applications. During the past contract our group also developed on-chip coils monolithically integrated with electronics circuits to reduce the height of wireless implantable systems to below 1mm, including the package. We have demonstrated that these on-chip coils are capable of receiving at least several milliwatts of power at a distance of several centimeters from an external transmitter and can easily power an integrated circuit chip and deliver current to the tissue. An 8-channel integrated circuit chip with on-chip coils has been designed, and fabricated, to deliver constant current pulses of up to 2mA in amplitude to peripheral nerves through any 8 user-selected channels. This system has recently been tested and shown to be fully functional. In the future packaged and assembled versions of this system will be built and delivered to outside investigators for further testing.

The combination of the above technologies has allowed us for the first time to implement a implantable systems. Obviously the road ahead is both exciting and challenging, and based on our past progress we believe that fully functional, robust, and practical multichannel implantable microstimulators for a variety of applications can be fabricated. We believe that we have achieved most of the objectives stated in the original proposal.

5. Papers and Theses Produced By The Current Contract

1. K. Najafi, "Integrated Sensing Systems in Closed Loop Neural Prosthesis," Invited Keynote Speaker, *European Solid-State Sensors and Actuators Conf., EUROSENSORS*, Toulouse, France, September 1994
2. K. Najafi, "Sensor/Circuit Integration in Biomedical Applications," Invited Presentation, *European NEXUS Workshop on Sensor/Circuit Integration*, Toulouse, France, Sept. 29-30, 1994
3. M. Nardin, B. Ziaie, J. Von Arx, A. Coghlan, M. Dokmeci, and K. Najafi, "An Inductively Powered Microstimulator for Functional Neuromuscular Stimulation," *13th International Symposium on Biotelemetry*, pp. 99-104, Williamsburg, VA, April 1995
4. K. Najafi, "Silicon-Based Electronic Interfaces to Biological Systems," Invited Speaker at the Workshop on "Bio-Mechatronics" held as part of the 1995 *IEEE Int. Conference on Robotics and Automation*, Nagoya, Japan, May 22-27, 1995
5. M. Nardin, and K. Najafi, "A Multichannel Neuromuscular Microstimulator With Bi-Directional Telemetry," *1995 Int. Conference on Solid-State Sensors and Actuators, Transducers '95*, pp. 59-62, Stockholm, Sweden, June 1995
6. J. Von Arx, B. Ziaie, M. Dokmeci, And K. Najafi, "Hermeticity Testing of Glass-Silicon Packages with On-Chip Feedthroughs," *1995 Int. Conference on Solid-State Sensors and Actuators, Transducers '95*, pp. 244-247, Stockholm, Sweden, June 1995
7. K. Najafi, "Recent Progress in Micromachining Technology and Applications in Implantable Biomedical Systems," Invited Lecture, *Proceedings, Sixth Int. Symp. on Micro Machine and Human Science, MHS '95*, pp. 11-20, Nagoya, Japan, October 1995
8. B. Ziaie, J. A. V. Arx, M.R. Dokmeci, and K. Najafi, "A Hermetic Glass-Silicon Micropackage with High-Density On-Chip Feedthroughs for Sensors & Actuators," *IEEE Journal of Microelectromechanical Systems*, Vol. 5, No. 3, pp. 166-179, September 1996
9. B. Ziaie, M.D. Nardin, A.R. Coghlan, and K. Najafi, "A Single-Channel Implantable Microstimulator for Functional Neuromuscular Stimulation," *IEEE Trans. on Biomedical Engineering*, Vol. BME-44, No. 10, October 1997
10. J.S. Walter, L. Riedy, W. King, J.S. Wheeler, K. Najafi, C.L. Anderson, T.M. Gudausky, and M. Dokmeci, "Short-Term Bladder-Wall Response to Implantation of Microstimulators," *J. of Spinal Cord Medicine*, Vol. 20, No. 3, pp. 319-323, 1997
11. K. Najafi, "Silicon Micromachining Technologies: Future Needs and Challenges," Invited Speaker *SPIE, Micromachining & Microfabrication Process Technology II Conference*, October 1996
12. B. Ziaie, J. Von Arx, K. Najafi, "A Micro-Fabricated Planar High-Current IrOx Stimulating Microelectrode," *IEEE Eng. in Medicine and Biology (EMBS) Conf.*, Amsterdam, October 1996
13. J. Von Arx, and K. Najafi, "On-Chip Coils with Integrated Cores for Remote Inductive Powering of Integrated Microsystems," *Ninth IEEE Int. Conference on Solid-State Sensors and Actuators, Transducers '97*, Chicago, June 1997

14. M. Dokmeci, J. Von Arx, and K. Najafi, "Accelerated Testing of Anodically Bonded Glass-Silicon Packages in Salt Water," *Ninth IEEE Int. Conference on Solid-State Sensors and Actuators, Transducers '97*, Chicago, June 1997

Doctoral Theses:

1. Dr. Mark Nardin; Thesis title: "A Programmable Multichannel Microstimulator with Bi-Directional Telemetry." Graduation: March 1996
2. Dr. Jeffrey A. Von Arx; Thesis Title: "A Single Chip, Fully Integrated, Telemetry Powered System For Peripheral Nerve Stimulation." Graduation: March 1998

References

- [1] J. K. Niparko, R. A. Altschuler, X. Xue, J. A. Wiler, and D. J. Anderson, "Surgical Implantation and Biocompatibility of CNS Auditory Prostheses," *Ann. Otol. Rhinol. Laryngol.*, vol. 98, pp. 965-970, 1989
- [2] J. K. Niparko, R. A. Altschuler, D. A. Evans, X. Xue, J. Farraye, and D. J. Anderson, "Auditory Brainstem Prosthesis: Biocompatibility of Stimulation," *Otolaryngol. Head Neck Surg.*, vol. 101, pp. 344-352, 1989